Photoluminescence from Defects in Two-Dimensional Transition Metal Dichalcogenides

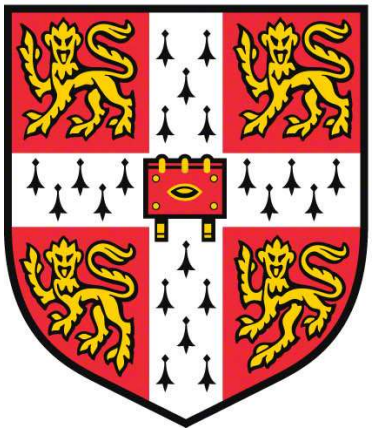

Yiru Zhu

Department of Materials Science & Metallurgy

Magdalene College

This thesis is submitted for the degree of

Doctor of Philosophy

March 2024

Declaration

This thesis is the result of my own work and includes nothing which is the outcome of work done in collaboration except as declared in the preface and specified in the text. It is not substantially the same as any work that has already been submitted, or, is being concurrently submitted, for any degree, diploma or other qualification at the University of Cambridge or any other University or similar institution except as declared in the preface and specified in the text. It does not exceed the prescribed word limit for the relevant Degree Committee.

Yiru Zhu

March 2024

Abstract

Atomic defects in monolayer transition metal dichalcogenides (TMDs) such as chalcogen vacancies significantly affect their properties. In this thesis, I provide a reproducible and facile strategy to rationally induce chalcogen vacancies in monolayer MoS_2 by annealing at 600 °C in an argon/hydrogen (95 *vol.*%/5 *vol.*%) atmosphere. At sulfur vacancy densities of ~1.8×10^{14} cm^{-2}, I observe defect-mediated photoluminescence (PL) at ~1.72 eV (referred to as LX_D) at room temperature. The LX_D emission is attributed to excitons trapped at defect-induced in-gap states and is typically observed only at low temperatures (≤77 K). Time-resolved PL measurements reveal that the lifetime of defect-mediated LX_D emission is longer than band edge excitons, both at room and low temperatures (~2.44 ns at 8 K). My results provide insight into how excitonic and defect-mediated PL emission in MoS_2 are influenced by sulfur vacancies at room and low temperatures.

I also show that the LX_D peak can be suppressed by annealing the defective MoS_2 in sulfur or selenium vapor, which indicates that it is possible to passivate the vacancies. At annealing temperatures ≥600 °C in selenium vapor, I observed the filling of sulfur vacancies by selenium.

I extended the defect generation strategy to monolayer MoS_2 on various dielectric substrates to investigate the influence of dielectric substrates on defect-mediated emission. The LX_D emission after annealing was observed on SiO_2 and hBN, but not on HfO_2. When the MoS_2 is first annealed on SiO_2 and then transferred onto HfO_2, the LX_D emission is present on untreated HfO_2, but not on annealed HfO_2. These results suggest that surface states in dielectric substrates can influence the defect-mediated emission.

I dedicate this thesis to my beloved mother Jing Xu and father Shiguo Zhu, for their infinite love, care, and support.

“After all, tomorrow is another day!”

— Margaret Mitchell, Gone with the Wind.

Acknowledgments

As I bring my Ph.D. journey to a close, I would like to express my deepest gratitude to the people who supported me throughout this journey, without whom, the completion of this journey would not be possible.

First and foremost, I would like to thank my supervisor Prof. Manish Chhowalla and advisor Prof. Robert L. Z. Hoye for their invaluable supervision and guidance during my PhD study. I want to thank Prof. Manish Chhowalla for taking great care of me during my academic research and daily life. His remarkable visions and knowledge have influenced me greatly and I learned a lot from him about how to become a good researcher. I would like to thank Jackie and Emile for hosting the wonderful barbecue parties. I will never forget the wonderful time I had with his cats Kitty and Oscar that helped me forget my stress and relax my mind. I would also like to thank Prof. Robert L. Z. Hoye who always set a good example to me even before I started my PhD study.

Very special thanks to Dr. Yan Wang and Dr. Soumya Sarkar, for their mentorship. When I first joined the 2DMD group, Yan guided me from the initial step in research to progressively develop an understanding of the subject. Her level of critical thinking has inspired me to assess my work as a whole. I would also like to thank Soumya for being consistently willing to listen to me when I talked about something that I was unsure of, even after a long day at work. His very positive response helped me build up my confidence.

Furthermore, I would like to thank all the members of the 2DMD group, past and present, for creating such a comfortable environment for research. It is my great fortune to be a part of this group, along with so many supportive people. I would like to begin by thanking Dr. Peter Knight, our group technician, for his endless and prompt help with all the lab issues that makes the 2DMD lab such an ideal place to conduct experiments. I would like to thank Ms. Ana Talaban-Bailey for arranging all the meetings and supporting the administrative work. I would like to thank Dr. Hugh Ramsden for never getting annoyed whenever I suddenly came up with an idea and caught him for discussions. He always took my ideas seriously and our scientific discussions encouraged me to interpret my results in the right way. I would like to thank Dr. Yang Li and Mr. Han Yan for device fabrication, whom I could always count on when I needed

to prepare a lot of samples in a very limited time for conducting Synchrotron XPS. I would like to thank Dr. Ye Wang for her support with full encouragement and enthusiasm. I am very impressed by how much effort she devotes to her work and her determination has inspired me to keep pursuing my PhD when I am held back by difficulties. I would also like to thank Dr. Zhuangnan Li and Mr. Jeffery Yang for their help with XPS and XRD measurements. I would also like to extend my thanks to Prof. Jieun Yang, Dr. Moon Hyo Kang, Dr. Javier Rubio Garcia, Dr. Jincheng Tong, Dr. Wenshuo Xu, Dr. Jung-In Lee, Dr. Jung-ho Kim, Dr. Ismail Sami, Dr. Benxuan Li, Mr. James Moloney, Ms. Jiahang Li, Ms. Han Zang, Ms. Maheera Abdul Ghani.

Dr. Juhwan Lim and Dr. Nicolas Gauriot are thanked for their expertise in various optical characterization techniques and all the helpful discussions. I would like to thank Dr. Zhepeng Zhang for his valuable help with low-temperature optical measurements under the supervision of Prof. Goki Eda. I would also like to thank Dr. Dibya Phuyal for his assistance with Synchrotron XPS measurements.

Finally, I would like to thank my parents and my sister Ms. Ning Sun for always being there for me. They always have faith in every decision I make, even when I am not very confident about it. Their forever love keeps me motivated all the time.

Table of Contents

Chapter 1 Introduction

Three-dimensional (3D) semiconductors (*e.g.*, silicon, GaN, GaAs) are staples of the electronics industry, with applications that include transistors[1,2], optoelectronic devices (*e.g.*, photodiodes[3], solar cells[4], light-emitting diodes[5]), and electro-/photo-catalysts[6]. For these applications, an important consideration is the role of defects. Under equilibrium conditions at room temperature, defects are unavoidable in crystalline semiconductors. These include line defects (such as dislocations), planar grain boundaries, macroscopic structural defects (such as voids), and atomic-level point defects such as vacancies and interstitials. Significant efforts have been made in mitigating the role of defects in materials to achieve optimal performance.[7–9] For example, record-efficiency in silicon solar cells requires fine control of growth parameters to remove grain boundaries, reducing impurities and point defects to the parts per billion level, and passivating defects at interfaces to minimize surface recombination.[10,11] However, although defects are conventionally viewed as detrimental, they can improve performance of materials in some cases. For example, sulfur vacancies in two-dimensional (2D) molybdenum disulfide have been extensively studied as active sites to improve catalytic activity by simultaneously adsorbing reactants and transferring charge carriers to active sites.[12] Another example is the long coherence time at room temperature of nitrogen-vacancy defect centers in diamond for quantum information processing and quantum sensing as well as room-temperature solid-state masers.[13,14] Understanding the role of defects on functionality of materials is therefore essential for optimizing device performance.

This thesis aims to develop an understanding of how atomic defects influence the photoluminescence in semiconducting 2D transition metal dichalcogenides (TMDs), primarily MoS_2.

The remaining **Chapter 1** reviews the fundamentals of 2D TMDs, including atomic and electronic structures that give rise to their interesting optical properties. Since sample quality significantly affects the properties of 2D TMDs, various synthesis methods used in literature are also discussed.

Chapter 2 reviews the fundamentals of defects in 2D TMDs. A comparison is made with traditional 3D semiconductors, with particular emphasis on point defects that are the most

relevant for 2D TMDs. The role of defects on electronic and optoelectronic properties is also discussed, including detrimental effects and opportunities that defects offer, and how they can be engineered to optimize performance of devices.

Chapter 3 describes synthesis methods used in this thesis. The principles of various characterization methods and relevant cases from literature are discussed. In particular, X-ray photoelectron spectroscopy (XPS), absorption spectroscopy, photoluminescence (PL) spectroscopy, Raman spectroscopy, atomic force microscopy (AFM), and X-ray diffraction (XRD) are described.

Chapter 4 describes my original work on generation of defects by annealing monolayer TMDs in Ar/H_2 (95 *vol.*%/5 *vol.*%) atmosphere. By controlling the temperature, duration, and environment of thermal annealing, it is shown that sulfur vacancies can be reproducibly generated in 2D MoS_2. The sulfur vacancies introduce in-gap electronic states that lead to defect-mediated PL observed at room temperature (~300 K). The nature of in-gap states is explored by temperature-dependent, time-resolved, and power-dependent PL spectroscopy. In this chapter, I also show that defect-mediated PL can be suppressed by passivating the sulfur vacancies via annealing in sulfur or selenium vapor.

Chapter 5 investigates the influence of different dielectric substrates on defect-mediated PL and builds on the work in Chapters 4. It shows that strong doping from the surface states on substrates leads to passivation of defect states of sulfur vacancies that leads to suppression of defect-mediated emission PL peak.

Chapter 6 concludes the main findings of my research and presents how the findings could be of broader interest for future investigations. A few projects for future research are suggested.

1.1 Transition Metal Dichalcogenides (TMDs)

2D materials have received interest since the discovery of graphene. 2D TMDs, such as MoS_2 and WSe_2, have attracted attention because they can be direct bandgap semiconductors at monolayer thickness with interesting optical and electronic properties.

1.1.1 Atomic Structure

TMDs have a layered structure, in which each unit layer MX_2 consists of transition metal cations sandwiched between two chalcogen anions through polar covalent bonds. M represents a transition metal cation from group IV – X, such as Ti, V, Nb, Mo, Hf, Ta, and W; X represents a chalcogen anion, such as S, Se, and Te. Adjacent unit layers of MX_2 are held together by weak van der Waals (vdW) interactions. Owing to the vdW interactions, bulk TMDs can be mechanically or chemically exfoliated to atomically thin single layers.[15] Depending on the different coordination of atoms, single-layer TMDs can be categorized into two polymorphs, trigonal prismatic phase (1H) or octahedral phase (1T). In 1H phase, each metal atom is covalently bonded to six chalcogen atoms (**Figure 1.1**).[16] The chalcogen atoms in different atomic planes are aligned along the z-axis with the chalcogen–metal–chalcogen stacking order of AbA and the hexagonal symmetry (D_{3h} = E, C_3, $2C_2$, σ_h, S_3, $3\sigma_v$) can be seen in the top view. E is the identity element, taking the molecule back into the same position it started. C_3/C_2 is a 3-fold/2-fold axis of rotation symmetry. σ_h/σ_v is a plane of reflection symmetry in which the mirror plane is perpendicular/parallel to the principal axis of the molecule. S_3 is a 3-fold axis of improper rotation symmetry (rotation-reflection symmetry). Compared to 1H phase, 1T phase has the same trigonal chalcogen layer on the top but a 180° rotated layer at the bottom. The stacking order of AbC corresponds to tetragonal symmetry (D_{3d} = E, $2C_3$, $3C_2$, *i*, $2S_6$, $3\sigma_d$). Here *i* is a center of inversion symmetry. σ_d is a plane of reflection symmetry in which the mirror plane is diagonal to the principal axis of the molecule. 1T phase also has a lower-symmetry version phase called distorted octahedral structure (1T′).

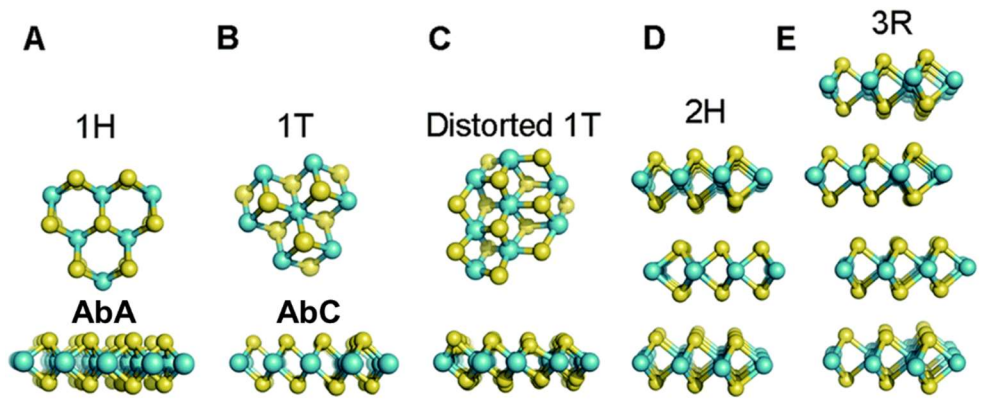

Figure 1.1. Typical structures of layered transition metal dichalcogenides with 1H, 1T, distorted 1T (referred to as 1T'), 2H, and 3R phases, where the green atoms denote transition metal atoms and the yellow atoms denote chalcogen atoms. Reproduced from Ref. [16].

Extending to multilayers, different stacking orders of 1H layers give rise to either 2H phase with hexagonal symmetry or 3R phase with rhombohedral symmetry. Most TMD materials have more than one phase and the thermodynamically stable phase strongly depends on the *d*-electron count.

1.1.2 Electronic Structure

Most TMD materials have more than one phase with different electronic properties, for example in MoS_2, 1H-MoS_2 is semiconducting phase while 1T-MoS_2 is metallic, with the corresponding electronic structure shown in **Figure 1.2**.[17] Since non-bonding transition metal *d* orbitals are located close to the Fermi level whereas chalcogen *p* orbitals are located at much lower energies, the electronic properties of TMDs are determined by the filling level of transition metal *d* orbitals. For 1H MoS_2, the orbitals split into three degenerate states: d_{z^2}, $d_{x^2-y^2,xy}$, and $d_{xy,yz}$. For 1T MoS_2, the orbitals split into two degenerate states: $d_{xy,yz,zx}$ (t_{2g}) and $d_{x^2-y^2,z^2}$ (e_g).

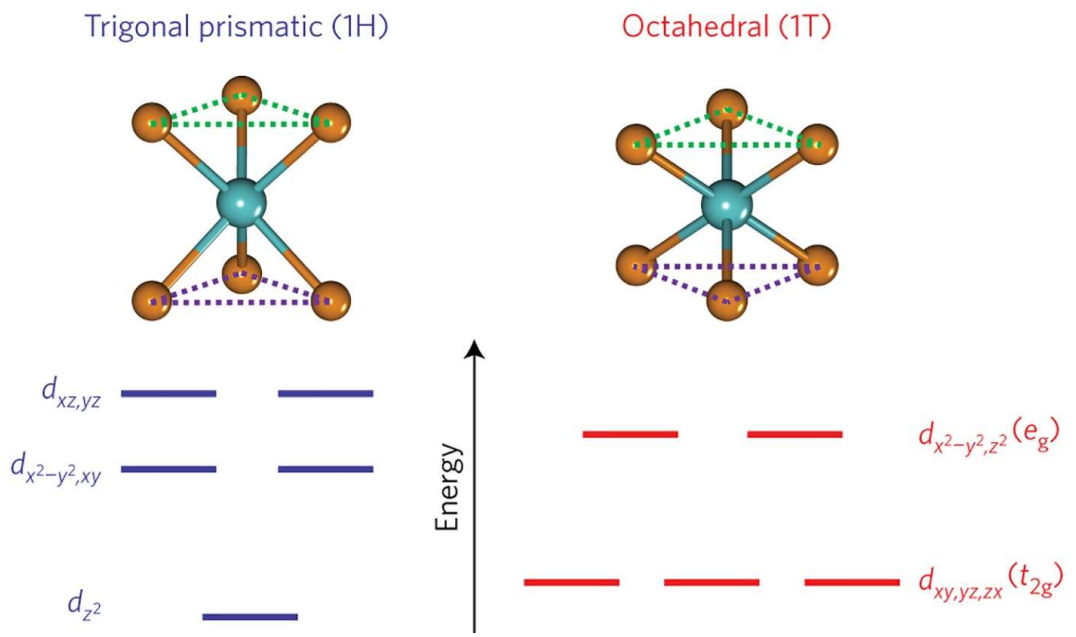

Figure 1.2. Schematic of energy levels of transition metal d orbitals in 1H and 1T phase TMDs. In 1H TMDs, transition metal d orbitals degenerate into three states of d_{z^2}, $d_{x^2-y^2,xy}$, and $d_{xy,yz}$; In 1T TMDs, transition metal d orbitals degenerate into two states of $d_{xy,yz,zx}$ (t_{2g}) and $d_{x^2-y^2,z^2}$ (e_g). Reproduced from Ref. [17].

The filling level of transition metal *d* orbitals determines the thermodynamically favorable phase of TMDs (**Figure 1.3**).[18] Group-4 TMDs have no *d*-electron (d^0) and show 1T configuration. For group-5 TMDs, electrons fill d_{z^2} orbital of 1H phase and generate both 1H and 1T phase. Group-6 TMDs (d^2) mostly show 1H phase with a bandgap formed between $d_{x^2-y^2,xy}$ and d_{z^2} orbitals. Filling above d_{z^2} orbital to $d_{x^2-y^2,xy}$ orbital promotes the transformation of 1H structure into 1T. Therefore, group-7 TMDs (d^3) show 1T′ phase while group-9 (d^5) and group-10 (d^6) TMDs show 1T phase. The energy difference between 1H and 1T phases is ~1 eV.[16] This allows semiconducting 2H MoS_2 to phase transform into metallic 1T phase by Li-intercalation through electron transfer from n-butyllithium to MoS_2, so that total electron count in *d* orbital of Mo increases from 2 to 3.[19]

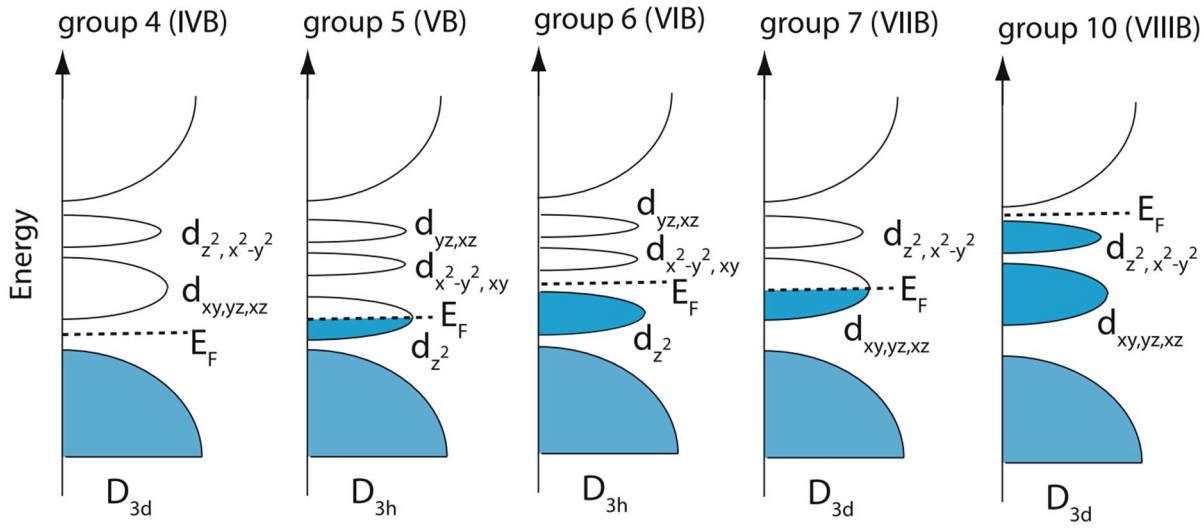

Figure 1.3. Schematic of the filling level of transition metal d orbitals in group 4 – 10 TMDs. D_{3h} represents the hexagonal symmetry for 1H phase and D_{3d} represents the tetragonal symmetry for 1T phase, respectively. Reproduced from Ref. [18].

1.2 Semiconducting TMDs – From Bulk to Monolayer

The semiconducting behavior of 2D TMDs is determined by their thickness. Taking MoS_2 as an example, with decreasing layer numbers, the lowest energy transition (between conduction band minimum [CBM] and valence band maximum [VBM]) evolves from indirect (CBM and VBM have different momentum values) to direct (CBM and VBM have the same momentum value), as shown in **Figure 1.4**.[20] This is due to the lack of sulfur-sulfur interlayer interactions. Typically, most 2H semiconducting 2D TMDs show direct bandgap in monolayers (1H) and indirect bandgap in bulk form (2H). This applies to MoS_2, $MoSe_2$, WS_2, WSe_2, and $MoTe_2$. Owing to the quantum confinement effect, discrete electronic states exist in 2D TMDs and provide the basis for controllable electronic spins and valleys of individual carriers. This makes TMDs promising candidates for spintronic and valleytronic applications, offering the potential of energy-efficient data storage and logic applications.[21–23] The bandgap of TMD monolayers ranges from near-infrared to visible spectral region, which ensures large optical absorption coefficient and remarkable quantum efficiency at nanometer thickness.[24] These properties enable TMDs to achieve high solar energy conversion efficiency across the entire visible spectrum when normalized to their mass or thickness.[25] This is critical for applications, including photovoltaics, electronics, sensors, and light sources for long-distance quantum

communication.[26] Further, vdW interlayer interactions allow the creation of vertical heterostructures with tunable optoelectronic phenomena.[27]

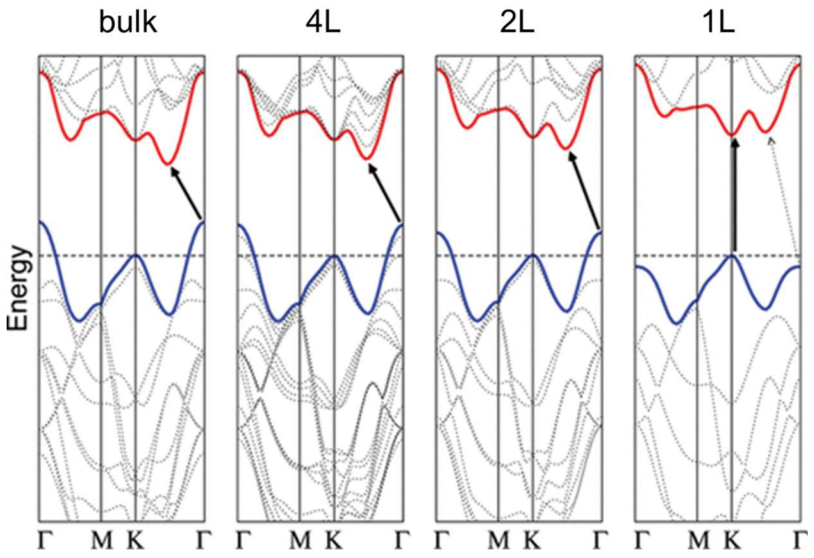

Figure 1.4. Energy dispersion in bulk, quadrilayer (4L), bilayer (2L), and monolayer (1L) MoS_2. The red and blue lines denote the conduction and valence band edges, respectively. The black arrows represent the lowest energy transitions from the valence band maximum to the conduction band minimum, evolving from indirect to direct (vertical) transitions with decreasing layer numbers. Reproduced from Ref. [20].

1.3 Photoluminescence (PL) from Semiconducting TMDs

Photoluminescence (PL) is spontaneous light emission from a semiconductor following photo-excitation. When the photon energy of the light source is larger than the bandgap of the semiconductor (**Figure 1.5a**, blue arrow), electrons in the valence band are excited to the conduction band, leaving holes in the valence band.[28] The excited electron relaxes to the CBM and the energy difference is released as phonons (represented by small grey arrow in (**Figure 1.5a**). For a direct-bandgap semiconductor, PL occurs when electrons at the CBM radiatively recombine with holes in the VBM to release photons (represented as red arrow in **Figure 1.5a**). In contrast, PL from indirect bandgap semiconductors undergoes a more complicated process. Due to the momentum mismatch between CBM and VBM in indirect bandgap semiconductors, indirect CBM-to-VBM transitions can only occur when momentum is supplied by phonons (represented as dashed red arrow in **Figure 1.5b**).[29] This principle

applies to both photoexcitation and PL emission. For photoexcitation, the direct transitions from valence band to conduction band (the valley shown in yellow) are also possible but this requires an excitation photon energy a lot higher than the bandgap energy. However, the hot carrier would then thermalize to the lowest energy state, and this energy funneling would then typically still result in electrons and holes at the band-extrema at different points in *k*-space. PL emission from these cold carriers would then still have to satisfy the condition of momentum conservation. PL emission involves multiple processes, the probability of radiative recombination for achieving PL is very low in indirect bandgap semiconductors. This leads to low photoluminescence quantum yield (PLQY). That is, the ratio of the number of emitted photons to the number of absorbed photons is low. As a result, indirect bandgap semiconductors are not as efficient as direct bandgap semiconductors for light-emitting devices.

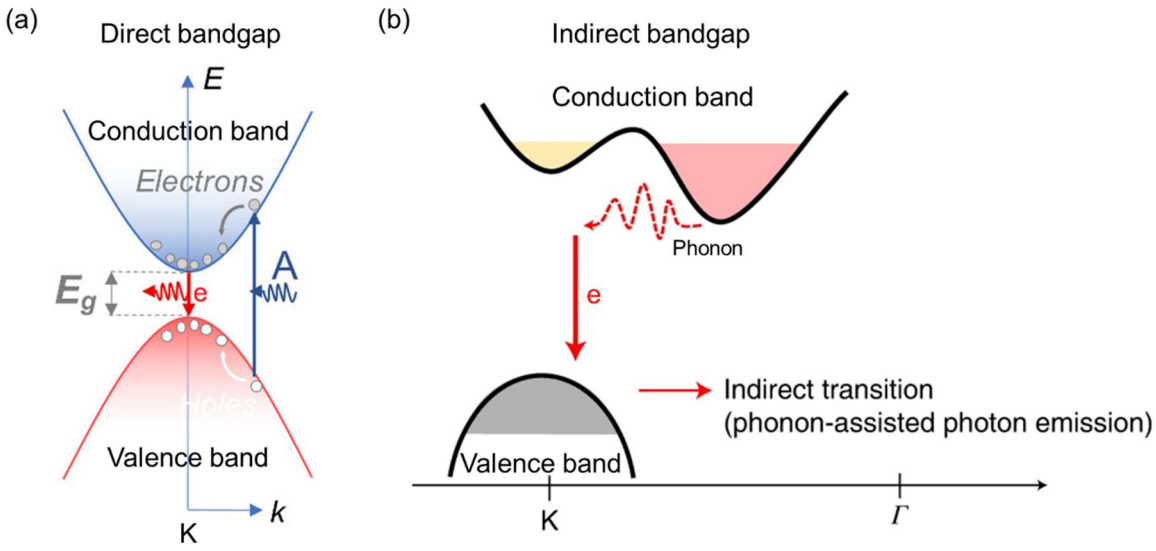

Figure 1.5. Schematic of PL process in (a) a direct bandgap semiconductor and (b) an indirect bandgap semiconductor. In (a), the blue arrow (A) represents photon absorption, red arrow (e) represents photon emission (PL), grey arrow represents phonon emission, E_g represents the bandgap of the semiconductor, and k represents the wavevector of electrons and holes.[28] The diagram shows the band structure at K point of 2D MoS_2 Brillouin zone. In (b), the dashed red arrow represents phonon that assists an electron to relax from CBM to VBM. Γ represents the center of Brillouin zone.[29] Reproduced from Refs. [28,29].

Bulk TMDs are indirect bandgap semiconductors and therefore are dominated by phonon-assisted transitions. PLQY for bulk TMDs such as MoS_2 is low (**Figure 1.6a**, inset).[30] The PLQY increases steadily with decreasing thickness and reaches the highest value (~4×10^{-3}) in monolayers (**Figure 1.6a**). However, the PLQY in monolayers is still low due to non-radiative recombination related to impurities, adsorbed layers, vacancies and other defects. 2D semiconducting TMDs exhibit reduced dielectric screening and enhanced Coulomb interactions. Hence the photoexcited free electron-hole pairs are Coulombically attracted to form tightly bound quasi-particles called excitons near the band edge and have lower energy

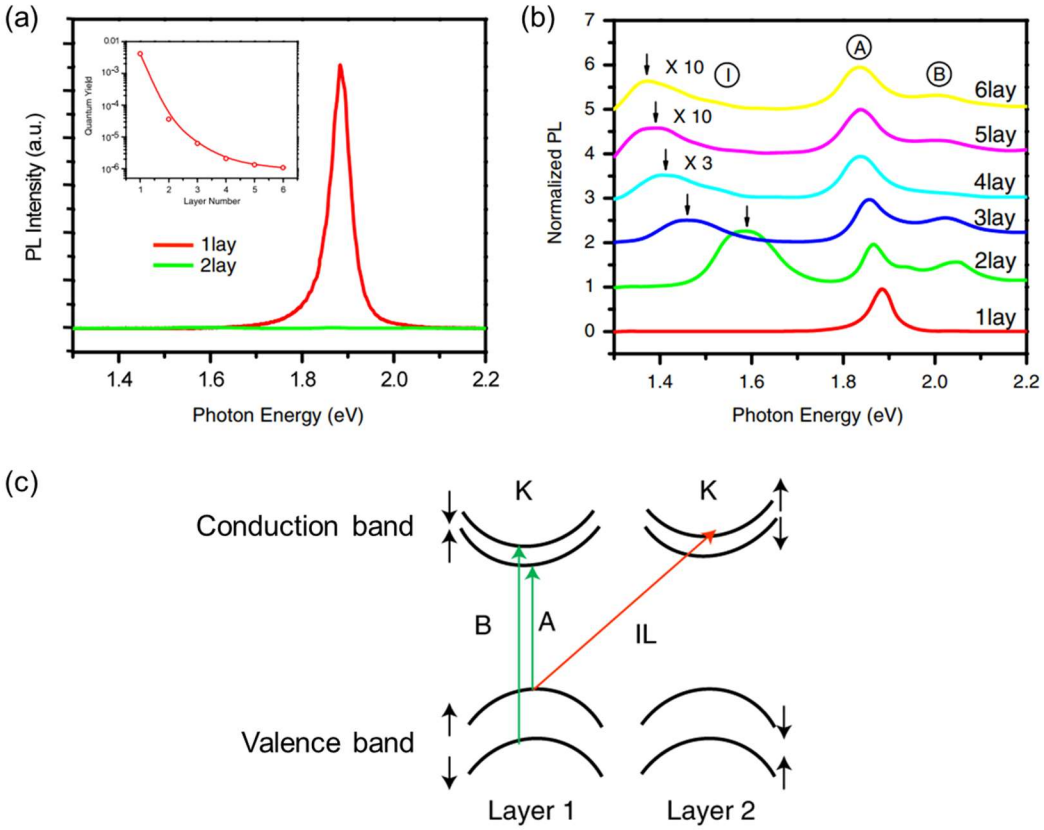

Figure 1.6. Room-temperature (RT) PL spectra of MoS_2 samples with layer numbers ranging from 1 to 6. (a) RT PL spectra of monolayer and bilayer MoS_2.[30] Inset: PLQY of thin layers of MoS_2, decreasing with increasing layer numbers. (b) RT PL spectra of thin layers of MoS_2, showing A, B, and I peaks.[30] The spectra are normalized to the intensity of A peak. (c) Schematic energy band diagram of bilayer MoS_2 with spin states denoted by black arrows.[31] The intralayer optical transitions of A and B excitons are denoted by green arrows, and the interlayer optical transition of IL exciton is denoted by red arrow. Reproduced from Refs. [30,31].

and ~0.4 eV for W-based TMDs, while the splitting for the conduction band is <0.1 eV.[27] Both A and B excitons are optically bright excitons with the electron and hole having the same spin states. In contrast, dark excitons with the electron and hole having the opposite spin states are spin-forbidden.

The A exciton emission peak in monolayer MoS_2 shown in **Figure 1.6a** is typically asymmetric due to the presence of trions (charged excitons composed of a neutral exciton bound with an extra electron/hole) at lower photon energies. This is due to doping of semiconductors. If the majority charge carriers are holes, the trions will be positive; if the majority charge carriers are electrons, the trions will be negative. In 3D semiconductors, the binding energy of trions (that is, the energy required to separate a trion into a neutral exciton and an unbound electron/hole) is small (several meV). Therefore, radiative recombination of free trions and neutral excitons appears as a single near-band-edge emission peak.[35] In contrast, excitonic recombination of trions and neutral excitons in 2D TMDs are significantly split due to reduced dielectric screening and enhanced Coulomb interactions, even at room temperature. The binding energy of trions in 2D TMD semiconductors is found to be tens of meV.[36,37] Javey's group has shown that PL emission of neutral A excitons and A^- trions in monolayer MoS_2 can be tuned by the application of a gate voltage, as shown in **Figure 1.8a**.[38] When more electrons are added into MoS_2 at gate voltage of 80 V, the exciton spectral weight is transferred to trions, suggesting that trions in MoS_2 are in the negative charge state. As a result, the ratio of the integrated intensity of A^- trion to A exciton, $I(A^-)/I(A)$, can be used to illustrate the density of excess free carriers in MoS_2. Suppressing the formation of trions while boosting the formation of neutral excitons at −70 V in the low exciton density regime, the PLQY reaches the highest (75% ± 10%), as shown in **Figure 1.8b**.[39] This indicates that recombination of neutral excitons is dominated by radiative recombination, whereas the recombination of trions is dominated by non-radiative recombination. A similar effect can be achieved in monolayer MoS_2 chemically treated with a strong protonating superacid bis(trifluoromethane) sulfonimide (TFSI).[40] The electron counter doping effect of TFSI enhances the PLQY to >95%.

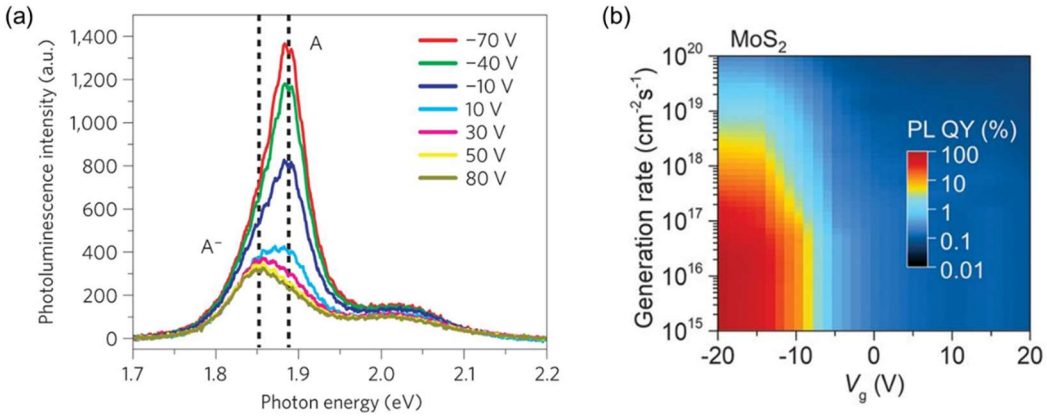

Figure 1.8. PL features of monolayer MoS_2 at different gate voltages. (a) PL spectra measured at gate voltages ranging from −70 V to 80 V.[38] Both neutral exciton (A) and trion (A^-) features can be identified, as indicated by the dashed lines. With gate voltage tuned from −70 V to 80 V, the dominant emission peak is changed from A exciton peak to A^- trion peak. (b) Color plot of PLQY as a function of photocarrier generation rates and gate voltage (V_g) for monolayer MoS_2.[39] The photocarrier generation rates are varied by the incident pump power. Reproduced from Ref. [38,39].

1.4 Synthesis Methods of TMDs

1.4.1 Bulk

Chemical vapor transport (CVT) is a well-developed technique for growing crystals. The growth is based on the use of vapor transport agent, usually a volatile halogen substance. The elemental precursors and transport agent are sealed in a quartz ampoule under vacuum ($<10^{-3}$ Torr). At the hot source end of a sealed transport ampoule, the vapor transport agent reacts with nonvolatile metal and forms intermediate gaseous substances that can diffuse to the cold growth end (see schematic in **Figure 1.9a,b**).[41] Under high pressure, the intermediate substance is dissociated, forming target crystals while releasing the transport agent. CVT can grow large crystals at high temperatures (>1000 °C) and has become the prevalent technique for producing bulk crystals of various TMDs. One critical parameter of this method is selecting a suitable transport agent. For most TMDs, the most common transport agent is iodine, while bromine has also been successfully used to grow MoS_2 and $MoSe_2$ crystals.[42,43] Bougouma *et al.* also reported using $TeCl_4$ as transport agent to grow $MoSe_2$ crystals.[44] The other key factors include growth temperatures and the ratio of reactants. Hu *et al.* reported the growth of high-quality MoS_2 monolayers at low temperatures (300 – 600 °C) with a low defect density.[45] However, it

is difficult to completely remove the transport agent residues even by rinsing with proper solvents. Another challenge in CVT growth is condensed nucleation that leads to aggregation of crystals with restricted sizes. To achieve larger crystals, seeded CVT growth has been developed by adding a seed crystal at the growth end to suppress excess nucleation and promote lateral growth. Li *et al.* reported seeded growth of large-sized $MoSe_2$ and $MoTe_2$ crystals up to 3 mm, and $PtSe_2$ crystals with a shortened growth period.[46]

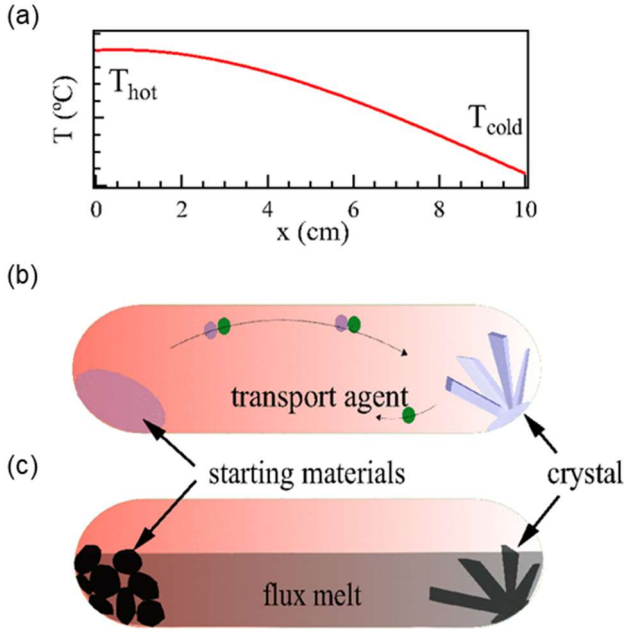

Figure 1.9. Schematic of CVT and flux growths. (a) Temperature profile along a horizontal sealed ampoule. (b) Schematic of CVT in which volatile transport agent chemically reacts and transports non-volatile starting materials from the hot source end of the sealed ampoule to the cold growth end. (c) Schematic of flux growth in which flux dissolves and transports starting materials from the hot end to the cold end. Reproduced from Ref. [41].

Flux growth method is an alternative liquid transport growth method without chemical reactions. The flux dissolves starting precursors at high temperatures and diffuses to the cold end, followed by supersaturation, precipitation, and crystallization (see schematic in **Figure 1.9a,c**).[41] Depending on the choice of flux, this method can be categorized into two types: exotic-flux method and self-flux method. There are two essential requirements for exotic flux, low melting point and high boiling point. Zhang *et al.* reported the growth of MoS_2 using Sn flux, obtaining large-sized (3 mm × 5 mm) MoS_2 single crystals.[47] However, the exotic-flux

method commonly has the same residue removal problem as CVT, making the self-flux method a better choice. The growth of $MoSe_2$ and WSe_2 assisted by self-flux Se has achieved a defect density of ~10^{11} cm^{-2} compared to CVT (>10^{12} cm^{-2}), quantified by scanning transmission electron microscopy (STEM) and scanning tunneling microscopy (STM) topographic images.[48–50]

1.4.2 Thin Film/Monolayer

1.4.2.1 Mechanical/Liquid Exfoliation

The vdW interactions in bulk TMDs can be overcome by applying external mechanical or chemical force, thereby breaking the vdW bonding and isolating single layers.

Tape mechanical exfoliation of 2D TMD crystals refers to peeling off TMD flakes layer by layer using adhesive Scotch tape. The adhesive force can break vdW bonds between adjacent layers of TMD crystals, thereby allowing repeated exfoliation of bulk crystals into few layers and even monolayers (**Figure 1.10**).[51] Pressing the Scotch tape on a substrate (*e.g.*, SiO_2/Si wafer) with suitable mechanical force allows exfoliated flakes to adhere on the substrate. However, under the applied mechanical force, the fragile thin exfoliated flakes (few layers and monolayers) can fragment into smaller pieces, often restricting the lateral sizes to <10 μm.

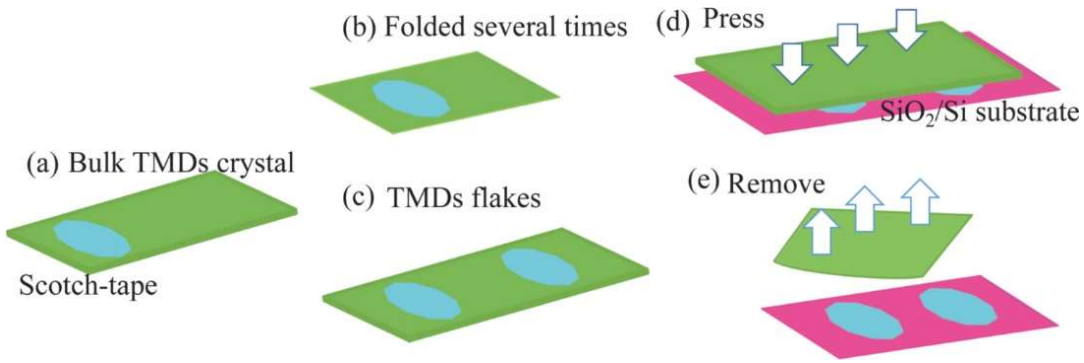

Figure 1.10. Schematic of conventional tape mechanical exfoliation process. Reproduced from Ref. [51].

Polydimethylsiloxane (PDMS)-assisted mechanical exfoliation uses less-adhesive PDMS gel film to transfer exfoliated flakes from the Scotch tape to PDMS stamp and then to substrate (**Figure 1.11**). The lower adhesive strength of PDMS allows it to be easily separated from both Scotch tape and substrate, thus minimizing the fragmentation of thin flakes to reach large lateral sizes (>20 μm). However, both tape mechanical exfoliation and PDMS-assisted mechanical exfoliation are hindered in application by the low exfoliation yield of thin flakes due to weak vdW interaction between Scotch tape and TMD layers.

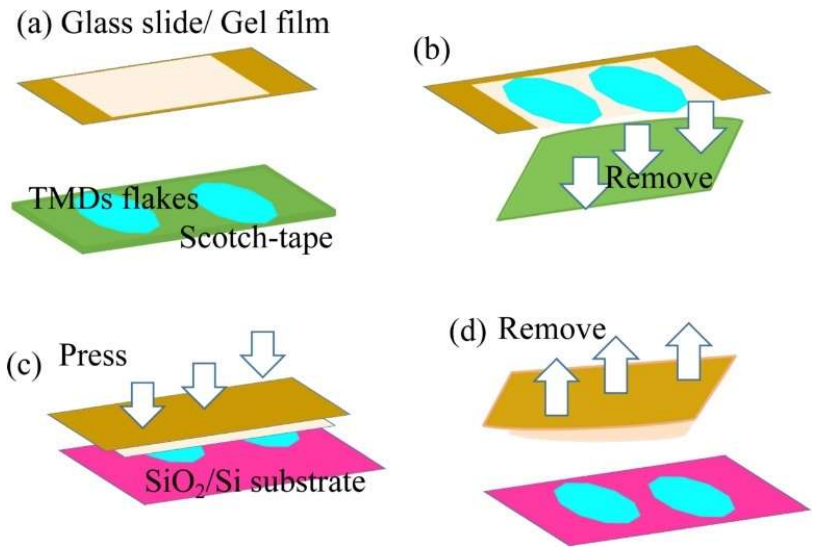

Figure 1.11. Schematic of PDMS-assisted mechanical exfoliation process. Reproduced from Ref. [51].

Gold-assisted exfoliation has been developed to increase the exfoliation yield of macroscopic (millimeter scale) monolayer TMDs by using Au as exfoliation substrate. Owing to highly polarizable electron densities, large dispersion attraction is introduced at the Au/TMD interface, forming covalent-like quasi-bonding (CLQB) that overcomes the interlayer interactions between the bottom most layer and its adjacent layer in TMD crystal (**Figure 1.12**).[52] This facilitates peeling of the bottom most monolayer when Au is removed from the crystal. Velický *et al.* reported that fresh Au substrate that is exposed to air for <6 min can yield 70 – 80 % monolayer MoS_2.[53] However, if exposed to air for >15 min then the fresh Au substrate gradually ages due to adsorption of organic airborne contaminants. This weakens MoS_2−Au adhesion and consequently results in negligible exfoliation yield. This method has

been applied to other TMDs to produce millimeter-sized monolayers, including $MoSe_2$, WS_2, WSe_2, $MoTe_2$, and WTe_2, as well as to other 2D materials, including GaSe, BP, FeSe, Fe_3GeTe_2, $RuCl_3$, $PtSe_2$, $PtTe_2$, $PdTe_2$, and CrSiTe. Yet, we need to note that although this exfoliation method itself is contamination-free, transferring the exfoliated flakes from Au to other substrates (*e.g.*, SiO_2/Si) requires KI/I_2 etchant to remove Au due to strong TMD−Au adhesion. This wet-transfer method is commonly assisted by PMMA support layer that unavoidably introduces polymer contamination.

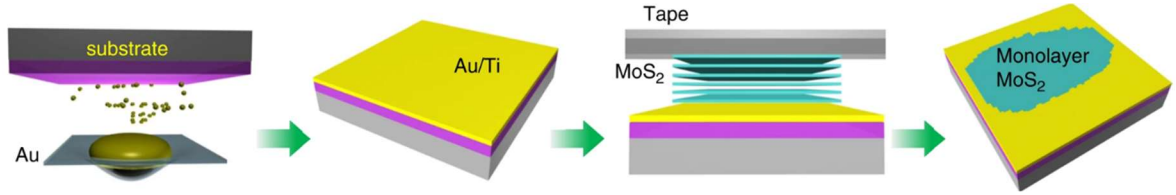

Figure 1.12. Schematic of gold-assisted exfoliation process. Reproduced from Ref. [52].

Liquid exfoliation provides a simpler and faster method of producing mass-scale 2D TMD materials. The bulk crystal is immersed into suitable solvents or surfactants to allow ions to intercalate between layers, weakening the interlayer interactions in TMD crystal. By applying external force, *e.g.*, ultra-sonication, the exfoliation process is initiated with adjacent layers detaching from each other (**Figure 1.13**).[54] Choosing proper solvents and surfactants with surface energy matching with TMDs, the exfoliated nanosheets form stable dispersion with limited reaggregation. Amine-based solvents, including N-methylpyrrolidone (NMP) and N,N-dimethylformamide (DMF), are the most effective for liquid exfoliation of TMDs, while ethanol and water have also been explored.[55] However, the quality of liquid-exfoliated flakes is significantly limited by defects, yield of monolayers, and doping introduced during the exfoliation process.

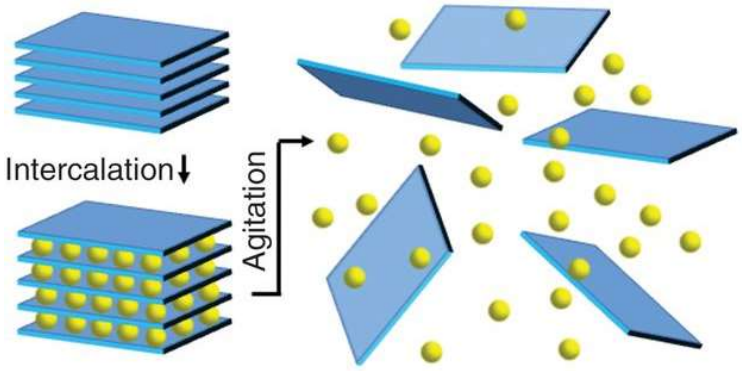

Figure 1.13. Schematic of the liquid exfoliation process. Reproduced from Ref. [54].

1.4.2.2 Bottom-Up Growth

To produce large-scale TMD monolayers, "bottom-up" growth methods have been developed, including chemical vapor deposition (CVD), atomic layer deposition (ALD), metal-organic CVD (MOCVD), and physical vapor deposition (PVD).

CVD is based on chemical reactions between transition metal and chalcogen precursors that grow thin films on suitable substrates. The growth rate depends on several key factors including growth temperature, gas flow, and type of substrate. There are two typical processes: (1) Direct chemical vapor phase reaction by co-evaporation of transition metal and chalcogen precursors under high temperature (see schematic in **Figure 1.14**).[56] Lee *et al.* synthesized large-scale MoS_2 layers at 650 °C using MoO_3 and sulfur powders with the reaction: $MoO_3(s)+S(g) \rightarrow MoO_{3-x}(s)+SO_x(g)$; $MoO_{3-x}(s)+S(g) \rightarrow MoS_2(s)$, but this recipe fails to achieve full coverage of the substrate.[57] Yu *et al.* reported growth of continuous MoS_2 films using $MoCl_5$ and sulfur precursors.[58] (2) Vapor phase chalcogenation of transition metal precursors that are pre-deposited on substrates. Zhan *et al.* reported MoS_2 film in which Mo film was pre-deposited on a SiO_2/Si wafer and annealed in sulfur vapor.[59] The lateral size and thickness of the resulting MoS_2 thin film can be controlled by the thickness of pre-deposited Mo film. However, CVD growth for atomically thin 2D TMDs is limited by the by-product of few-layer flakes, making it difficult to selectively produce monolayer TMDs.

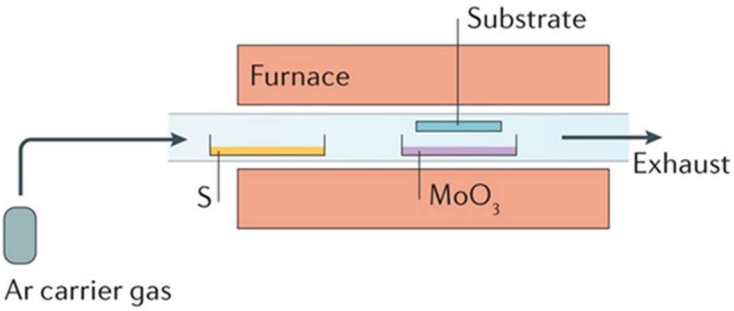

Figure 1.14. CVD growth of MoS_2 nanosheets based on the direct chemical reactions between different precursor materials. Reproduced from Ref. [56].

ALD in principle can achieve layer-by-layer growth of TMDs by alternately exposing transition metal precursor and chalcogen precursor to the substrate. The process consists of repeating cycles of two half-reactions. During each half-reaction, one precursor is pulsed to deposit one atomic layer. Every half-reaction is followed by subsequent purging with an inert carrier gas to eliminate unreacted precursors and reaction by-products. Thus, the number of TMD layers can be controlled by tuning the number of ALD cycles. Song *et al.* reported conformal ALD growth of WS_2 using WO_3 and H_2S, shown in **Figure 1.15**.[60] Their growth achieved 1-layer, 2-layer, and 4-layer over 20, 30, and 50 ALD cycles, respectively. However, due to the random adsorption of precursors in one cycle, random nucleation, and low diffusivity of precursor adsorbates, it is challenging to produce wafer-scale monolayers.[61]

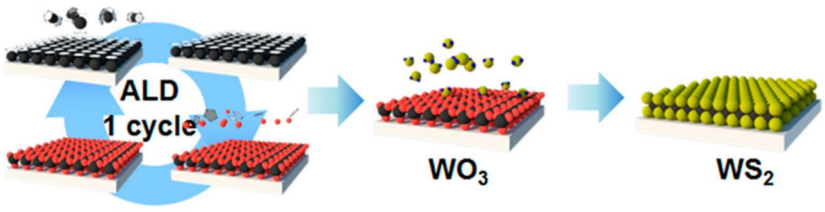

Figure 1.15. Schematic of ALD growth of WS_2 nanosheets. Reproduced from Ref. [60].

MOCVD has been reported for achieving wafer scale growth, using metal-organic precursors such as $Mo(CO)_6$, $W(CO)_6$, and chalcogen-organic precursors such as $(C_2H_5)_2S$ and $(CH_3)_2Se$. During the growth, organic precursors are thermally decomposed to deposit transition metal and chalcogen atoms on substrate. Similar to ALD, MOCVD can also achieve precise

stoichiometric control of precursors by regulating the partial pressure of each reactant. This offers an ideal environment to minimize the formation of nuclei and maximize the lateral growth of monolayers. However, the decomposition of carbon-based precursors can introduce carbon contamination to TMD products. Kang *et al.* reported the uniform growth of monolayer MoS_2 and WS_2 films on a 4-inch wafer by using $Mo(CO)_6$, $W(CO)_6$, and $(C_2H_5)_2S$ precursors, shown in **Figure 1.16**.[62] In this process, H_2 is used to remove impurities and by-product carbonaceous species, ensuring excellent structural and electrical uniformity over the entire films.

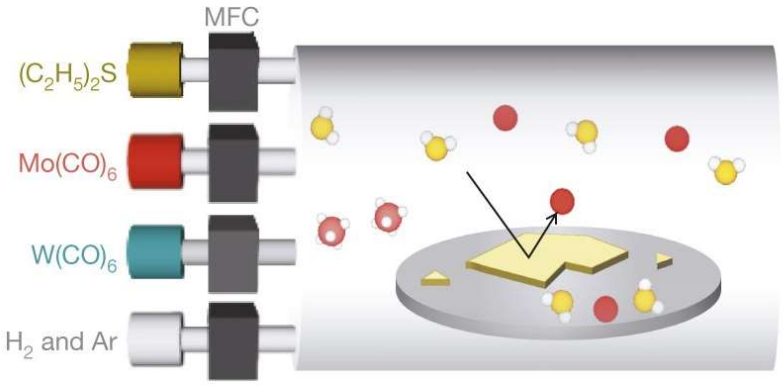

Figure 1.16. Schematic of MOCVD growth of continuous wafer-scale monolayer MoS_2 film. Reproduced from Ref. [62].

PVD, including sputtering, pulsed laser deposition (PLD) and molecular beam epitaxy, has been investigated to produce TMD thin films over large areas. Sputtering is usually performed by using energetic gaseous ions that can be accelerated from plasma to bombard the surface of the target material. With sufficient energy, the surface atoms are ejected out of the target material and then deposited on a substrate. Tao *et al.* reported one-step reactive sputtering deposition of MoS_2 by sputtering Mo on pre-heated c-plane sapphire (Al_2O_3) or SiO_2/Si, and sulfurizing Mo with gaseous sulfur atoms (**Figure 1.17a**).[63] The produced MoS_2 thin films were homogeneous across an area of centimeters. By adjusting key parameters including deposition time, substrate temperature, gas pressure, and sputtering power, the layer thickness of MoS_2 can be controlled. However, as sputtering and deposition are performed in the same chamber, re-sputtering of deposited material cannot be avoided. This has led to the development of two-step sputtering deposition that consists of non-reactive sputtering

deposition of target material in amorphous form and post-annealing to transform it into crystalline state. Krbal *et al.* reported deposition of amorphous MoS_2 film at room temperature, followed by post-annealing (**Figure 1.17b**).[64] This method produced single crystalline MoS_2 along the (002) plane. However, the high post-annealing temperature of 800 °C tends to cause sulfur deficiency in MoS_2. To compensate for the loss of chalcogen during high-temperature annealing, additional chalcogen source is required. Zeng *et al.* sputtered WS_2 precursor film onto a substrate and post-annealed the amorphous sample in sulfur vapor to crystalize WS_2 while maintaining its stoichiometry.[65]

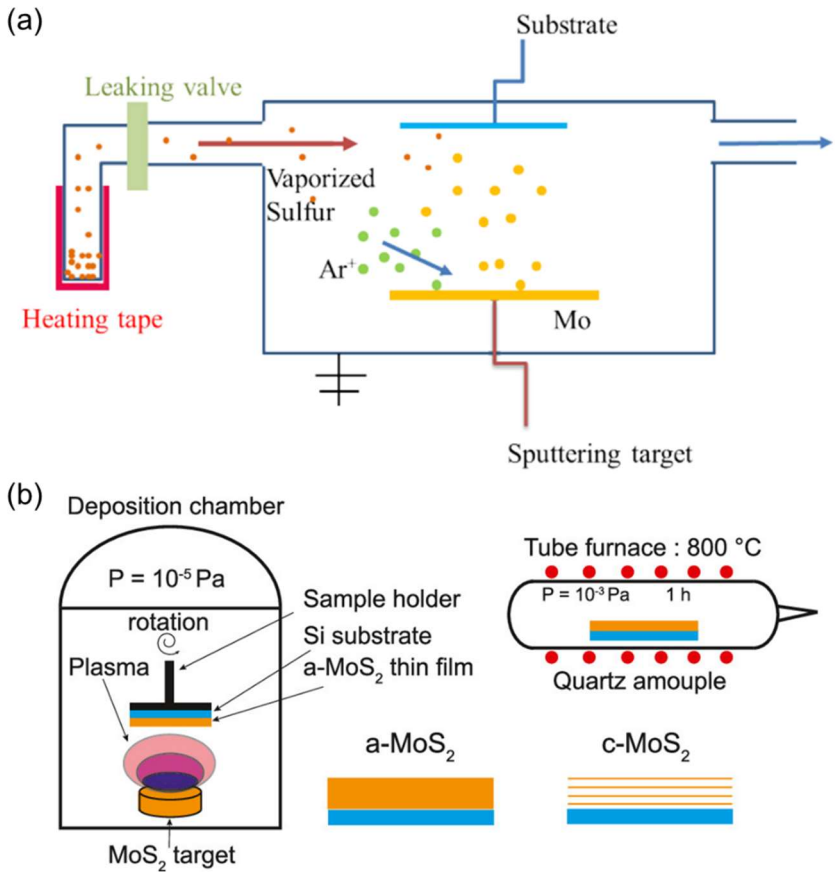

Figure 1.17. Schematic of sputtering deposition of TMD thin films. (a) Schematic of one-step reactive sputtering deposition.[63] (b) Schematic of two-step sputtering deposition that consists of non-reactive sputtering deposition of amorphous MoS_2 and post-annealing for transforming the amorphous MoS_2 into crystalline.[64] Reproduced from Refs. [63,64].

PLD is performed using high-power laser pulses to ablate target material, producing a plasma plume that expands rapidly away from the target surface (see schematic in **Figure 1.18**).[66] A high supersaturation of ablated material condenses on an appropriately placed substrate in tens of microseconds, thereby providing high nucleation density that can increase the coverage of product film. By adjusting the laser fluence and repetition rate of the laser pulse, the thickness of TMD thin films can be regulated. Compared to other methods, PLD offers a primary advantage of transferring the stoichiometry of target material to product film by adjusting the laser fluences. At low laser fluences, target materials are locally heated and thereby evaporated by absorbing the laser energy. At high laser fluences, PLD induces ablation that can better transfer stoichiometry of target material than pure evaporation. However, too high laser fluences may cause self-sputtering that worsens the stoichiometry of product film. This self-sputtering of the product film can be reduced by adding a background gas to modulate the deposition pressure. To further improve the film quality, reactive gases can be added to background gas. Serrao *et al.* reported the PLD synthesis of thin MoS_2 films (1 – 15 layers) on Al_2O_3, GaN, and SiC-6H substrates using targets composed of MoS_2 and excess sulfur powder.[67] Despite high uniformity and crystallinity, the film shows a Mo:S atomic ratio of 1:4 that corresponds to a sulfur-rich product. To improve the film quality, Serna *et al.* optimized the target composition of PLD growth and achieved a better Mo:S ratio close to 1:2 for large-area MoS_2 with layers ranging from 1 to 10.[68]

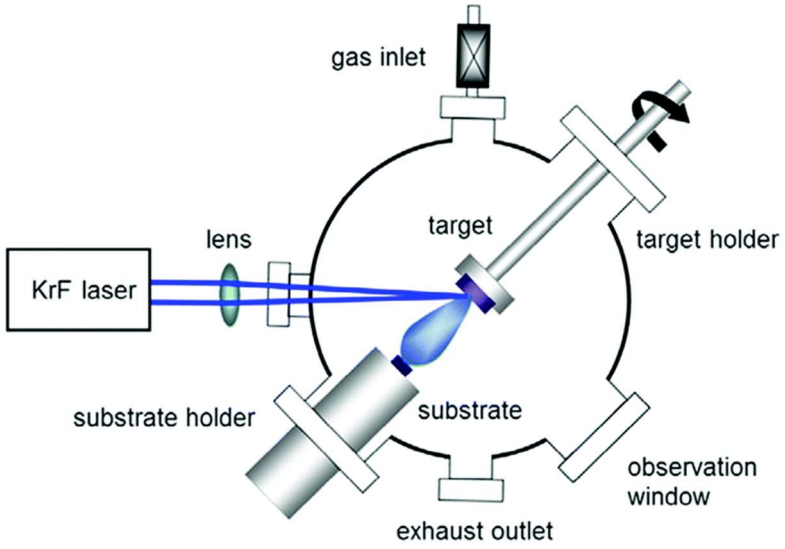

Figure 1.18. Schematic of a typical PLD system. Reproduced from Ref. [66].

Chapter 2 Defects in 2D TMDs

To better understand how TMD-based devices can be optimized, it is essential to understand the role of defects. Three critical questions arise. The first is type of defects that occur in two-dimensional (2D) TMDs. The second is how these defects affect the electronic structure. The third is how to identify these defects. Answers to these questions can provide insights into how to engineer the defects to optimize the properties of 2D TMDs. This chapter describes defects in 2D TMDs.

2.1 Type of Defects and Their Formation Energy in 2D TMDs

Generally, defects in crystalline materials can be categorized into three types according to their dimensions: zero-dimensional (0D) point defects, one-dimensional (1D) line defects (dislocations), 2D planar defects (grain boundaries, phase boundaries), and 3D volume defects (pores, cracks, voids). Owing to the reduced dimensionality of the 2D crystals, the number of defect types that can exist is reduced compared to 3D semiconductors. Only point defects, line defects (grain boundaries and edges), and planar defects (wrinkling, folding, and scrolling) can exist in atomically thin 2D crystals.

Due to the high surface-to-volume ratio, point defects in 2D TMDs have significant influence on their optoelectronic properties. Therefore, I focus on them in this chapter and remaining thesis. Point defects refer to atomic defects within lattice sites that locally break the crystal periodicity, regardless of the crystal dimension. They are usually classified as intrinsic point defects (*i.e.*, vacancies, interstitials, and antisites) and extrinsic point defects (*i.e.*, impurities, which could occupy substitutional or interstitial sites).[69] When different types of point defects are generated in a crystal, these defects may combine to form defect complexes. In 2D TMDs, intrinsic point defects include abundant chalcogen vacancies (V_{X}) while transition metal vacancies (V_{M}) are rarely found with a lower defect density. Extrinsic point defects include oxygen substitution for chalcogen atoms ($\mathrm{O_X}$) and other metal substitution (Al, Fe, Si, Cu, Mn, Cr, Ni, and V) for transition metal atoms ($\mathrm{A_X}$), as shown in **Figure 2.1**.

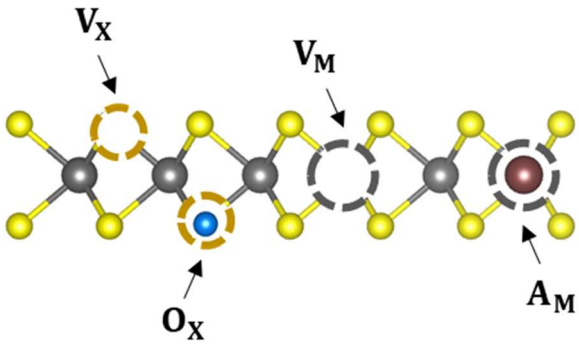

Figure 2.1. Schematic of point defects in 2D MoS_2.

The formation energy of point defects (E_{fe}) depends on the chemical potential of point defects that is often defined by experimental growth conditions.[70] With a given set of chemical potentials, the concentration of defects has an exponential dependence on formation energy.[71] The dominant defects are those with the lowest formation energy. For example, the E_{fe} for atomic vacancies in TMDs can be calculated as:

$$E_{fe} = E_{\mathrm{vac}} - [E_{\mathrm{undef}} - n_{\mathrm{M}} m_{\mathrm{M}} - n_{\mathrm{X}} m_{\mathrm{X}} - q(E_{\mathrm{F}} + E_{\mathrm{VBM}})] \quad (2.1)$$

where E_{undef} and E_{vac} are the energies of the defect-free supercell and defective supercell with vacancy at charge state q, respectively.[72] E_{F} corresponds to the Fermi level and E_{VBM} is the energy of the valence band maximum. n_{M} and n_X are the numbers of metal and chalcogen vacancies, respectively. m_{M} and m_{X} are the chemical potential of the displaced metal and chalcogen atoms, which are taken as the partial derivative of Gibbs free energy of the isolated atoms. In particular, both m_{M} and m_{X} in TMDs depend on the thickness of nanosheets and are smaller for monolayers than for bulk as a result of the limited available space around vacancies in monolayers.[73] Consequently, the formation energy of vacancies is smaller for free-standing monolayer TMDs than for bulk TMDs. Calculated formation energies of typical intrinsic point defects in monolayer MoS_2 as a function of chemical potential of sulfur are shown in **Figure 2.2**.[74] There are eight types of possible intrinsic point defects in MoS_2: single sulfur vacancy (V_{S}), double sulfur vacancy (V_{S2}, vertically aligned), single Mo vacancy (V_{Mo}), vacancy complex (V_{MoS2}, V_{MoS3}, V_{MoS6}), and antisites ($S2_{\mathrm{Mo}}$ and Mo_{S2}). By comparing the formation energies of all possible intrinsic point defects, the Mo-related intrinsic defects (V_{Mo} , V_{MoS2}, V_{MoS3}, V_{MoS6}, $S2_{\mathrm{Mo}}$, and Mo_{S2}) are found to have high formation energies above 4 eV in both Mo-rich and S-rich growth conditions, while sulfur vacancy defects (V_{S} and V_{S2}) have lower formation energies. Thus, density of Mo-related intrinsic defects in MoS_2 monolayers is low while the density of sulfur vacancy defects is higher.

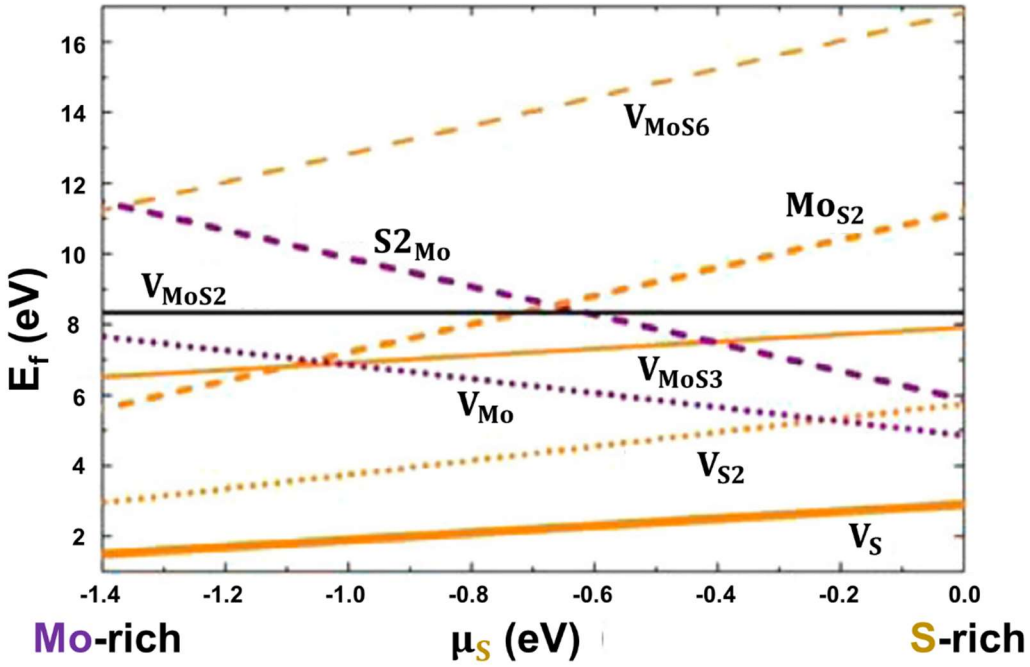

Figure 2.2. Calculated formation energies of intrinsic point defects in MoS_2 monolayer as a function of chemical potential of sulfur (μ_S). Single sulfur vacancy (V_S) has the lowest formation energy among all possible point defects. Reproduced from Ref. [74].

2.2 Influence of Defects on Electronic Structure of 2D TMDs

In defect-free semiconducting crystals, the photoexcited free electron-hole pairs or excitons can undergo band-to-band radiative recombination that contributes to optical emission. In **Figure 2.3a**, the energy *vs* density of states of a semiconductor with a bandgap (E_g) is shown.[75] The conduction band (CB) and valence band (VB) along with shallow and deep trap energy levels are indicated. Radiative and non-radiative processes are also shown. In **Figure 2.3b**, various recombination processes of photoexcited carriers are shown.[76] In radiative recombination, photoexcited electrons in the conduction band recombine with holes in the valence band, releasing excess energy as photons. When defects are present, extra electronic states may be created inside the bandgap that act as photocarrier traps to mediate radiative/nonradiative recombination. After photoexcitation, electrons in the conduction band (CB) can directly recombine with holes in the valence band (VB) ①. A fraction of photoexcited electrons can get trapped by the unoccupied defect levels (electron trap states) ②. The trapped electrons can undergo recombination with holes in VB ③. Similarly, holes

can get trapped by the occupied defect levels (hole trap states) ④ and then recombine with electrons from CB ⑤ or the trapped electrons ⑥.

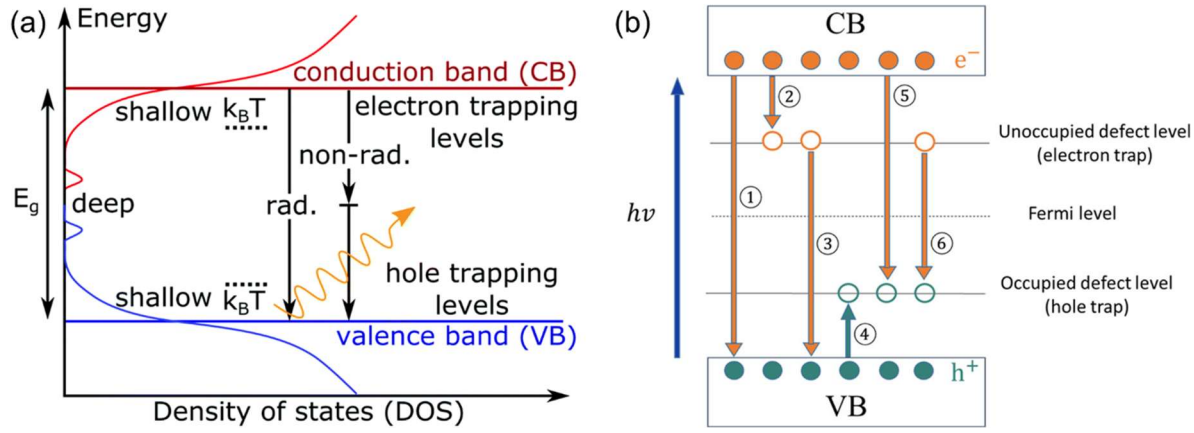

Figure 2.3. (a) Schematic of shallow and deep traps in the energy band diagram.[75] (b) Transition of electrons and holes induced by defect level. The electrons are shown in orange and the holes are shown in emerald.[76] Reproduced from Refs. [75,76].

Depending on the energy difference between trap states and band edges, defects can be classified as shallow or deep traps.[77] If the energy difference is smaller (or larger) than the thermal energy of k_BT (~26 meV at room temperature), the traps are shallow (or deep) traps. For shallow defect states, the defect states close to conduction band easily trap electrons while defect states near valence band easily trap holes.[78] These shallow trapped electrons/holes tend to be easily excited back to conduction band/valence band. The deeply trapped carriers are less likely to be de-localized. Deep defect states typically serve as dominant recombination centers.[79] For electron trapping, the electron trapping rates (R_{cn}) and thermal emission rates (R_{en}) can be written as[80]:

$$R_{\mathrm{cn}} = C_{\mathrm{n}} N_{\mathrm{t}} [1 - f(E_{\mathrm{t}})] n, \qquad R_{\mathrm{en}} = E_{\mathrm{n}} N_{\mathrm{t}} f(E_{\mathrm{t}}) n \tag{2.2}$$

where C_{n} and E_{n} are the trap capture and thermal emission coefficients, in units of cm^3/s. N_{t} is the number of trap states. $f(E_{\mathrm{t}})$ is the probability that a trap of energy E_{t} is occupied. $1 - f(E_{\mathrm{t}})$ is the probability that a trap of energy E_{t} is empty. n is the concentration of free electrons. C_{n} and E_{n} can be calculated by:

$$C_{\mathrm{n}} = v_{\mathrm{th}}\sigma_{\mathrm{n}}, \qquad E_{\mathrm{n}} = C_{\mathrm{n}}N_{\mathrm{C}}\, exp(\frac{E_{\mathrm{C}}-E_{\mathrm{t}}}{k_{\mathrm{B}}T}) \tag{2.3}$$

v_{th} is the thermal velocity of carriers, σ_{n} is the electron/hole capture cross section. N_{C} is effective density of states for electrons. E_{C} is conduction band energy, and E_{t} is trap state energy, relative to vacuum level. k_B is Boltzmann constant and T is temperature.

At thermal equilibrium, $f(E_{\mathrm{t}})$ is given by the Fermi-Dirac distribution:

$$f(E_{\mathrm{t}}) = \frac{1}{1 + exp(\frac{E_{\mathrm{t}} - E_{\mathrm{F}}}{k_{\mathrm{B}}T})}$$

Whether a defect is deep or shallow can be identified by its charge transition levels. That is, Fermi energy levels where transitions between two different charge states of a localized defect occur with the same formation energy. For MoS_2, sulfur vacancies have two energetically favorable charge states: neutral and −1, as shown in **Figure 2.4**.[81] In Kröger–Vink notation, sulfur vacancies (V_{S}) can be written as V_{S}^{X} (neutral state) and V_{S}' (−1 charge state). The charge states of the defect depend on the Fermi level of the system. For sulfur vacancies in monolayer MoS_2, when the Fermi level is located close to the valence band, the dominant charge state is the neutral state, whereas the −1 charge state is favorable when the Fermi energy is close to the conduction band. Molybdenum vacancies (V_{Mo}) and molybdenum interstitials (Mo_i) also have one stable neutral state and another stable charged state, that is, $V_{\mathrm{Mo}}^{X}/V_{\mathrm{Mo}}'$ for V_{Mo}, and Mo_i^{X}/positively charged $\mathrm{Mo}_i^{\bullet}$ for Mo_i. V_{S} has 0/−1 charge transition level at E_{Fermi} = +1.7 eV, therefore V_{S} is a deep defect in MoS_2. Similarly, Mo_i with +1/0 charge transition level at E_{Fermi} = +0.3 eV and V_{Mo} with 0/−1 charge transition level at E_{Fermi} = +1.1 eV are also deep defects.

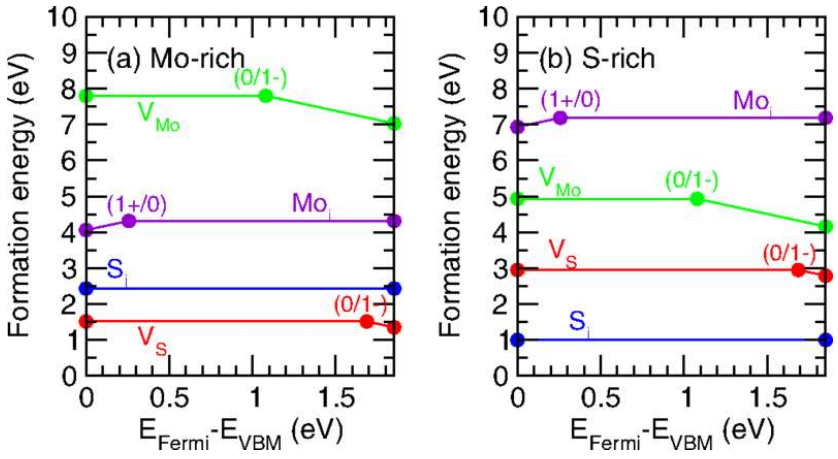

Figure 2.4. Calculated formation energies of isolated intrinsic point defects in a MoS_2 monolayer in various stable (energetically the most favorable) charge states as a function of the Fermi level inside the bandgap in the (a) Mo-rich and (b) S-rich limit conditions. Only the charge states that are the most energetically favorable at a given Fermi level are shown for each geometrical defect. Reproduced from Ref. [81].

2.3 Visualization of Defects

Scanning transmission electron microscopy (STEM) and scanning tunneling microscopy/spectroscopy (STM/STS) have been extensively used to image and identify atomic-scale defects in 2D TMDs. **Figure 2.5** shows high-angle annular dark-field (HAADF) STEM image of monolayer MoS_2 with various atomic vacancies created by helium ion irradiation.[82] In HAADF-STEM images, heavier atoms show higher contrast, therefore the brightest atoms in **Figure 2.5a** are Mo atoms (Z = 42) while sulfur atoms show darker contrast (Z = 16). Three types of vacancies can be seen: Single sulfur vacancy, double sulfur vacancy (two single sulfur vacancies vertically aligned), and single Mo vacancy. **Figure 2.5b** shows contrast intensity profile extracted along 4 lines from **Figure 2.5a**. Taking the intensity profile of line 1 (shown in black) without any vacancies as reference, single sulfur vacancies show relative reduction of contrast intensity by ~30% while double sulfur vacancies show a reduction of ~45%. It can also be seen that the contrast intensity on Mo vacancy sites becomes 0%.

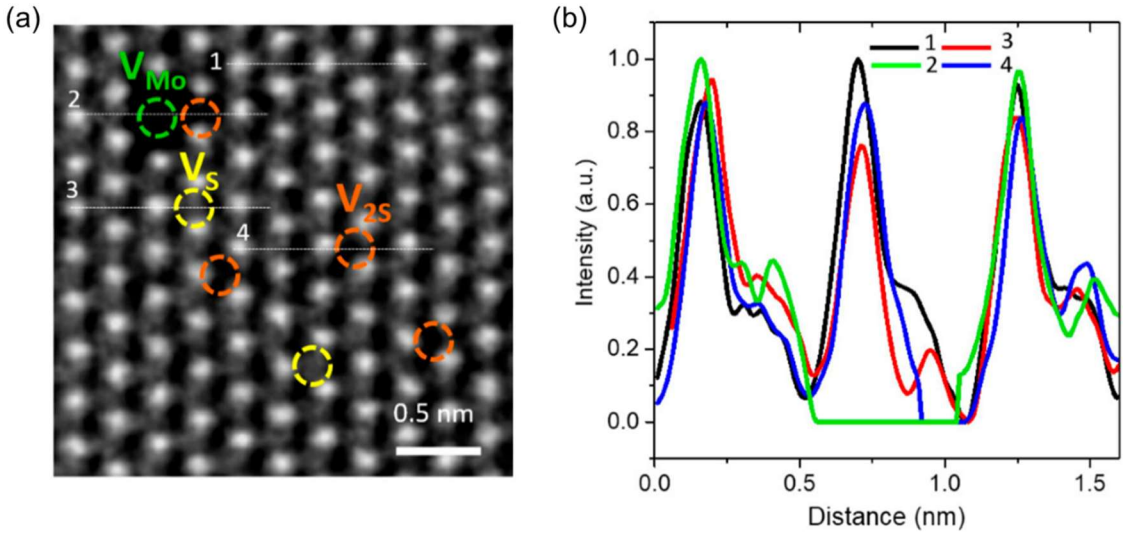

Figure 2.5. (a) HAADF-STEM image of defective monolayer MoS_2 showing three types of vacancies: Single sulfur vacancy (V_S, yellow circles), double sulfur vacancy (V_{2S}, orange circles), and single molybdenum vacancy (V_{Mo}, green circle). (b) ADF intensity line profiles taken along dotted lines 1 – 4 in image (a). Reproduced from Ref. [82].

ADF-STEM imaging can also be used to characterize metal impurities. It can be co-used with atomic-scale energy dispersive x-ray spectroscopy (EDS) and electron energy loss spectroscopy (EELS) mapping to identify elemental nature of impurity metal atoms. EDS and EELS are useful in distinguishing atoms with similar atomic number and consequent similar contrast. **Figure 2.6** shows ADF-STEM images and corresponding EELS maps of CVD-grown monolayer MoS_2.[83] In **Figure 2.6a**, it can be seen that some Mo sites show darker contrast, indicating the presence of low contrast atoms on Mo sites. EELS map for the blue square in **Figure 2.6b** indicates the presence of Cr in the low contrast region. This is inferred from EELS intensity map in **Figure 2.6c**, which shows higher intensity between 570 – 590 eV, corresponding to $L_{3,2}$ edge (transitions from 2*p* to 3*d*) of Cr. EELS from red square in **Figure 2.6d** shows that the low contrast region (indicated by yellow arrow) corresponds to V atom as indicated by EELS intensity map in **Figure 2.6e**. The actual EELS peaks from V and Cr are shown in **Figure 2.6f**.

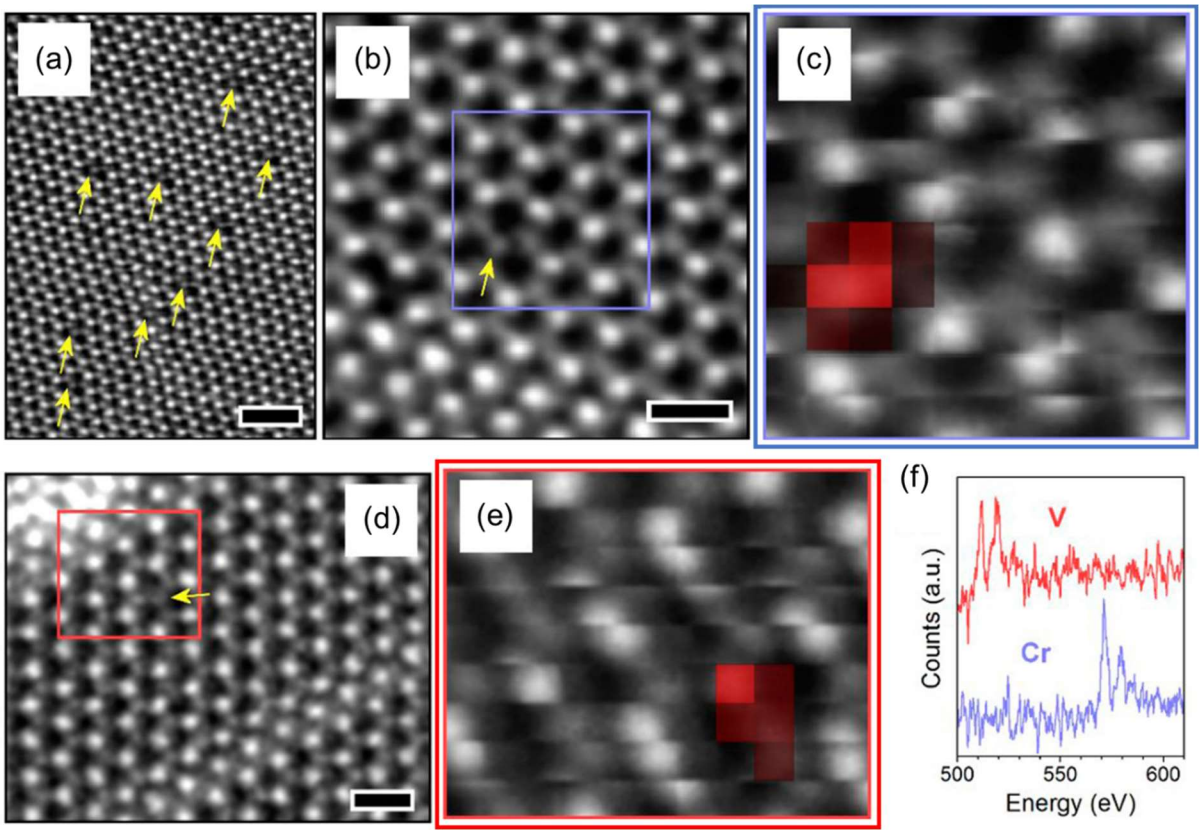

Figure 2.6. (a) ADF-STEM image of MoS_2 with low contrast single atoms on some Mo sites, indicated by yellow arrows. Scale bar = 1 nm. (b,d) ADF-STEM image of two regions for EELS mapping. Scale bar = 0.5 nm. (c,e) The integrated EELS intensity maps acquired in the energy range of (c) Cr $L_{3,2}$ edge (570 – 590 eV) for blue region in image (b) and (e) V $L_{3,2}$ edge (505 – 525 eV) for red region in image (d). Higher red squares correspond to higher integrated EELS intensity. (f) EELS spectra showing Cr $L_{3,2}$ and V $L_{3,2}$ edges. Reproduced from Ref. [83].

One aspect of STEM imaging that must be considered is that high-voltage electron beam can generate knock-on damage and create additional defects in 2D TMDs. As Qiu *et al.* reported, there was no obvious new sulfur vacancy observed in a 12×12 nm MoS_2 monolayer within 44 s exposure under 80 keV electron beam irradiation.[84] After 62 s exposure, the number of sulfur vacancies increased from 65 to 70, and the average vacancy generation rate was calculated to be 5.6×10^{10} cm^{-2} s^{-1}. When the irradiation time was long enough, other defects such as line defects and nanopores also appeared. Therefore, great care needs to be taken in STEM measurements to minimize defects produced by the electron beam. For example, the electron beam energy needs to be minimized, as well as the irradiation time. This can be achieved by

testing the imaging conditions on one area and then quickly moving to an adjacent area to capture images.

Oxygen substitution for chalcogen in 2D TMDs is difficult to image and characterize with STEM because of low contrast. However, oxygen can induce changes in electronic structure of 2D TMDs. Therefore, Scanning tunneling microscopy/spectroscopy (STM/STS) can be used to image oxygen and its local electronic structure, respectively. STM measures tunneling current between a metallic tip and a conducting sample. When it is performed in constant height mode, plot of tunnelling current as a function of tip position is generated; In constant current mode, plot of tip height as a function of tip position is generated. STM plot typically matches sample surface structure, while STS differential conductance (dI/dV) spectra provide information about local electronic structure of the sample. In STM imaging, atomic resolution can be achieved using atomically sharp tips. **Figure 2.7** shows STM images and STS spectra of $MoSe_2$ monolayer grown by molecular beam epitaxy (MBE).[85] STM images of oxygen substitution for top and bottom Se atoms in $MoSe_2$ are shown in **Figure 2.7a,b**. In **Figure 2.7a**, oxygen substituted for top (left side of image) and bottom (right side of image) Se atoms are shown. The sample voltage (V_S) in **Figure 2.7a** is –1.55V, which means that states near the valence band edge are probed. It can be seen that O_{Se} top site appears darker and oxygen substitution for bottom Se (O_{Se} bottom) appears brighter. This is also true for states near the conduction band edge, as shown in **Figure 2.7b**. **Figure 2.7c** shows dI/dV spectra measured on pristine $MoSe_2$ and oxygen substitution for top Se (O_{Se} top), respectively. The O_{Se} top site shows an additional defect resonance peak below the valence band edge.

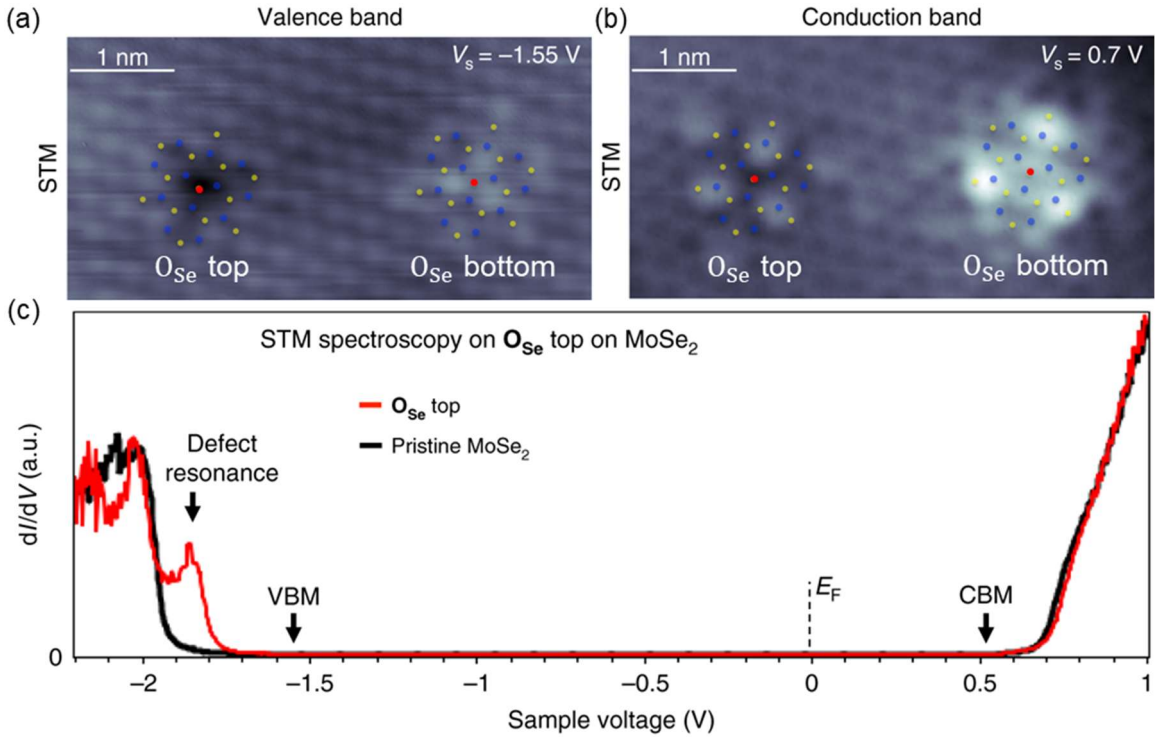

Figure 2.7. (a,b) STM images of $MoSe_2$ monolayer with oxygen substitution for top sulfur (O_{Se} top) and bottom sulfur (O_{Se} bottom) measured at (a) valence and (b) conduction band edges. Se (yellow dots), Mo (blue dots), and O (red dots) are shown. (c) Differential conductance (dI/dV) spectra acquired on pristine $MoSe_2$ and O_{Se} top site, showing an additional defect resonance peak below the valence band edge. Reproduced from Ref. [85].

STM/STS can also be extended to characterize vacancies and metal impurities. **Figure 2.8** shows atomic resolution STM images and STS spectra of CVD-grown MoS_2 monolayer with single sulfur vacancies under different biases.[86] **Figure 2.8a,b** shows STM images taken under ±0.7 V bias, in which a single sulfur vacancy appears as a dark spot. The dI/dV spectrum of the single sulfur vacancy shows valence band maximum (VBM) at around −1.6 V and the conduction band minimum (CBM) at around +0.7 V. This corresponds to a bandgap of $E_g = E_{CBM} - E_{VBM}$ = 2.25 eV. The single sulfur vacancy introduces an additional sharp peak at around +0.35 eV that arises from in-gap defect states.

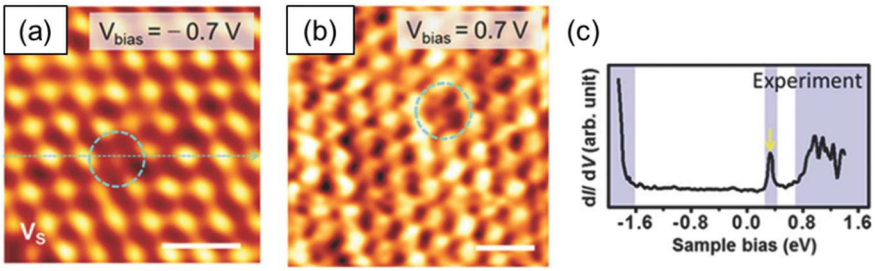

Figure 2.8. STM imaging of MoS_2 monolayer with single sulfur vacancies generated by thermal annealing in Ar/H_2 (50 sccm: 5 sccm). (a,b) STM images of MoS_2 monolayer with a single sulfur vacancy recorded under ±0.7 V bias. (c) Differential conductance dI/dV spectrum obtained at the single sulfur vacancy. Scale bar is 0.6 nm in (a) and 0.5 nm in (b). Reproduced from Ref. [86].

However, both STEM and STM measurements have several practical disadvantages, including time-consuming and very small probing regions. Additionally, STEM requires ultrahigh vacuum (UHV) and suffers from beam-induced defects. The current maps measured by STM sometimes also deviate from the real surface structures due to current fluctuations caused by a rough topography. These hinder the identification of defects. Recently, conductive atomic force microscopy (CAFM) that can be operated under ambient conditions has been explored for atomic-resolution imaging of defects in 2D TMDs. Similar to STM, CAFM also measures current as a function of tip position to produce current maps while measuring topography simultaneously but independently. Therefore, CAFM can more accurately distinguish whether a current change is a real change or not. When the conductive tip is in contact with sample surface, a bias can be applied to sample and cause current to flow from sample to tip, as shown in **Figure 2.9a**.[87] Using this setup to measure exfoliated WSe_2 monolayer with a sample bias of 0.05 V, an atomic-scale defect can be identified with lower conductance (**Figure 2.9b**).

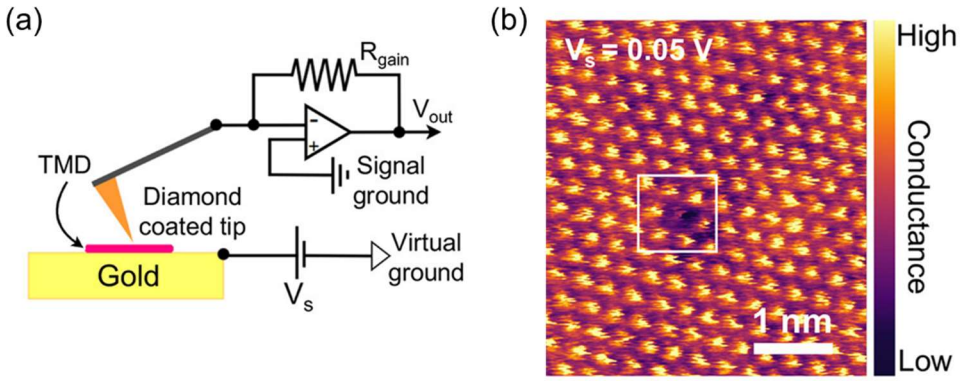

Figure 2.9. CAFM image of defects in exfoliated WSe_2 monolayer. (a) Experimental setup for CAFM measurement. (b) Atomic resolution CAFM image of WSe_2 monolayer, showing an atomic-scale defect. Reproduced from Ref. [87].

Since STEM, STM, and CAFM imaging are all limited to microscopic scale and subsequently not available for locating and identifying point defects at macroscale scale, dark-field optical microscopy has been proposed to analyze macroscopic distribution of point defects. Compared with bright-field optical microscopy, dark-field optical microscopy may show stronger contrast on defects arising from enhanced light scattering at defects. To further increase the contrast, defect sites are often anchored with metal nanoparticles such as Ag nanoparticles (size of several hundred nanometers). In **Figure 2.10a**, it can be seen that when MoS_2 monolayer is decorated with Ag nanoparticles, various defects are clearly visible in dark-field optical microscope image, including what the authors claim to be atomic-scale defects, grain boundaries, and edges. Multilayer regions can also be clearly distinguished from monolayer regions.[88] Similarly, point defects (bright spots in the basal plane of flakes) and grain boundaries can also be observed in WS_2 and WSe_2 monolayers (**Figure 2.10b,c**). Compared to MoS_2 and WS_2 monolayers, less bright spots are observed in WSe_2 flakes, indicating a smaller density of point defects. Hence dark-field optical microscopy can be potentially used as a complementary technique to locate and identify defects in macroscale for 2D TMDs. However, it is unclear whether defects labelled as "point defects" in **Figure 2.10a** are real atomic defects such as those identified using techniques described above. Further study is required to understand whether anchoring of Ag atoms on atomic defects can render them visible in optical microscopy.

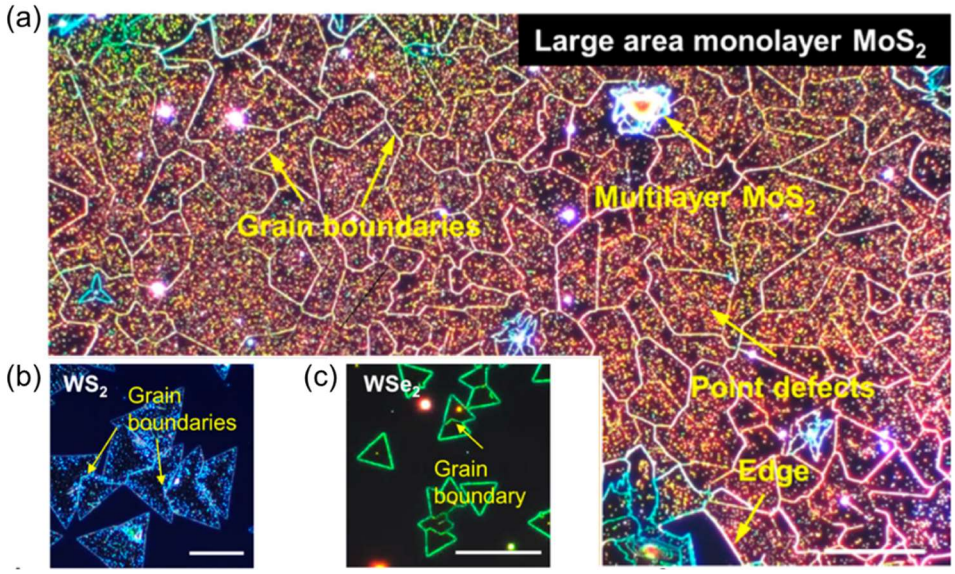

Figure 2.10. (a) Dark-field optical microscope image of MoS_2 monolayer decorated with Ag nanoparticles, showing defects. (b–c) Dark-field optical microscope images of defects in WS_2 and WSe_2 monolayers. Scale bar is 20 μm. Reproduced from Ref. [88].

Chapter 3 Experimental Methods: Synthesis & Characterization

This chapter describes the material synthesis and characterization methods used in my PhD research. Mechanically exfoliated and atmospheric-pressure chemical vapor deposition (CVD) grown high-quality monolayer 2D TMDs were used in this study. Annealing of 2D TMDs was done to generate the defects. X-ray photoelectron spectroscopy (XPS), absorption spectroscopy, photoluminescence (PL) spectroscopy, Raman spectroscopy, atomic force microscopy (AFM), and X-ray diffraction (XRD) were used to characterize the materials.

3.1 Synthesis of 2D TMDs

Mechanical exfoliation. Monolayer TMDs, including MoS_2, WS_2, $MoSe_2$, and WSe_2, were mechanically exfoliated in air on SiO_2 (300 nm)/Si substrates from commercial bulk crystals purchased from *2D Semiconductor*. The polydimethylsiloxane (PDMS)-assisted exfoliation & dry transfer method[89] used to produce monolayer TMDs is shown in **Figure 3.1**. This method is based on the viscoelastic properties of PDMS. The bulk crystal was first exfoliated onto a scotch tape and then attached to a PDMS stamp on a glass slide ①. After peeling off the scotch tape, flakes were left on the PDMS stamp. Monolayer flakes (1L) were identified using Nikon Eclipse LV150N optical microscope. An example of a monolayer and multilayer flake is shown in **Figure 3.2**. Then the glass slide was attached to the transfer stage, with the PDMS stamp placed face-down ②. Using a micromanipulator, the target flake was precisely aligned with the target substrate (*e.g.*, 300 nm SiO_2/Si) ③. To deposit the target flake, the PDMS stamp was brought into contact with the target substrate and heated to 60 °C for 1.5 min to soften ④. Then the PDMS stamp was raised to detach from the substrate ⑤, leaving the target flake on the substrate ⑥.

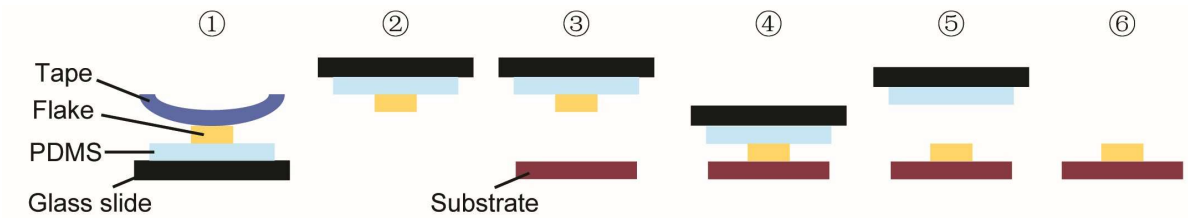

Figure 3.1. Schematic of PDMS-assisted exfoliation & dry transfer. Steps ①– ⑥ are described in the text.

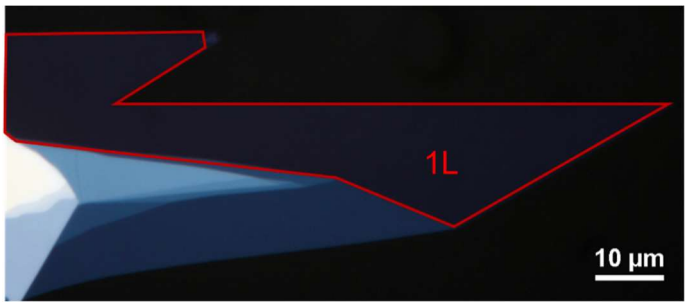

Figure 3.2. Optical microscope image of mechanically exfoliated MoS_2 on PDMS. The monolayer region (1L) is marked in red.

In the step ④, the PDMS/flake/substrate stack was heated to 60 °C for 1.5 min for transfer. This heating condition was chosen by comparing PL spectra of three transferred monolayered flakes measured at room-temperature (RT, ~300 K): one directly transferred without heating, one transferred at 60 °C for 1.5 min, and one transferred at 60 °C for 2 min (**Figure 3.3**). The RT PL spectra show the characteristic A^- trion/A exciton (A^-/A) and B exciton peaks (see **Section 1.3** for details of exciton and trion formation in 2D TMDs). The one transferred at 60 °C for 1.5 min shows the lowest proportion of A^- trions against A excitons, which is the closest out of the three samples to the PL of monolayer MoS_2 reported in the literature.[30] Using cleaning methods described in **Section 3.3** to treat transferred monolayered flakes, the proportion of A^- trions against A excitons can be further reduced.

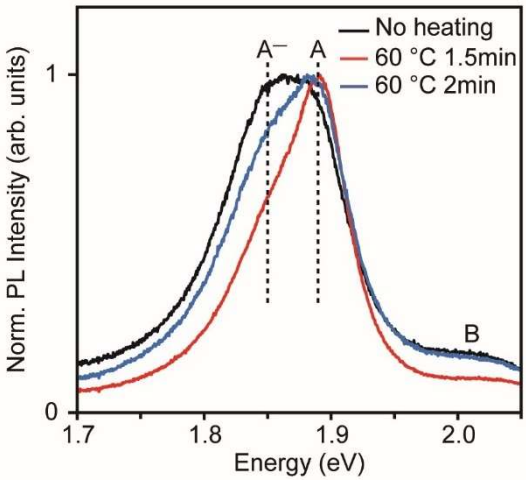

Figure 3.3. RT PL spectra of three monolayer MoS_2 flakes transferred from PDMS onto SiO_2/Si substrate: one directly transferred without heating, one transferred at 60 °C for 1.5 min, and one transferred at 60 °C for 2 min.

Atmospheric-pressure CVD growth. Monolayer MoS_2 was grown on SiO_2 (300 nm)/Si substrates by atmospheric-pressure CVD using MoO_3 and sulfur powders as precursors, as shown in **Figure 3.4**. Thermo Scientific Lindberg Blue M single-zone tube furnace was used for CVD growth and remaining annealing studies in this thesis. SiO_2 (300 nm)/Si wafers were treated in UV-ozone atmosphere for 15 mins to improve the wettability of the surface. Promoter NaOH was dissolved in water with a concentration of 4 mg/mL and 100 µL solution was uniformly spin coated on SiO_2/Si wafers. MoO_3 powder was dispersed in water with a concentration of 0.5 mg/mL, after which 250 µL dispersion was drop-cast in alumina boat 1 (see **Figure 3.4**) and heated to 110 °C until the boat was completely dry. 30 mg sulfur powder was placed in alumina boat 2. Alumina boats 1 and 2 were placed in the center and upstream of a 1-inch diameter quartz furnace tube I. SiO_2/Si wafers were placed face-down on boat 1. The furnace was heated to 700 °C at a rate of 45 °C/min and maintained for 10 min for the growth of MoS_2 flakes. High-purity N_2 (99.999%) was used as carrier gas. At ~680 °C, the tube was slightly shifted downstream by ~1.5 cm to vaporize the sulfur powder at ~200 °C. The flow rate of N_2 was adjusted from 260 to 60 standard cubic centimeters per minute (sccm) to allow chemical reaction of MoO_3, NaOH, and sulfur to grow MoS_2 on SiO_2/Si wafer. After growth, the furnace was cooled down to RT and samples were collected.

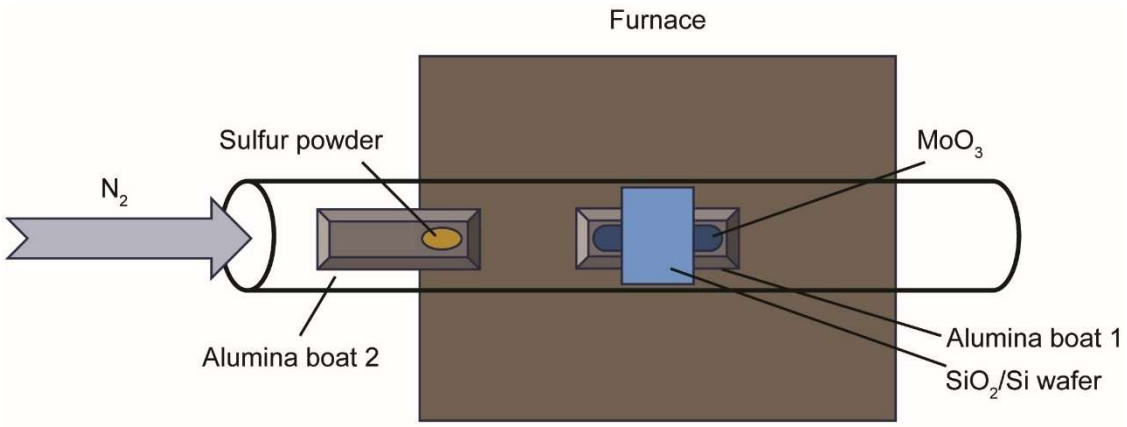

Figure 3.4. Schematic of atmospheric-pressure CVD growth of monolayer MoS_2 using a single-zone furnace. MoO_3 and sulfur powders are used as precursors, and NaOH is used as promoter. N_2 is supplied as carrier gas.

The possible reaction mechanism has been proposed by Lee's group, as follows[90]: $4NaOH(s) + MoO_3(s) + SiO_2(s) \rightarrow Na_2MoO_4(s) + Na_2SiO_3(s) + 2H_2O(g)$; $2Na_2MoO_4(s) + 7S(g) \rightarrow 2MoS_2(s) + 2Na_2O(s) + 3SO_2(g)$. They have shown that the reaction caused the corrosion of SiO_2 surface and created the hole features. Consistent with their work, I also observed similar hole features in atomic force microscopy (AFM) images of CVD-grown MoS_2 on SiO_2/Si wafer (**Figure 3.5a**). The height profile taken on one hole shows a depth of ~20 nm (**Figure 3.5b**).

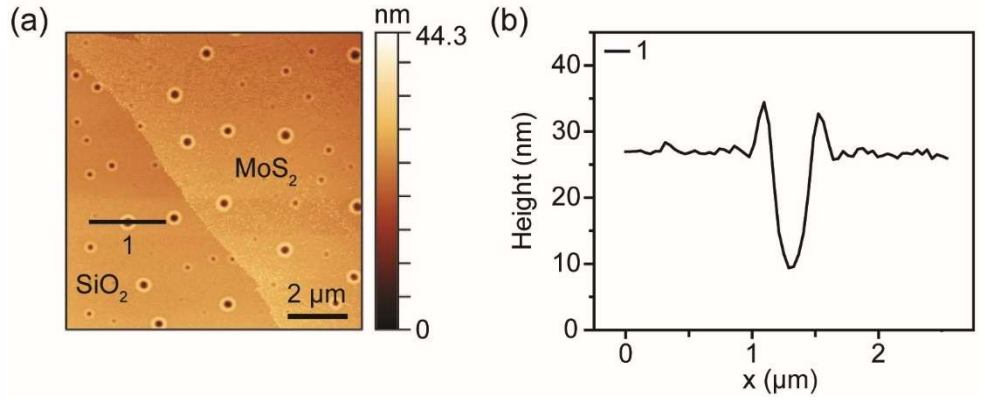

Figure 3.5. AFM image (a) and height profile (b) of CVD-grown MoS_2 on SiO_2/Si wafer, showing hole features on SiO_2 with a depth of ~20 nm.

This CVD growth recipe was originally derived by Dr. Yan Wang in our group using different amounts of precursors. Based on that, I developed my own recipe by fixing the amounts of NaOH (4 mg/mL, 100 μL) and sulfur (30 mg) and varying the amount of MoO_3 (0.5 mg/mL). The shape morphology evolution of growth products was monitored by optical microscopy, as shown in **Figure 3.6**. With 1 mL MoO_3, only dense seeds were obtained without proper monolayer flakes. Decreasing to 250 μL MoO_3, isolated monolayer flakes were grown, showing near-triangle shape. However, further decreasing the amount of MoO_3 (50 μL) did not generate larger flakes. Instead, the flakes showed dendritic shapes. Therefore, I used 250 μL MoO_3 for my own recipe.

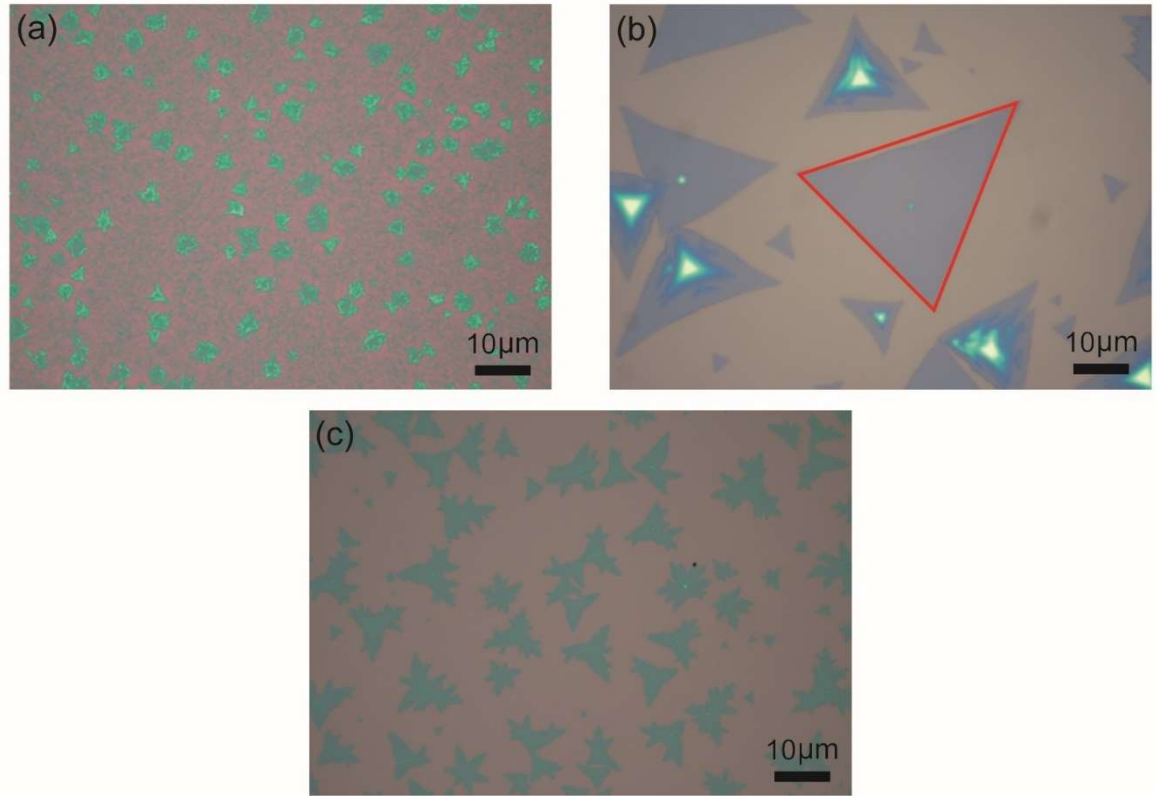

Figure 3.6. Optical microscopy images of CVD-grown MoS_2 grown using the same amounts of NaOH (4 mg/mL, 100 μL) and sulfur (30 mg), but various amounts of MoO_3. (a) MoO_3: 0.5 mg/mL, 1 mL. (b) MoO_3: 0.5 mg/mL, 250 μL. (c) MoO_3: 0.5 mg/mL, 50 μL.

Both mechanically exfoliated MoS_2 and CVD-grown MoS_2 have been shown that they are dominated by sulfur vacancy defects, as shown in **Figure 3.7**.[91] Hong *et al*. has reported that mechanical exfoliation generates a lower native defect density than CVD growth by quantifying defects through atomically resolved annular dark-field scanning transmission electron microscopy (ADF-STEM) imaging.[91] Hence, in this thesis, I mostly focus on mechanically exfoliated TMDs.

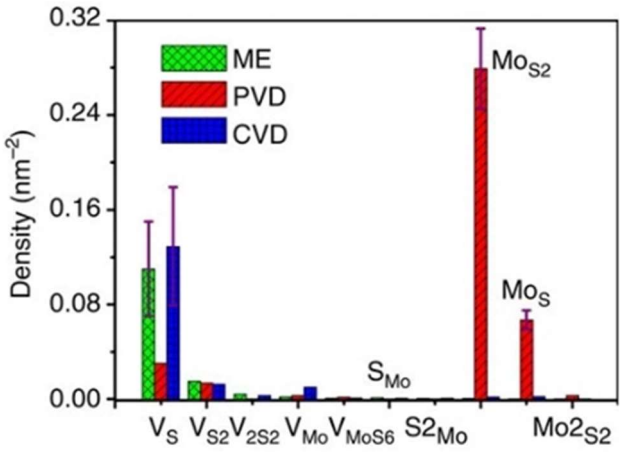

Figure 3.7. Histograms of defect density across various point defects in monolayer MoS_2 synthesized by mechanical exfoliation (ME), CVD, and physical vapor deposition (PVD). Reproduced from Ref. [91].

3.2 Characterization of 2D TMDs

3.2.1 Atomic Force Microscopy (AFM)

As discussed in **Section 1.2** and **1.3**, the semiconducting performance of 2D TMDs is strongly related to their layer numbers. Only monolayer TMDs are direct bandgap semiconductors that are ideal for investigating the influence of defects. Hence locating and identifying monolayers are important. AFM was routinely used to image and characterize the thickness (layer numbers) of 2D flakes (see **Section 5.2** for details). AFM consists of a cantilever with a sharp tip fixed to its end, a piezoelectric scanner, and an optical detection system composed of a laser beam, a laser diode, and a photodetector, as shown in **Figure 3.8**.[92]

AFM images are generated by scanning the sharp tip over sample surface. When the tip approaches sample surface, the attractive/repulsive forces between tip and sample surface can bend the cantilever. The deflection of cantilever can be measured by reflection of laser light from the reflective back side of cantilever into photodiode. The photodiode converts the light reflection into an electrical feedback loop which is controlled to its setpoint value by adjusting the height of cantilever. Using the height variance, a three-dimensional surface topography can be acquired. AFM is usually operated in three modes, contact mode, tapping mode, and non-contact mode. In contact mode, the tip is in continuous contact with sample surface, operated at short-range repulsive force regime. The feedback loop controls the cantilever

deflection to be constant and applies constant force to sample. However, the frictional and adhesive forces are strong and may damage the sample and distort the surface topography. To avoid sample damage, the non-contact mode is required to oscillate the tip above the sample surface without contact. However, the long-range attractive forces decrease the amplitude of oscillation, thus lowering the resolution. To maintain the resolution, the tip needs to contact sample surface intermittently, that is the tapping mode. By minimizing the lateral friction forces, the tapping mode also prevents damage to the sample surface. For non-contact mode and tapping mode, the cantilever oscillation amplitude is controlled to be constant. In this thesis, tapping mode is used to measure the thickness of 2D flakes.

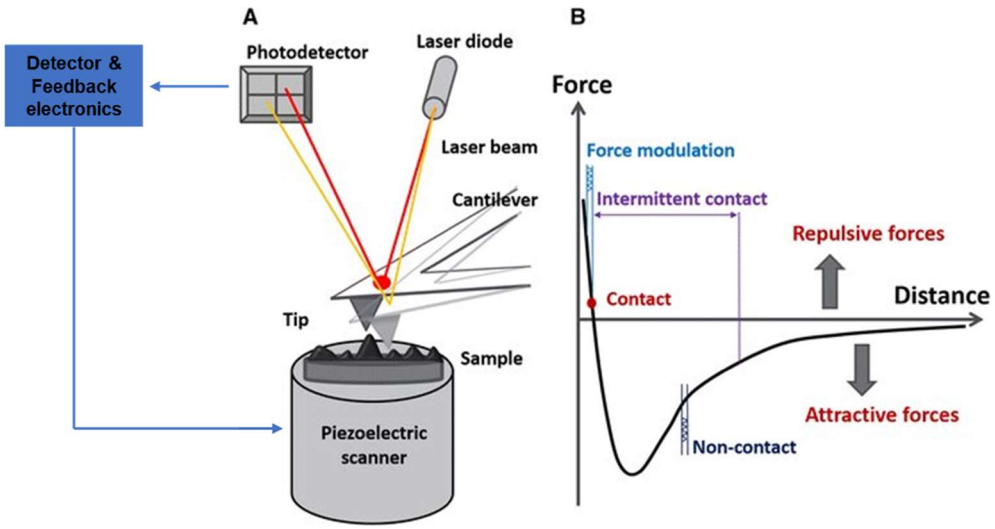

Figure 3.8. The principles of AFM. (a) Schematic configuration of AFM. (b) The probed forces at different distances between the tip and the sample surface in various imaging modes. Reproduced from Ref. [92].

3.2.2 Optical Microscopy

When light hits a surface, photons can be absorbed, transmitted, reflected, or scattered, as shown in **Figure 3.9a**. Optical microscopy produces optical contrast images based on reflectance difference of light on a substrate with and without 2D TMDs (**Figure 3.9b**).[93] The optical contrast difference (C_D) is defined as the relative intensity of light reflected by 2D TMDs (R) and substrate (R_S)[94]:

$$C_D = R - R_S \tag{3.1}$$

A positive C_D corresponds to brighter 2D TMDs on the substrate than bare substrate ($R > R_S$); A negative C_D corresponds to darker 2D TMDs on the substrate ($R < R_S$).

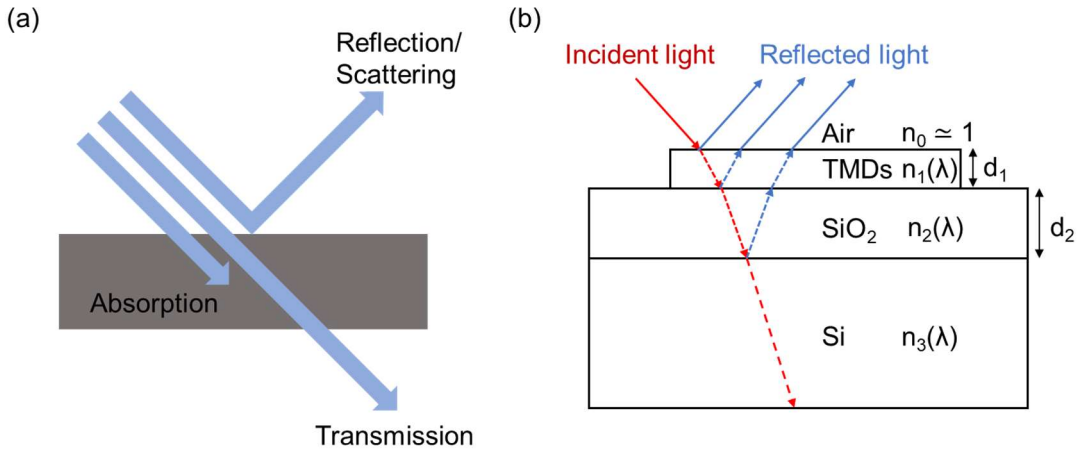

Figure 3.9. (a) Schematic of different pathways of light when interacting with a material, including absorption, transmission, reflection, and scattering. (b) Schematic of various reflection paths in TMDs/SiO_2/Si layers.[93] *The refractive index for air is represented as $n_0 \simeq 1$, while the wavelength-dependent refractive indices for the other layers is represented as $n_1(\lambda)$ for TMDs, $n_2(\lambda)$ for SiO_2, and $n_3(\lambda)$ for Si. Reproduced from Ref. [93].*

The optical contrast difference can be modulated by wavelength-dependent refractive index of substrate (n).[95,96] Zhang's group has shown that under white light illumination, MoS_2 nanosheets with layer numbers (L) ranging from 1 to 5 can be clearly identified on 300 nm SiO_2/Si **Figure 3.10a–e**).[97] When measuring the optical contrast difference for 1L – 15L MoS_2, 1L – 7L MoS_2 (appear darker than SiO_2/Si) show negative optical contrast difference while 8L – 15L MoS_2 (appear brighter than SiO_2/Si) show positive optical contrast difference (**Figure 3.10f**). In comparison, MoS_2 on 90 nm SiO_2/Si shows negative contrast difference in 1L – 5L and positive contrast difference in 6L – 15L (**Figure 3.10g**). Compared to 90 nm SiO_2/Si, 300 nm SiO_2/Si are more suitable to rapidly differentiate 1L – 3L MoS_2 because of the sufficient gap between the contrast difference values of adjacent layer numbers. Therefore, 300 nm SiO_2/Si is primarily used as substrate for 2D TMDs in this thesis.

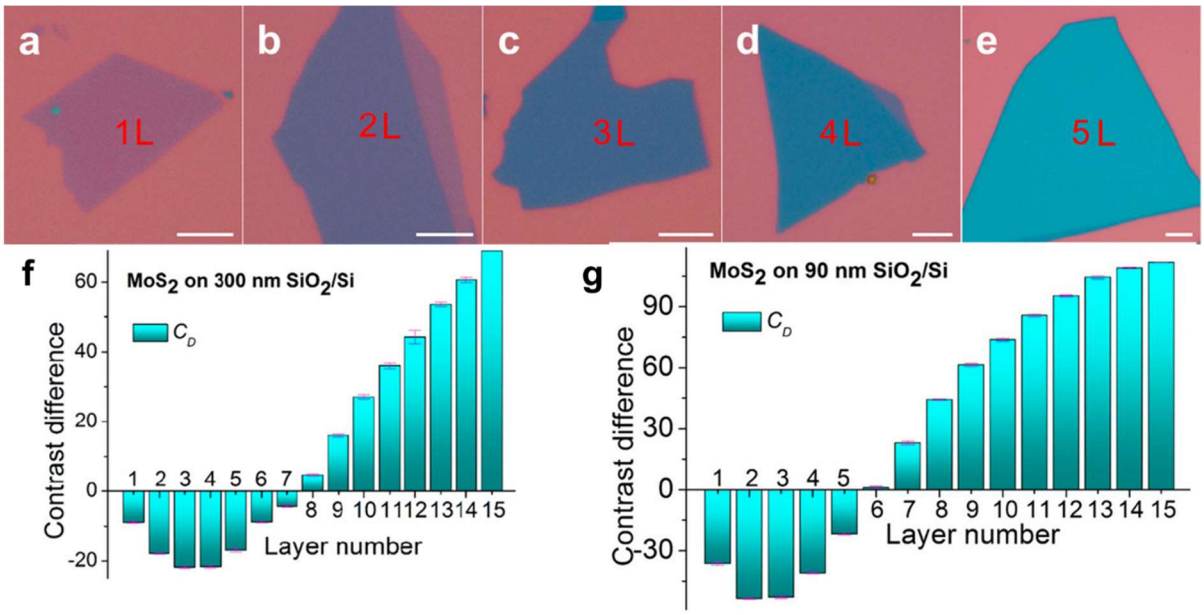

Figure 3.10. Optical microscopy characterization of MoS_2 with different layer numbers (L) on SiO_2/Si. (a–e) Optical microscopy images of 1L – 15L MoS_2 on 300 nm SiO_2/Si. The scale bars are 5 μm. MoS_2 flakes with different layer numbers show different optical contrast. (f–g) Plots of optical contrast difference (C_D) of 1L – 15L MoS_2 on (f) 300 nm SiO_2/Si, and (g) 90 nm SiO_2/Si. Reproduced from Ref. [97].

Both mechanically exfoliated and CVD-grown MoS_2 synthesized in this thesis were characterized by optical microscopy. As shown in **Figure 3.11**, darker monolayer MoS_2 can be easily distinguished from brighter thicker layers. In this study, only flakes free of measurable bubbles, wrinkles, or cracks were chosen for both mechanically exfoliated and CVD-grown MoS_2. The lateral size of monolayers was typically from 10 – 50 μm, which is suitable for Raman and PL spectroscopies (1 – 3 μm spot size), as well as XPS spectroscopy (15 × 35 μm spot size) which requires flakes of ≥20 μm.

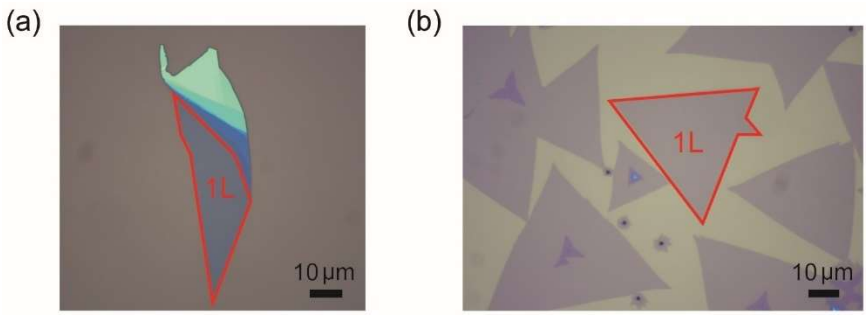

Figure 3.11. Optical microscopy images of synthesized MoS_2 flakes without noticeable bubbles, wrinkles, or cracks. (a) Optical microscopy image of mechanically exfoliated MoS_2. (b) Optical microscopy image of CVD-grown MoS_2. Monolayers are marked in red.

3.2.3 Absorption Spectroscopy

As discussed in **Section 1.3**, photoluminescence in 2D TMDs requires absorption of photons with energy larger than the bandgap of 2D TMDs. Absorption spectroscopy measures the number of photons absorbed by a material at each wavelength. This allows probing of the electronic structure – in particular, the conduction band. In 2D TMDs, the exciton resonance energies can be obtained from absorption measurements. From the optical paths in 2D TMDs shown in **Figure 3.12a**, absorbance ($\%A$) requires the measurement of both transmittance ($\%T$) and reflectance ($\%R$) where $A = 1 - \%R - \%T$. The transmittance measures the intensity difference between incident light and light transmitted through the sample. The reflectance measures the intensity difference between light reflected from the sample and light reflected from substrate only (as reference), also referred to as differential reflectance. In practice, reflectance is more often measured and taken as indicator of absorption since transparent substrates (*e.g.*, ultrathin optical glass slides for thin films and cuvette for solution) are required for transmittance measurement but not for reflectance measurement. In this thesis, 2D TMDs were exfoliated or grown on opaque SiO_2 (300nm)/Si substrates to easily identify monolayers. Therefore, reflectance was measured to characterize the optical properties of 2D TMDs in **Chapter 4**.

A typical example of absorption of monolayer TMDs in terms of differential reflectance ($\Delta R/R$) versus wavelength from Eda's group is shown in **Figure 3.12a**.[98] The grey curves represent the differential reflectance of different 2D TMDs. All monolayer TMDs show resonance peaks from excitonic transitions of A-exciton, B-exciton and also the C exciton at higher energies

(the spectrum of WSe_2 contains additional peaks labelled at A′ and B′). Surprisingly, it can be seen from the spectra that the absorption of the monolayers can be on the order of 30% or higher at the C-exciton energies. The A and B exciton transitions are explained in **Figure 1.6c**. The broad and enhanced absorption at the C exciton originates from band nesting between the Γ and K point in the band structure, as shown in **Figure 3.12b**.

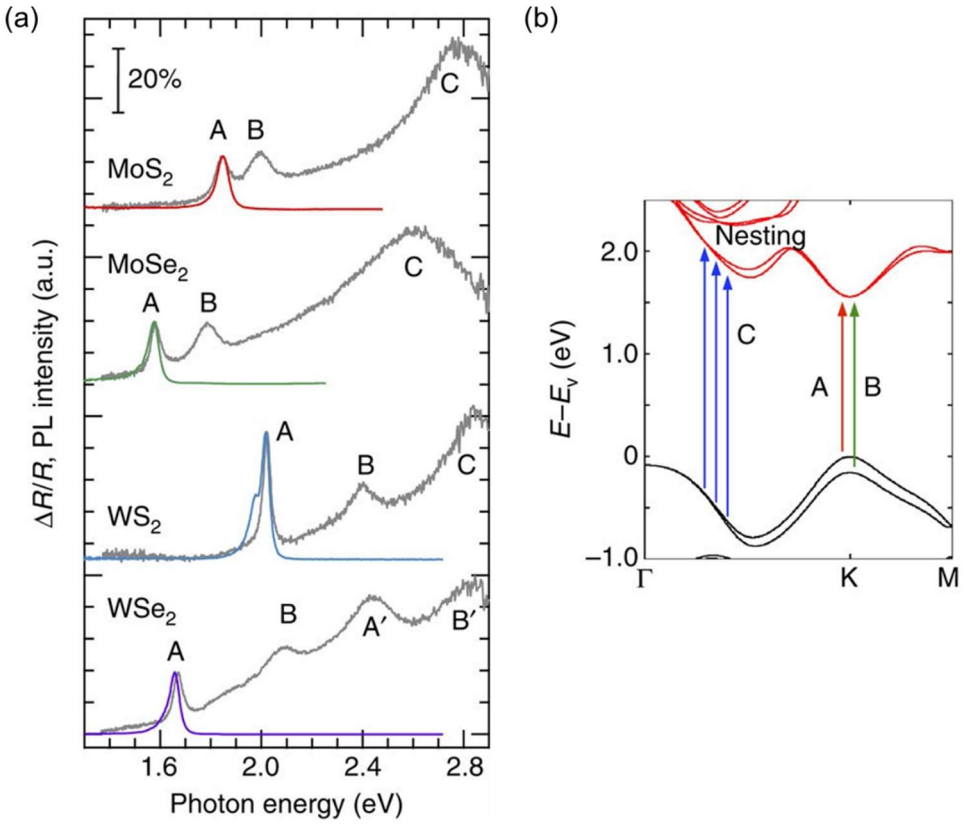

Figure 3.12. (a) Differential reflectance spectra (ΔR/R) shown in grey and PL spectra (shown in red, green, blue, and purple) of monolayer TMDs on quartz substrates. The vertical axis is for ΔR/R with a scale bar representing 20% absorption. The PL spectra are normalized to A exciton resonance differential reflectance peak. (b) The calculated band structure of monolayer MoS_2, showing transitions of A exciton and B exciton at K point of 2D MoS_2 Brillouin zone, and band nesting (C) between the Γ and K point. Reproduced from Ref. [98].

The measured reflectance spectra are affected by temperature. As shown in **Figure 3.13a**, with decreasing temperature, the A-exciton resonance shows gradual blue shift due to bandgap increase that can be fitted by Varshni's formula[99]:

$$E_g = E_0 - \alpha T^2/(T + \beta) \quad (3.2)$$

where E_g is the bandgap of material at temperature (T), E_0 is the bandgap of material at 0 K, α and β have unit of meV/K and K, respectively. The line width of A-exciton resonance decreases from 40 meV to 6.1 meV, indicating that A-exciton resonance is dominated by exciton-phonon scattering at high temperatures but suppressed at low temperatures (⩽77 K), as shown in **Figure 3.13b**. While I have not measured low-temperature absorption/reflection of 2D MoS_2, the increase of bandgap with decreasing temperature provides insight into changes in PL. This helps to understand the low-temperature PL results presented in **Chapter 4**.

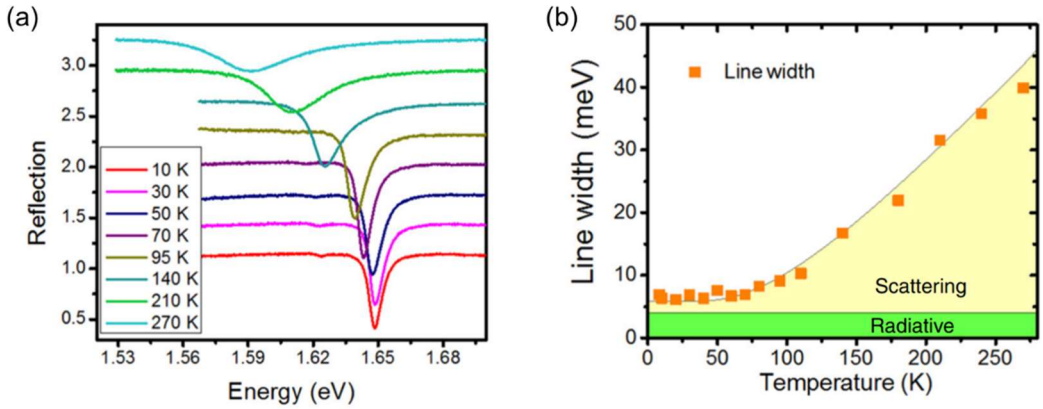

Figure 3.13. (a) Temperature-dependent reflection spectra of A-exciton resonance in $MoSe_2$ monolayer. The spectra are offset along the vertical axis for clarity. (b) Plot of line widths of A-exciton resonance as a function of temperatures, showing contributions from radiative recombination (green) and scattering (yellow). Reproduced from Ref. [99].

As discussed in **Section 2.2**, defects can alter the electronic band structure by introducing new energy levels in the bandgap (also temperature dependent), therefore the presence of defects can in principle be identified with resonance features in the absorbance spectrum. However, as shown in **Chapter 4**, the absorption in defective MoS_2 samples is broad and featureless and signature of sulfur vacancy states is not readily obvious.

3.2.4 Photoluminescence (PL) Spectroscopy

As discussed in **Section 1.3**, PL originates from radiative recombination of excitons. PL spectroscopy measures the number of photons emitted from a material as a function of photon

energy and can provide information about the electronic structure of materials. **Figure 3.12a** shows typical RT PL spectra of monolayer TMDs, in which dominant PL from A-exciton transition is observed at energies very close to the A-exciton resonance peak in the differential reflectance spectra. In this thesis, steady-state PL spectroscopy with laser excitation wavelength of 532 nm was used to characterize mechanical exfoliated and CVD grown monolayer MoS_2. The schematic setup of typical micro-PL measurements is shown in **Figure 3.14**.[100] Typical probing area is determined by the excitation laser spot size. Most micro-PL measurements use monochromatic laser at a fixed wavelength (with photon energy larger than the bandgap of semiconductor). In other instances, it is possible to measure PL at different excitation energies (PLE). 532 nm excitation wavelength was chosen based on the PLE results from Eda's group discussed in **Section 3.2.4.1**.

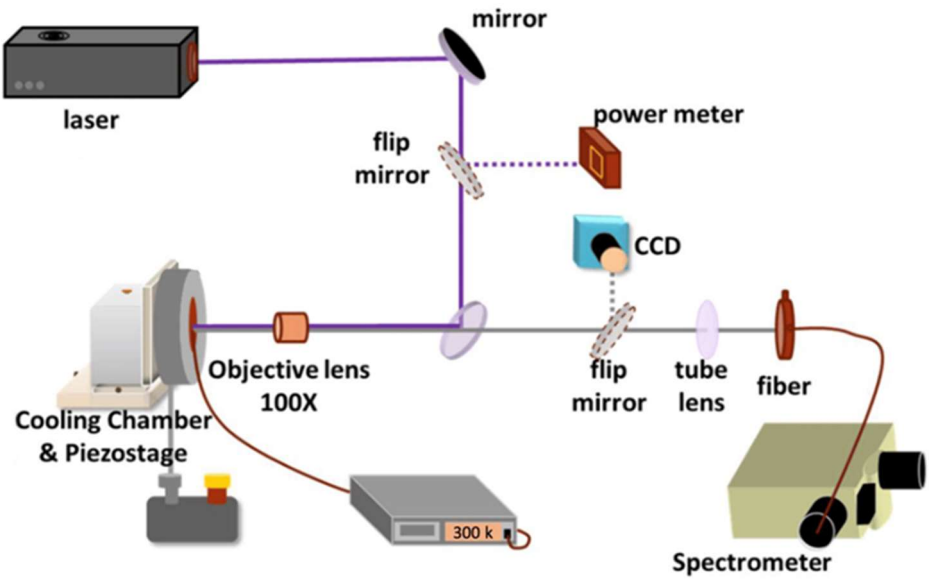

Figure 3.14. Schematic setup of micro-PL measurements. Reproduced from Ref. [100].

PL spectroscopy was used to characterize mechanically exfoliated monolayer MoS_2, as shown in **Section 3.1**, as well as CVD-grown monolayer MoS_2 (measured on its growth substrates). With respect to exfoliated 2D MoS_2, the A^-/A peak of CVD-grown MoS_2 is red-shifted by ~65 meV while B exciton peak shows a similar shift of ~67 meV (**Figure 3.15b**). This indicates that the bandgap of monolayer MoS_2 is narrowed due to the built-in biaxial tensile strain. This results from cooling of the CVD-grown sample from the growth temperature of 700 °C to room

temperature which leads to thermal expansion coefficient (TEC) mismatch between MoS_2 (TEC = 10^{-6} K^{-1}) and SiO_2/Si substrate (TEC = 5.5×10^{-7} K^{-1}). The reported shift of A exciton under biaxial tensile strain is −99 ± 6 meV per % strain.[101] Extrapolating this shift to the PL shift in the CVDgrown MoS_2, the biaxial tensile strain is approximated to be −0.68%.

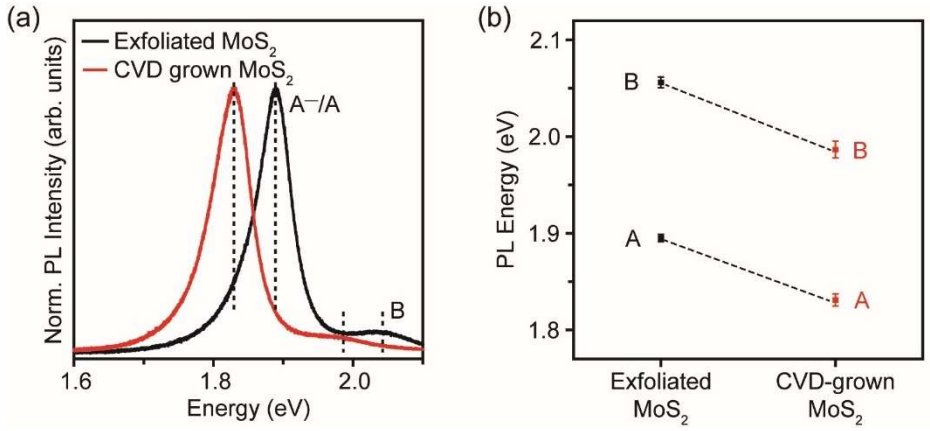

Figure 3.15. RT PL spectra of monolayer MoS_2 synthesized by mechanical exfoliation and CVD growth. (a) PL spectra of mechanically exfoliated and CVD-grown monolayer MoS_2. Each spectrum is normalized to the intensity of A^- trion/A exciton (A^-/A) peak. With respect to exfoliated MoS_2, CVD-grown MoS_2 shows a red-shift in A^-/A and B exciton peaks. (b) Plot of PL energy of A exciton and B exciton in mechanically exfoliated and CVD-grown monolayer MoS_2.

3.2.4.1 Photoluminescence excitation (PLE) spectroscopy

Eda's group measured the PLE map of mechanically exfoliated monolayer MoS_2 on quartz substrates, that is, the emission photon energy versus the excitation photon energy (**Figure 3.16a**).[98] It can be seen that for excitation energy ranging from 2.0 – 2.5 eV, the A exciton emission is bright and located at the same emission energy (~1.86 eV). The intensity of A exciton emission is highest at excitation energy of ~2.05 eV. In **Figure 3.16b**, the PLE, relative quantum yield (QY), and differential reflectance (ΔR/R) are plotted as a function of excitation energy. For excitation energy of <~2.4 eV, the relative QY remains high. The maximum relative QY occurs when the excitation energy is in resonance with the B exciton absorption (shown in grey curve). Based on this, I used excitation energy of ~2.33 eV (wavelength of 532 nm) for my micro-PL measurements.

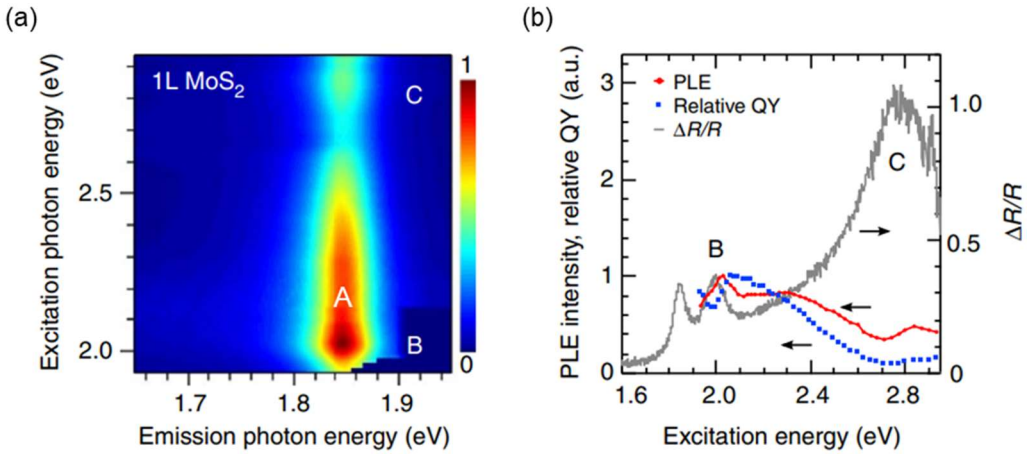

Figure 3.16. (a) PLE intensity color map for mechanically exfoliated monolayer MoS_2 on quartz substrates. The color bar represents the PLE intensity. (b) Plots of PLE intensity and relative QY for A exciton emission as a function of excitation energy for monolayer MoS_2. Differential reflectance spectrum is shown for comparison. Reproduced from Ref. [98].

3.2.4.2 Temperature-Dependent, Power-Dependent, and Time-Resolved PL Spectroscopy

Steady-state PL spectroscopy can be used to reveal the presence of defects. As discussed in **Section 2.2**, in-gap electronic states generated by defects can trap excitons and induce defect-mediated emission at lower energies than free exciton emission. Temperature-dependent, power-dependent and time-resolved measurements can help distinguish defect-mediated emission from free exciton emission.

Temperature-dependent PL spectroscopy measures PL spectrum at various temperatures. At room temperature, trapped excitons are mostly delocalized before any defect-mediated radiative or non-radiative recombination can occur, resulting in weak or absence of defect-mediated emission. At low temperatures (≤77 K), excitons are localized at trap states due to the lack of thermal energy for detrapping. Therefore, the evolution of low-energy emission measured at different temperatures can reveal the presence of in-gap states from defects. This temperature dependence of defect-mediated emission can be written by a thermal Arrhenius formula[102,103]:

$$I(T) = \frac{I(0)}{1+(\tau/\tau_0)e^{-E_A/KT}} \quad (3.3)$$

where $I(0)$ is the PL intensity at $T = 0$ K, τ is the excitonic lifetime, τ_0 is effective scattering time, K is the Boltzmann constant, and E_A is the activation energy that is required for delocalization of trapped excitons. Tongay *et al.* has reported temperature-dependent and power-dependent PL properties of defective monolayer MoS_2 with sulfur vacancies created by annealing at 500 °C in vacuum (**Figure 3.17**).[104] As shown in **Figure 3.17a**, defective monolayer MoS_2 only shows free exciton emission (X_0) at 300 K. The bound exciton emission (X_B) that is mediated by defects emerges at 175 K and its intensity approaches that of X_0 emission at 77 K. Both X_0 and X_B emissions show blue shift with decreasing temperatures – consistent with the blue shift of resonance reflectance features shown in **Figure 3.13**.

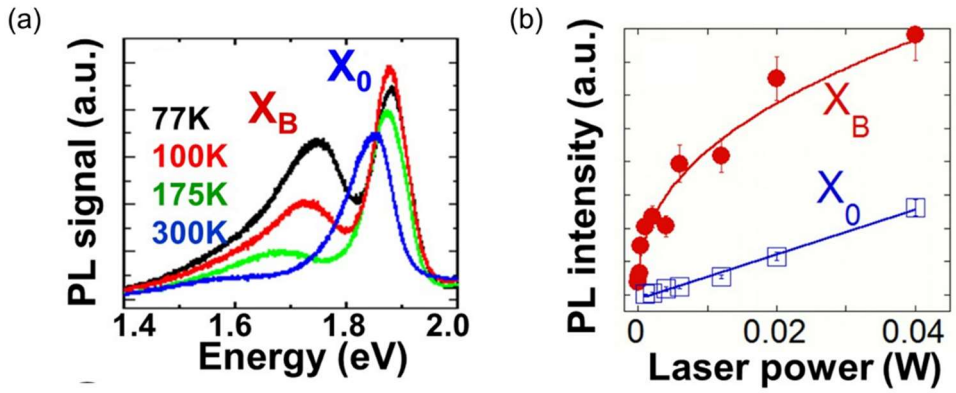

Figure 3.17. Temperature-dependent and power-dependent PL properties of monolayer MoS_2 with sulfur vacancies created by annealing at 500 °C in vacuum (~10^{-4} Torr). (a) Temperature-dependent PL spectra of defective MoS_2 at temperatures ranging from 300 to 77 K, showing the evolution of free exciton emission (X_0) and bound exciton emission (X_B) mediated by defects. (b) Power-dependent PL intensity plot of X_0 and X_B emissions. X_0 emission is linearly dependent on laser power whereas X_B shows saturation dependence. Reproduced from Ref. [104].

Power-dependent PL spectroscopy measures the PL as a function of excitation laser power. The empty in-gap defect states can be occupied by photoexcited carriers at sufficiently high excitation power.[104] In **Figure 3.17b**, the intensities of free exciton emission (X_0) and bound exciton emission (X_B) are plotted as a function of excitation power.[104] The X_0 emission scales

linearly with increasing excitation power whereas the X_B emission appears to saturate. The PL intensity (I_{PL}) follows a power-law dependence with excitation laser power (L_E) so that $I_{PL} \propto L_E^k$, where k is power exponent.[105] The k value can be identified from the logarithmic plot of **Figure 3.17b**. Excitonic transitions typically show k = ~1, while transitions from localized excitons at lattice defects show $k < 1$.[104,106] While the logarithmic plot is not shown here, the power-dependent PL intensity plot and its logarithmic plot for investigating optical properties of defects are included in **Chapter 4**.

Time-resolved PL spectroscopy measures PL decay after an excitation laser pulse (<picosecond) to determine the PL lifetime. This is typically achieved by time-correlated single photon counting (TCSPC) that detects a single photon and compares its arrival time with respect to the laser pulse. Repeating the laser pulse multiple times can allow enough photon events to accumulate and generate a statistical histogram plot of photon arrival times. Fitting the histogram plot exponentially, the PL lifetime can be obtained. The PL consists of several processes: 1) excitation of photoexcited carriers (~femtosecond), 2) relaxation (~100 femtoseconds) and thermalization (~1 picosecond), 3) radiative recombination (hundreds of picoseconds to tens of nanoseconds), and 4) non-radiative recombination. Eda's group has measured PL decay of defective monolayer WS_2, in which sulfur vacancies were created by proton irradiation (**Figure 3.18a**).[107] The free neutral exciton emission (X^0) and trion emission (T) show lifetime of hundreds of picoseconds, while localized exciton emissions LX_1 and LX_2 show longer lifetime of tens of nanoseconds (ns). The long-lived localized exciton emissions are also observed in other defective monolayer TMDs, including $MoSe_2$, WSe_2, and MoS_2, as shown in **Figure 3.18b**.

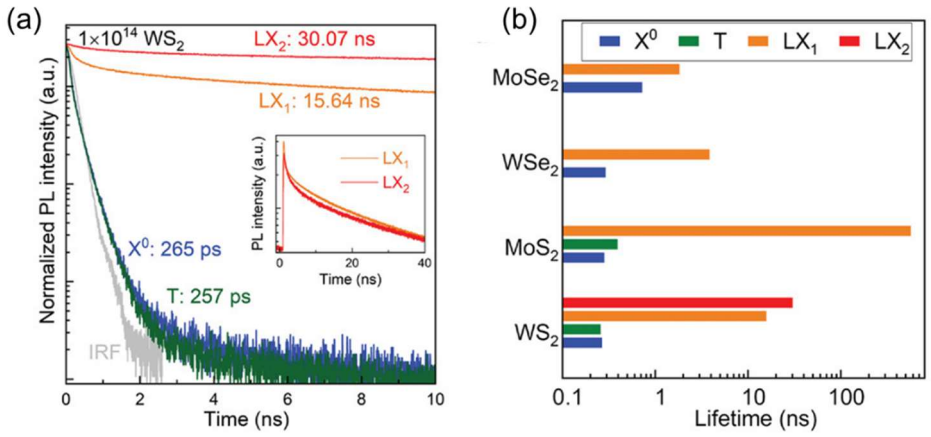

Figure 3.18. Time-resolved PL decay of monolayer TMDs with sulfur vacancies created by irradiation with protons. (a) Time-resolved PL decay plot of free neutral exciton emission (X^0), trion emission (T), and localized exciton emissions (LX_1 and LX_2) for defective monolayer WS_2. (b) Summary of lifetimes of different PL emissions for defective monolayer $MoSe_2$, WSe_2, MoS_2, and WS_2. Reproduced from Ref. [107].

3.2.3 Raman Spectroscopy

Raman spectroscopy is based on scattering of photons to reveal the local structure of materials. As shown in **Figure 3.19**, electrons can be excited from the ground state to some virtual energy state and immediately relax back to the ground state.[108] Scattering occurs either elastically or inelastically. In elastic scattering (Rayleigh scattering), electrons are excited by the Raman laser to a virtual state and relax back to the original state, showing no changes in photon energy. In inelastic scattering (Raman scattering), the photons are scattered with energies different from the incident photons. One is Stokes scattering where excited electrons from the ground state relax to a virtual state and emit photons with energy lower than the excitation laser energy. The other is anti-Stokes scattering where excited electrons relax back to a virtual state and release photons with energy greater than the excitation photons. In most Raman measurements, Stokes scattering is used since the ground vibrational state is more populated than higher vibrational states that leads to more intense Stokes signals. It is worth noting that Raman scattering is an inefficient process with only 1 in 10^6 – 10^8 photons emitted. By measuring the energy difference between incident photons and emitted photons, the energy of vibrations of molecules can be determined. In Raman spectra, this energy difference is usually presented in wavenumbers ($\tilde{\nu}$), calculated from the wavelength difference (λ):

$$\Delta\tilde{\nu} = \frac{1}{\lambda_0} - \frac{1}{\lambda_1} \tag{3.4}$$

where $\Delta\tilde{\nu}$ is the wavenumber difference between incident and emitted photons, while λ_0 and λ_1 are the wavelengths of incident and emitted photons, respectively.

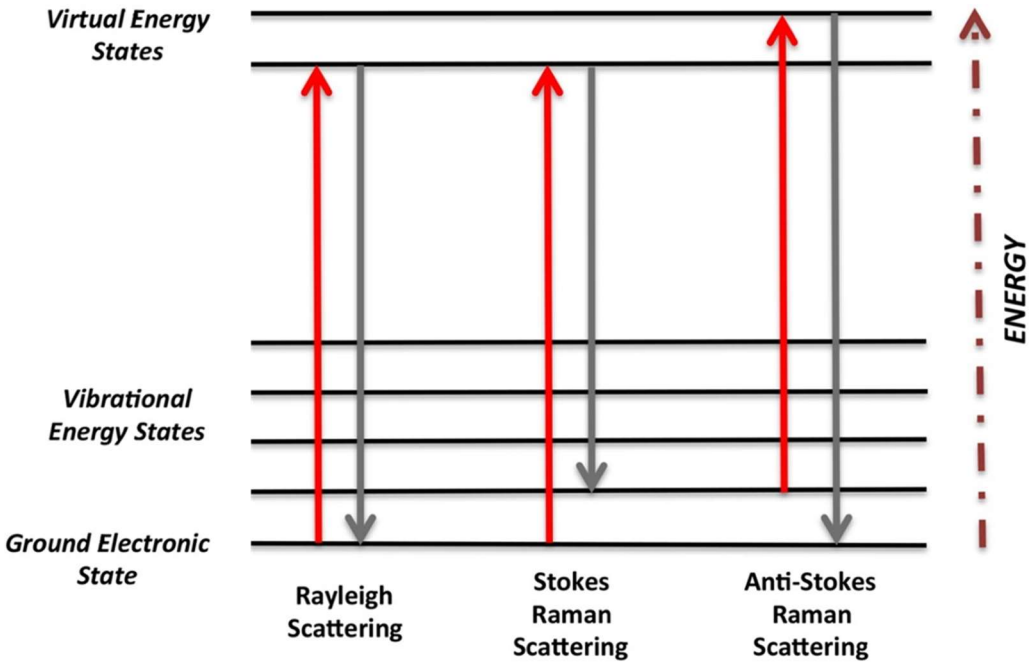

Figure 3.19. Schematic energy level diagram of the transitions of Rayleigh, Stokes, and anti-Stokes Raman scattering. Reproduced from Ref. [108].

However, not all materials are Raman active. Raman scattering arises from changes in polarizability (α) of a molecule. That is, the possibility of molecules to induce electric dipole moments (μ_i) in an external electric field, calculated by:

$$\alpha = \alpha_0 + \alpha_1 \sin(2\pi\nu_{vib}t) \tag{3.5}$$

where α_0 is equilibrium polarizability, α_1 is rate of change of polarizability with molecule vibration, ν_{vib} is vibration frequency of the molecule, and t is time period. The electric field generated by the photon with a frequency (ν_p) can be calculated by:

$$E = E_0 \sin(2\pi\nu_p t) \tag{3.6}$$

where E is the amplitude of the electric field at time, E_0 is the maximum amplitude of the electric field. Therefore, the induced dipole moment can be calculated by:

$$\mu_{\mathrm{i}} = \alpha E = [\alpha_0 + \alpha_1 \sin(2\pi\nu_{\mathrm{vib}}t)] \times E_0 \sin(2\pi\nu_{\mathrm{p}}t) \quad (3.7)$$

The induced dipole moment can be further written as:

$$\mu_{\mathrm{i}} = \alpha_0 E_0 \sin(2\pi\nu_{\mathrm{p}}t) + \frac{\alpha_1 E_0}{2}\cos\big(2\pi(\nu_{\mathrm{p}} - \nu_{\mathrm{vib}})t\big) - \frac{\alpha_1 E_0}{2}\cos(2\pi(\nu_{\mathrm{p}} + \nu_{\mathrm{vib}})t) \quad (3.8)$$

where the first term represents a dipole moment oscillating at photon frequency ν_{p} without energy gain or loss (Rayleigh scattering). The second term represents a dipole moment losing energy of $h\nu_{\mathrm{vib}}$ and oscillating at frequency of $\nu_{\mathrm{p}} - \nu_{\mathrm{vib}}$ (Stokes scattering). The third term represents a dipole moment gaining energy of $h\nu_{\mathrm{vib}}$ and oscillating at frequency of $\nu_{\mathrm{p}} + \nu_{\mathrm{vib}}$ (anti-Stokes scattering). The vibration of a molecule depends on mass of atoms and bond strength, described by Hooke's law:

$$\nu_{\mathrm{vib}} = \frac{1}{2\pi c}\sqrt{\frac{K}{m_{\mathrm{r}}}} \quad (3.9)$$

where c is the velocity of light, K is force constant of bond between atoms A and B, and m_r is reduced mass of A and B. It can be seen that lighter atoms and stronger bonds give rise to higher vibration frequencies.

Lee *et al.* has shown that for 2H MoS_2, there are four Raman active modes, three in-plane modes E^2_{2g}, E^1_g, E^1_{2g}, and one out-of-plane mode A_{1g}, as shown in **Figure 3.20a**.[109] Typical Raman spectrum of monolayer MoS_2 only shows E^1_{2g} mode at ~384 cm^{-1} and A_{1g} mode at ~403 cm^{-1} (**Figure 3.20b**). When the layer numbers increase, E^1_{2g} mode softens to lower frequencies while A_{1g} mode stiffens to higher frequencies. **Figure 3.20c** shows a plot of frequencies of E^1_{2g} and A_{1g} modes (shown in black), and their frequency difference (shown in red) as a function of layer thickness. Monolayer MoS_2 shows the smallest frequency difference (~18 – 20 cm^{-1}) between E^1_{2g} and A_{1g} modes, hence this frequency difference can be taken as an indicator of monolayer MoS_2.

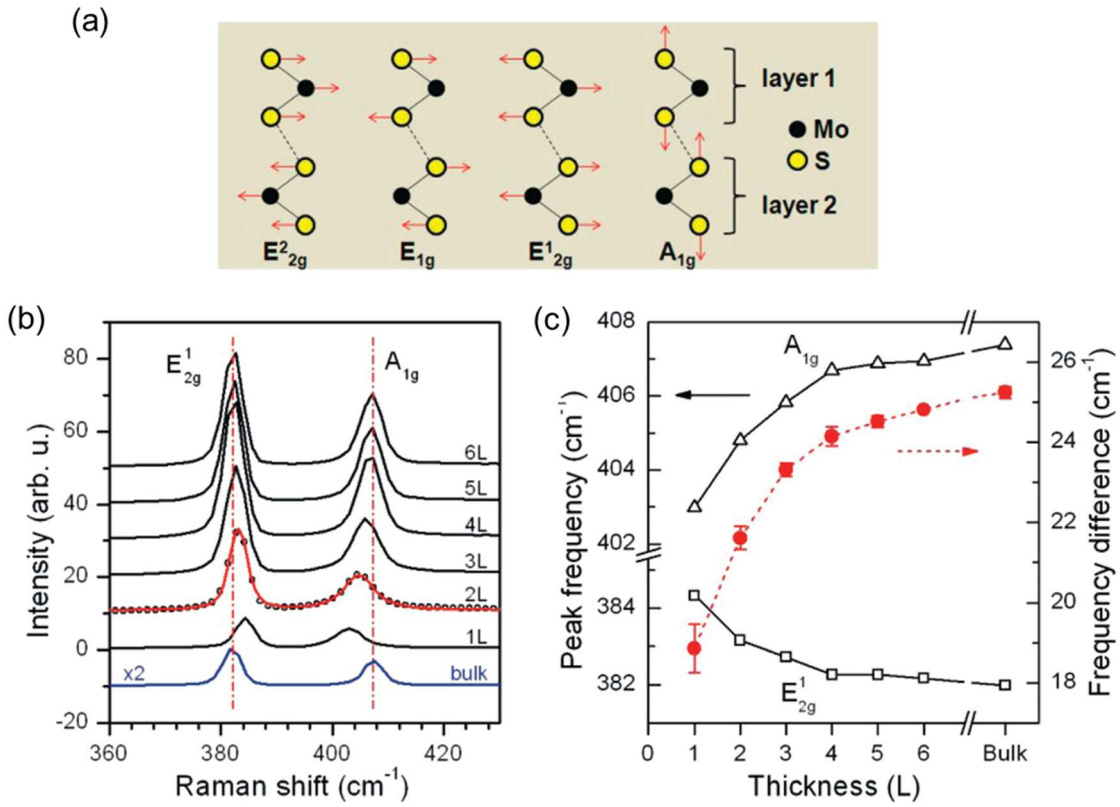

Figure 3.20. (a) Schematic of four Raman-active modes in MoS_2. (b) Raman spectra of MoS_2 ranging from bulk to monolayer, showing in-plane mode E^1_{2g} and out-of-plane mode A_{1g}. The dotted red vertical line denotes the E^1_{2g} and A_{1g} mode in bulk MoS_2. (b) Plot of frequencies of E^1_{2g} and A_{1g} Raman modes (left vertical axis) and their difference (right vertical axis) as a function of layer thickness. Reproduced from Ref. [109].

For materials that contain Raman active molecular vibrations, perturbation on crystal lattice induced by defects can be identified by Raman scattering. In defect-free crystals, only phonons near the center of the Brillouin zone (**Γ**) where $\mathbf{q} \cong 0$ (**q** is the wavevector of phonon) are Raman active due to the fundamental Raman selection rule.[110] For defective crystals such as the MoS_2 samples studied here, the presence of defects leads to observation of three typical Raman changes: (1) Symmetric broadening of Raman peaks that can be attributed to reduction of phonon lifetime that is inversely proportional to linewidth of Raman peaks[111]; (2) Changes in intensity of Raman peaks that can be explained by changes in chemical bonds. For defective crystal lattices, local chemical bonds could be broken, weakening prominent peaks at the Brillouin zone center. New non-center phonon modes may also be activated by defects due to the relaxation of the wave-vector selection rule. Using Raman spectroscopy, the defect density

can be estimated using either the peak intensity ratio or peak area ratio of defect-activated peaks and prominent peaks at the Brillouin zone center. (3) Changes in the frequency of Raman peaks due to the diminished periodicity. The relaxation of the wave-vector selection rule results in random wave vectors at $\mathbf{q} \ncong 0$ for non-center phonon modes. This randomness can not only cause changes in the line shape and intensity, but also shift the frequency of the phonon mode (Raman peak position). Mignuzzi *et al.* has shown the evolution of Raman features in monolayer MoS_2 under the bombardment of a focused Mn^+ ion beam that creates defects (**Figure 3.21**).[112] The in-plane mode E^1_{2g} is red-shifted while the out-of-plane mode A_{1g} is blue-shifted, with significant broadening of both peaks. Additional new peaks are activated by defects, *e.g.*, LA(M) peak at ~227 cm^{-1}. However, the nature of the generated defects was not further characterized.

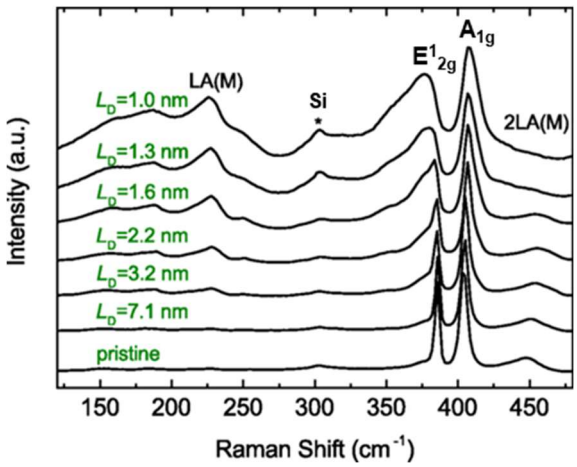

Figure 3.21. RT Raman spectra of monolayer MoS_2 with defects created by Mn^+ ion beam bombardment. The density of defects increases with shortening inter-defect distances L_D. The spectra are normalized to the intensity of A_{1g} peak. Reproduced from Ref. [112].

3.2.4 X-ray Photoelectron Spectroscopy (XPS)

XPS is a surface-sensitive technique, based on the photoelectric effect. When a beam of X-ray photons hits a surface, the atoms undergo photoionization. By absorbing the energy of photons, photoelectrons are ejected from different orbitals into vacuum with a defined kinetic energy. By measuring the kinetic energy (KE) of the ejected photoelectrons, the binding energy (BE) of electrons in a specific orbital can be determined by:

$$BE = h\nu - KE \tag{3.10}$$

where $h\nu$ is the energy of absorbed photons, h is Planck's constant, and ν is the frequency of absorbed photons. For solid materials including 2D TMDs, there is an additional potential barrier at the surface for photoelectrons to overcome, which corresponds to the work function (Φ) that is the energy difference between the sample Fermi level and the vacuum level, as shown in the left panel of **Figure 3.22**.[113] Therefore, the photoelectron kinetic energy is measured with respect to the sample Fermi level, giving rise to a new equation:

$$BE = h\nu - (KE_{\mathrm{F}} + \Phi_{\mathrm{sample}}) \tag{3.11}$$

where Φ_{sample} is the work function of the sample, and KE_{F} is the kinetic energy of the photoelectrons with respect to the sample Fermi level.

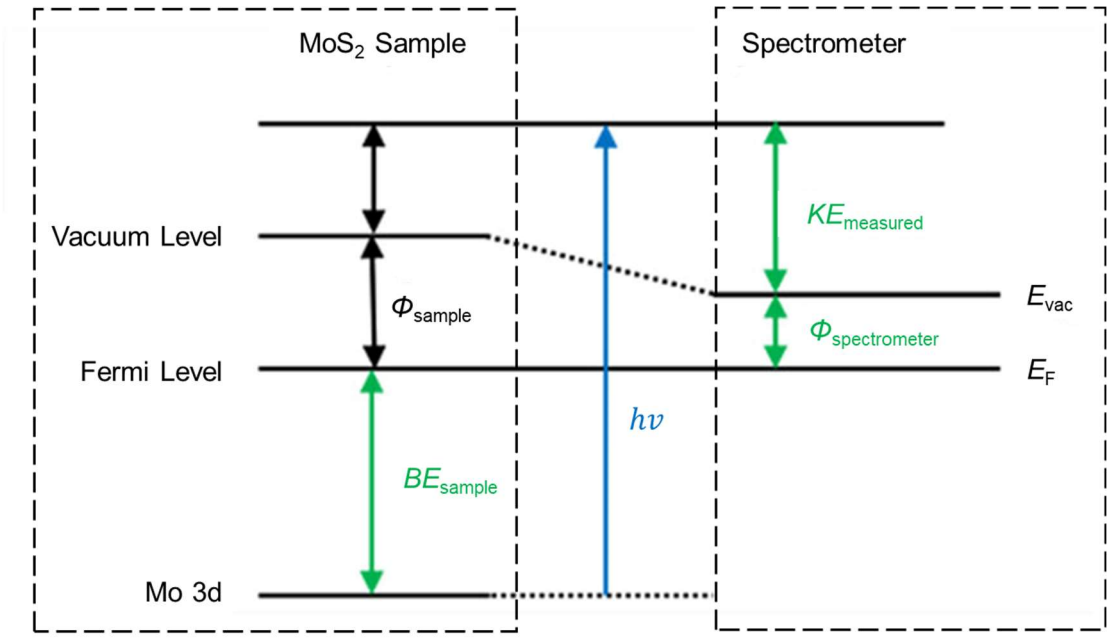

Figure 3.22. Schematic energy level diagram for MoS_2 in good electrical contact with the spectrometer. Reproduced from Ref. [113].

To get reliable measurements, samples need to be in good electrical contact with the spectrometer, as shown in the right panel of **Figure 3.22**.[113] Owing to charge transfer at the interface between sample and spectrometer, the Fermi level of the sample is aligned with that of the spectrometer. Since the kinetic energy of photoelectrons is measured on the side of the

spectrometer (KE_{measured}), we need to know the work function of the spectrometer ($\Phi_{\text{spectrometer}}$) to acquire the binding energy of the sample by:

$$BE = h\nu - (KE_{\text{measured}} + \Phi_{\text{spectrometer}}) \quad (3.12)$$

If the sample has bad electrical contact with the spectrometer, then their Fermi levels are misaligned, leading to inaccurate measurement of binding energy. Another factor that could shift the measured binding energy is charging which results from the accumulation of positive charges on the sample surface as a result of photoelectron emission. For conducting materials, internal electrons can diffuse from the bulk to the surface to compensate for the positive charges, whereas for semiconducting and insulating materials, the compensation is limited. Accumulated positive charges can attract photoelectrons, reducing the kinetic energy of photoelectrons and shifting the binding energy towards higher *BE*. Therefore, for semiconducting MoS_2, additional compensation methods are required to externally inject electrons, *e.g.*, grounded electrode, low-energy electron flood gun (10 eV or less).[114] In this thesis, In/Au contact was used to ground 2D MoS_2 to reduce charging.

For MoS_2, XPS has been extensively used to measure Mo 3d and S 2p to characterize the chemical states and bonding environment of the constituent elements in MoS_2. Our group has used XPS to characterize the ultraclean vdW interface formed between CVD-grown monolayer MoS_2 and indium/gold (In/Au) electrodes deposited by electron-beam evaporator.[115] As shown in **Figure 3.23**, Mo 3d spectrum shows Mo 3d doublet peaks and S 2s peak at lower binding energy while S 2p spectrum shows S 2p doublet peaks, attributed to pristine MoS_2. Nonstoichiometric Mo_xS_y peaks are expected to appear at higher binding energy in Mo 3d spectrum while lower binding energy in S 2p spectrum. The absence of Mo_xS_y peaks shows that MoS_2 remains pristine through In/Au deposition.

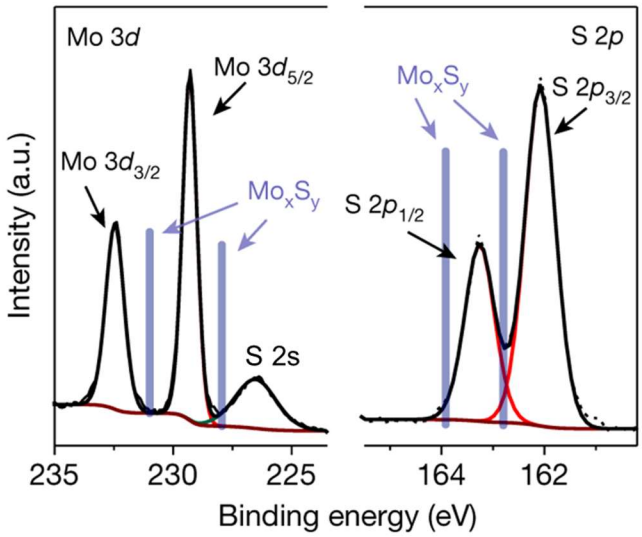

Figure 3.23. XPS spectra of Mo 3d and S 2p core levels of stoichiometric MoS_2. Reproduced from Ref. [115].

The formation of core level doublet peaks is due to spin-orbit coupling, that is, the coupling of magnetic fields generated by orbit motion and spin motion of electrons. In nonsymmetric orbitals (angular momentum quantum number $l > 0$), two possible magnetic fields exist due to two possible spin states (spin quantum number $m_s = \pm 1$) and are typically expressed by total angular momentum number $j = l + m_s$. For Mo 3d ($l = 2$), j is either 3/2 or 5/2. Mo $3d_{5/2}$ degenerate level has a larger j value and a lower binding energy than Mo $3d_{3/2}$. Similarly, S 2p core level degenerates into S $2p_{1/2}$ and S $2p_{3/2}$ doublet. The schematic photoelectron emission from Mo 3d and S 2p doublets are shown in **Figure 3.24**. Mo $3d_{3/2}$ and Mo $3d_{5/2}$ doublet are separated by 3.15 eV while S $2p_{1/2}$ and S $2p_{3/2}$ are separated by 1.18 eV. The relative number of photoelectrons is represented by the thickness of orange arrows. With a given number of incident X-ray photons, the number of photoelectrons emitted from Mo 3d doublet follows $N_{\text{Mo 3d3/2}}$: $N_{\text{Mo 3d5/2}} = (2j + 1)_{\text{Mo 3d3/2}}$: $(2j + 1)_{\text{Mo 3d5/2}} = 2$: 3. Similarly, $N_{\text{S 2p1/2}}$: $N_{\text{S 2p3/2}} = 1$: 2. The number of photoelectrons can be obtained from peak area in XPS spectrum.

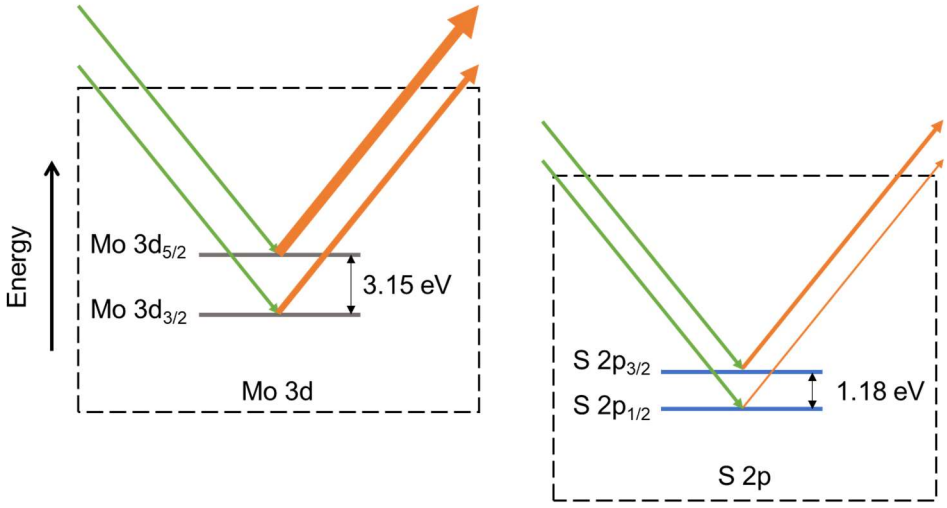

Figure 3.24. Schematic photoelectron emission from Mo 3d doublet and S 2p doublet in MoS_2. The green arrows represent incident X-rays. The orange arrows represent photoelectron emission from an orbital. The grey lines in the left panel and blue lines in the right panel represent the orbital energy levels.

The peak area ratio across Mo 3d and S 2p doublets can be used to calculate elemental stoichiometry of MoS_2:

$$\frac{\mathrm{S}\ (at.\%)}{\mathrm{Mo}\ (at.\%)} = \left(\frac{I_{\mathrm{S\ 2p\ 3/2}}}{\sigma_{\mathrm{S\ 2p\ 3/2}}}\right)/\left(\frac{I_{\mathrm{Mo\ 3d\ 5/2}}}{\sigma_{\mathrm{Mo\ 3d\ 5/2}}}\right) \tag{3.13}$$

where S $(at.\%)$ and Mo $(at.\%)$ are atomic percentages $(at.\%)$ of S and Mo, $I_{\mathrm{S\ 2p\ 3/2}}$ and $I_{\mathrm{Mo\ 3d\ 5/2}}$ are integrated intensities (area) of S $2p_{3/2}$ peak and Mo $3d_{5/2}$ peak. $\sigma_{\mathrm{S\ 2p\ 3/2}}$ and $\sigma_{\mathrm{Mo\ 3d\ 5/2}}$ are the photoionization cross-sections calculated theoretically. Here photoionization cross-sections are used to normalize the relative photoelectron peak intensities due to the relative probability of photoionization of electrons. The stoichiometry can be used to quantify sulfur vacancies in MoS_2, as shown in **Chapter 4**.

In this study, synchrotron XPS was used to measure the chemistry of single flake monolayer MoS_2 obtained by mechanical exfoliation. Synchrotron XPS is useful because it provides high flux of X-rays with a beam that can be focused down to ~20 μm. This helps to collect enough signals from the monolayer sample with lateral dimensions of ~20 – 30 μm. Synchrotron radiation is emitted when electrons are forced to move along a curved orbit. In this process, electrons are generated by a hot filament and then accelerated and injected into a storage ring. In the storage ring, electrons move at relativistic speed with kinetic energy on the order of GeV.

Using dipole magnets to apply vertical magnetic field, electrons can be accelerated in the direction perpendicular to their velocity and thus are forced to move along a curved orbit. Using a series of dipole magnets to periodically anchor the storage ring, electrons can be kept in a closed orbit loop. The power (P) of synchrotron radiation per electron can be calculated by:

$$P = \frac{e^2}{6\pi\varepsilon_0 c^7}\frac{1}{m_0^4}\frac{E^2}{R^2} \quad (3.14)$$

where e is the electron charge, ε_0 is vacuum permittivity, c is the velocity of light, , m_0 is the rest mass of an electron, E is the electron energy, R is the radius of accelerator orbit. It can be seen that smaller accelerator orbit will result in higher synchrotron radiation power and this allows us to tune the energy of synchrotron radiation. Compared to lab based XPS that typically uses Al-Kα source (1486.6 eV), synchrotron XPS can produce X-rays ranging from 100 to 3000 eV. Soft X-rays (≤1000 eV) allow us to collect surface information from monolayer MoS_2 by increasing photoionization cross-sections.

3.2.6 X-ray Diffraction (XRD)

An X-ray diffractometer consists of an X-ray source, incident optics, sample goniometer, receiving optics, and detector (**Figure 3.25a**).[116] The X-ray beams are irradiated on samples through the incident optics at various angles between the source and the sample surface, and get diffracted to the receiving optics and detector. Most diffracted beams cancel each other out through destructive interference, while only X-rays incident at a specific angle of Θ can get diffracted at an angle of 2Θ between the incident beam and the detector through constructive interference. The coupled incident angle Θ and diffraction angle 2Θ depend on the lattice spacing, following Bragg's Law (see **Figure 3.25b**), written as:

$$n\lambda = 2d\ sin\Theta \quad (3.15)$$

where n is an integer, λ is the wavelength of the incident X-ray beam, and d is the interplanar spacing of a crystalline structure. With a fixed X-ray wavelength λ, the diffraction peak at an angle of 2Θ becomes a unique signature of the crystalline structure. Crystalline materials have long-range periodicity and can produce a diffraction pattern with sharp peaks, whereas amorphous materials are either invisible or can only produce broad signals in XRD patterns.

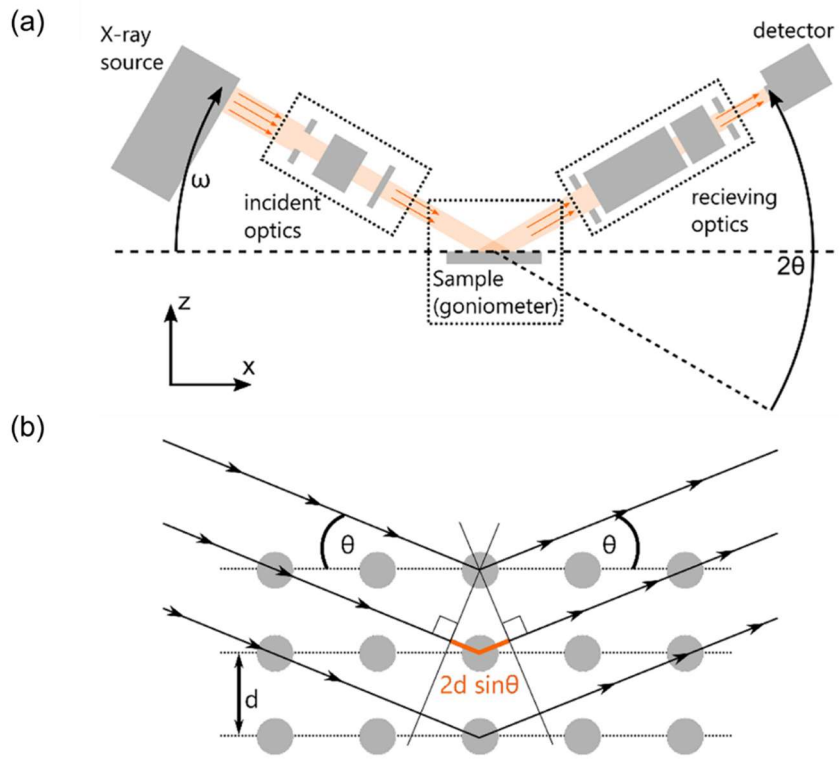

Figure 3.25. The principles of XRD. (a) Schematic configuration of XRD. (b) Schematic of Bragg's Law. Reproduced from Ref. [116].

However, XRD performed in Bragg–Brentano geometry is hindered from characterizing 2D TMD nanosheets, especially monolayers, due to the lack of periodicity in the third dimension (**Figure 3.26a**).[117] To measure nanosheets, the grazing incidence XRD (GIXRD) is required to maximize signals from the lateral periodicity by adjusting the X-ray incidence plane to a small angle (typically below 1°), as shown in **Figure 3.26b**. When the XRD measurement of WSe_2 monolayers/bilayers is performed in Bragg–Brentano geometry, the XRD pattern only shows a weak and broad XRD peak, while the GIXRD pattern shows the peaks of both WSe_2 and substrate Al_2O_3 (**Figure 3.26c,d**).[117] However, XRD measurement cannot be focused on monolayer only due to the spot size of a few mm for conventional lab X-ray diffractometers. Therefore, XRD is only used to characterize substrates in this thesis, as discussed in **Chapter 5**.

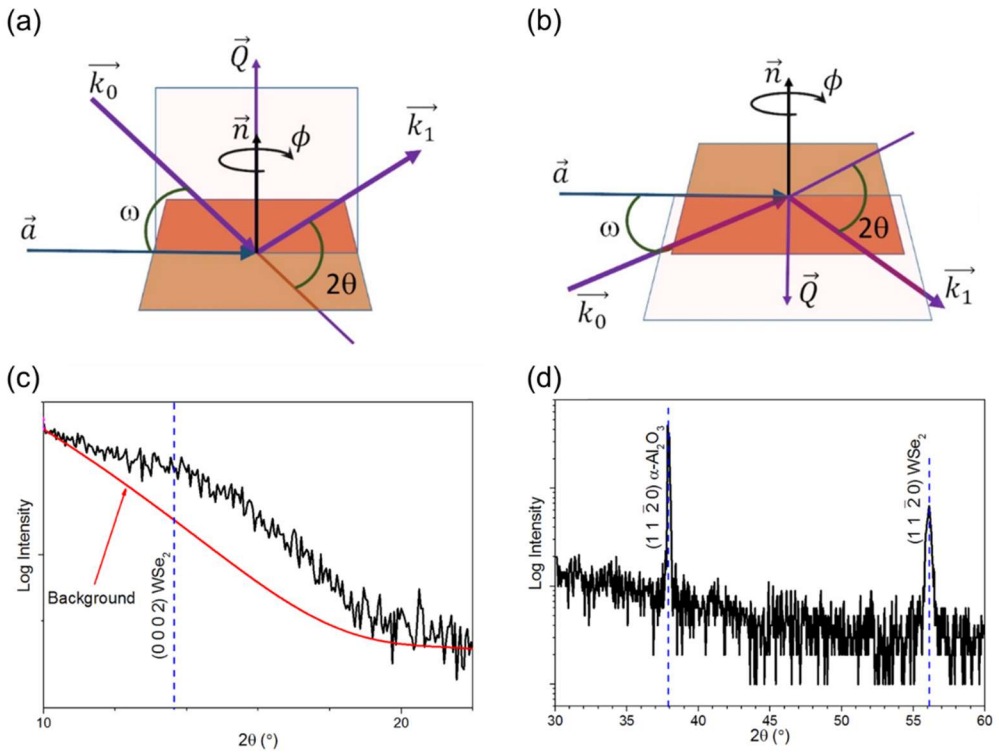

Figure 3.26. XRD measurements performed in Bragg–Brentano geometry and in-plane geometry. (a–b) Schematic of XRD performed in (a) Bragg–Brentano geometry, and (b) in-plane geometry. (c–d) XRD patterns of WSe_2 sample measured in (c) Bragg–Brentano geometry, and (d) in-plane geometry, respectively. The former XRD pattern in (c) only shows a weak and broad peak, and the latter in (d) shows sharper peaks from WSe_2 and α-Al_2O_3. Reproduced from Ref. [117].

3.3 Defect Generation & Passivation in 2D TMDs

In **Chapter 4**, sulfur vacancies are generated in 2D TMDs by annealing in an Ar/H_2 (95 *vol.*%/5 *vol.*%) atmosphere to generate defects. I briefly describe this process here. Prior to Ar/H_2 annealing, samples were annealed in a high-purity N_2 (99.9999%) atmosphere to remove volatile adsorbed contaminants. Mechanically exfoliated samples were annealed in N_2 in a 1-inch quartz tube in the single-zone furnace, as shown in **Figure 3.27**. A new tube II was used for annealing to avoid contamination. Before the first use, the tube was cleaned by annealing in Ar/H_2 at 1000 °C for 30 min. For N_2 annealing of 2D TMDs, the furnace tube was filled with flowing 450 sccm N_2 for 10 min to remove residual oxygen and then heated to 250 °C for 1 h under 100 sccm N_2. After each annealing, the furnace was cooled back to room temperature at a rate of 20 °C/min, and samples were removed from the tube for measurement. To maintain

the as-annealed condition, samples were stored in glovebox to minimize the exposure to air throughout this study.

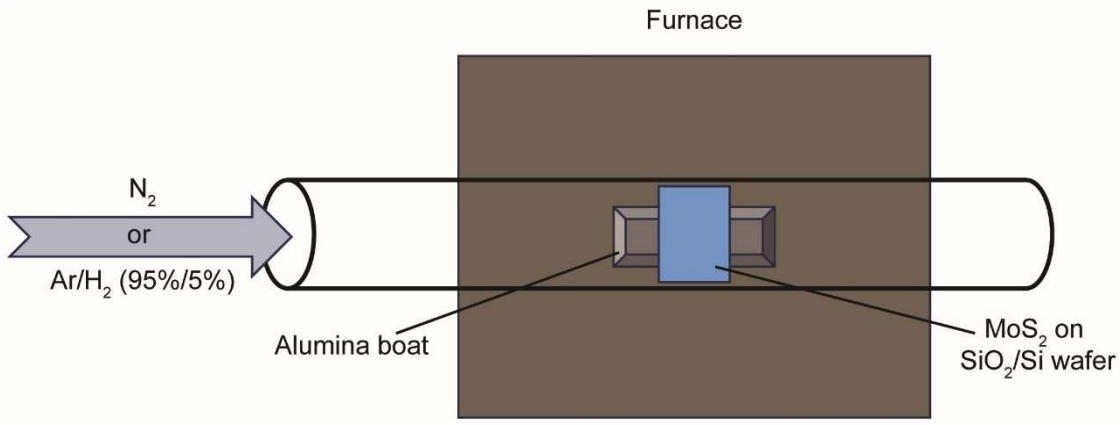

Figure 3.27. Schematic of annealing MoS_2 in a N_2 or Ar/H_2 (95 vol.%/5 vol.%) atmosphere.

I also tried to wash off the contaminants from mechanical transfer by immersing samples in acetone/IPA (30/15 mins). RT PL spectroscopy was performed to characterize the samples across different cleaning methods. As shown in **Figure 3.28a–d**, the PL spectra were deconvoluted to extract the ratio of the integrated intensity of A^- trion to A exciton, $I(A^-)/I(A)$, to show the electron doping level. This ratio was found to decrease from 0.84 ± 0.33 for as-exfoliated MoS_2, to 0.40 ± 0.04 for acetone/IPA washed MoS_2, further to 0.26 ± 0.02 for N_2 annealed MoS_2, showing that the native n-type doping of MoS_2 is partially induced by extrinsic contaminants and can be suppressed by proper cleaning methods (**Figure 3.28e**). The lowest $I(A^-)/I(A)$ ratio observed in N_2 annealed MoS_2 suggests that N_2 annealing is more effective in removing contaminants than acetone/IPA washing.

After N_2 annealing and RT PL measurement, samples are annealed in Ar/H_2 (95 *vol.*%/5 *vol.*%) for defect generation. The tube used for Ar/H_2 annealing was the same tube II used for N_2 annealing. As shown in **Figure 3.27**, samples were prepared by flowing 450 sccm Ar/H_2 (95 *vol.*%/5 *vol.*%) for 10 min to displace tube oxygen and heated to 200 °C under 70 sccm Ar/H_2 for 10 min to remove tube moisture. Then samples were heated to the target annealing temperature (*e.g.*, 600 °C) and held for the target time (*e.g.*, 30 min).

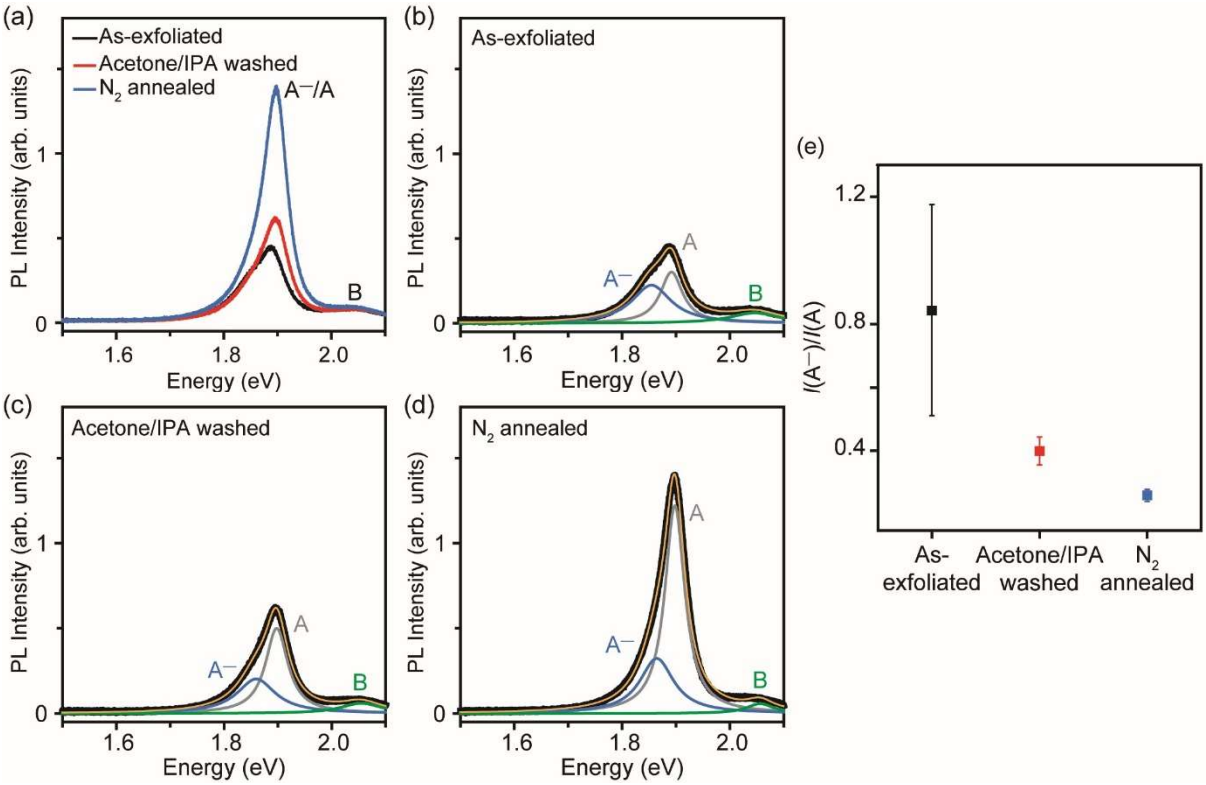

Figure 3.28. Room-temperature PL spectra of exfoliated pristine monolayer MoS_2 with different cleaning methods. (a) PL spectra of as-exfoliated, acetone/IPA washed, and N_2 annealed MoS_2, showing A^-/A peak and B exciton peak. (b–d) Deconvoluted PL spectra of (b) as-exfoliated MoS_2, (c) acetone/IPA washed MoS_2, and (d) N_2 annealed MoS_2, fitted with Lorentz peaks. Denotation: A exciton in grey, A^- trion in blue, B exciton in green, and cumulative fit curve in yellow. (e) The ratio of the integrated intensity of A^- trion to A exciton, $I(A^-)/I(A)$, for as-exfoliated, acetone/IPA washed, and N_2 annealed MoS_2. The $I(A^-)/I(A)$ ratio reaches the minimum in the N_2 annealed MoS_2.

High flow rate of 450 sccm prior to annealing is necessary to remove air from tube. As shown in **Figure 3.29a–d**, without this step, exfoliated monolayer MoS_2 annealed at 500 – 600 °C for 30 mins show significant damage, demonstrating non-reproducible results. Similarly, CVD-grown monolayer MoS_2 flakes show sample damage in **Figure 3.29e**,**f**.

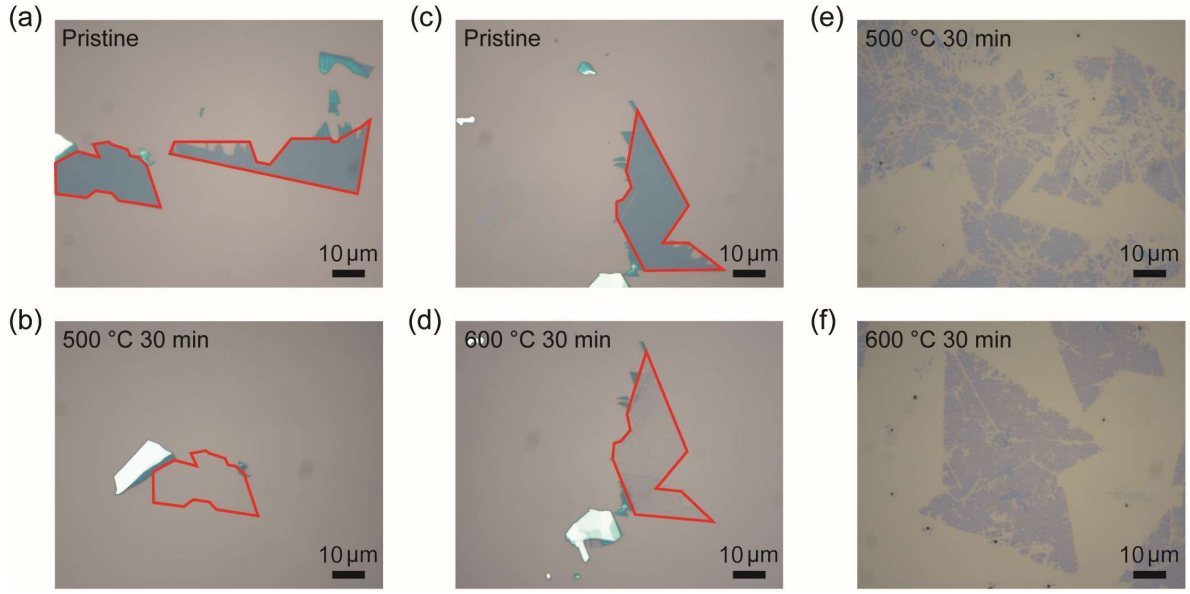

Figure 3.29. Optical microscopy images of monolayer MoS_2 annealed in Ar/H_2 (95 vol.%/5 vol.%) without pre-flowing the annealing tube, showing significant damage. (a–d) Optical microscopy images of mechanically exfoliated monolayer MoS_2 (a,c) before and (b,d) after annealing at 500 °C and 600 °C, respectively. (e,f) Optical microscopy images of CVD-grown monolayer MoS_2 flakes annealed at (e) 500 °C, and (f) 600 °C, respectively. The flakes are almost gone after annealing due to presence of residual oxygen.

In **Chapter 4**, defective 2D TMDs are passivated by annealing in sulfur/selenium vapor. As shown in **Figure 3.30**, for defect passivation, 2D TMDs were placed on alumina boat 1 and 8 mg sulfur or selenium powder was placed in alumina boat 2. Alumina boats 1 and 2 were placed in the center and upstream of a 1-inch tube in the single furnace, respectively. 450 sccm N_2 was introduced into the tube for 10 min and then heated to the target annealing temperature (*e.g.*, 500 °C) under 50 sccm N_2 and kept for 30 min. The position of sulfur (or selenium) was determined by measuring the temperature profile of the furnace using an external thermocouple. Sulfur (or selenium) was put at the position that reached 150 °C (or 250 °C) when 2D TMDs at the furnace center reached the target temperature. To avoid contamination, I used new quartz tubes III for sulfur annealing and IV for selenium annealing. Alumina boats were also separated for sulfur and selenium.

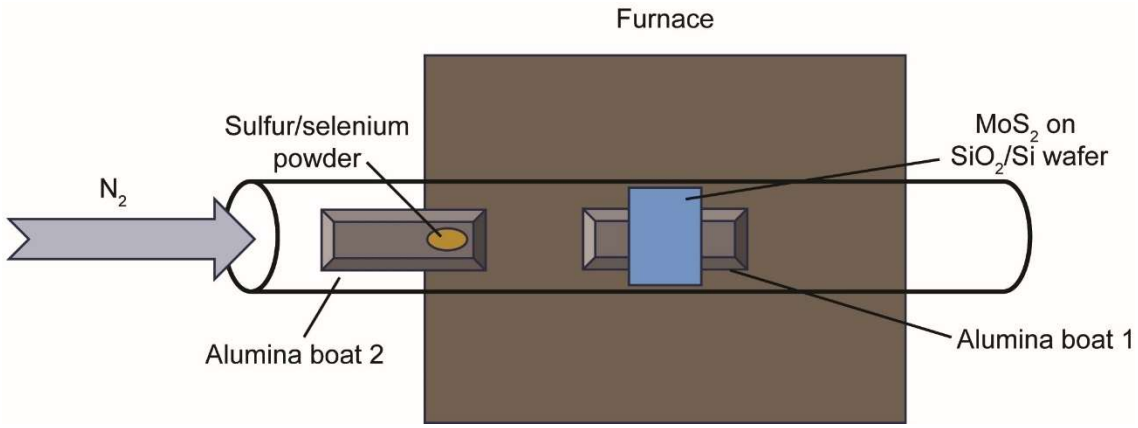

Figure 3.30. Schematic of annealing defective MoS_2 in sulfur or selenium vapor.

3.4 Wet Transfer of 2D TMDs

In **Chapter 5**, 2D TMDs are wet-transferred across various dielectric substrates to investigate the influence of substrates on PL from sulfur vacancies. The transfer of exfoliated TMDs is largely limited by the strong adhesion between exfoliated flakes and the substrate. To transfer exfoliated TMDs, an adhesive stamp is required to overcome the adhesion between annealed monolayers and the substrate. Hence poly(bisphenol A carbonate) (PC) stamp was used to assist the transfer (see **Figure 3.31**). PC dissolved in chloroform was first drop-cast on the annealed sample to form a uniform film ①. A PDMS stamp was stacked on a glass slide and attached to the transfer stage with PDMS stamp face-down ②. The PDMS stamp was brought in contact with the PC stamp to form a firm stack ③. The PDMS/PC stack was raised to pick up the target flake from substrate 1 ④. The detached substrate 1 was replaced by another substrate 2 ⑤. The PDMS/PC stack was aligned and brought in contact with substrate 2 and heated to 180 °C for 1 min to melt PC and weaken the adhesion between PDMS and PC ⑥. The PDMS stamp was raised to detach from PC, depositing the target flake on substrate 2 ⑦. The sample was immersed in chloroform for 10 mins to dissolve the melted PC stamp ⑧, leaving the target flake on substrate 2 ⑨.

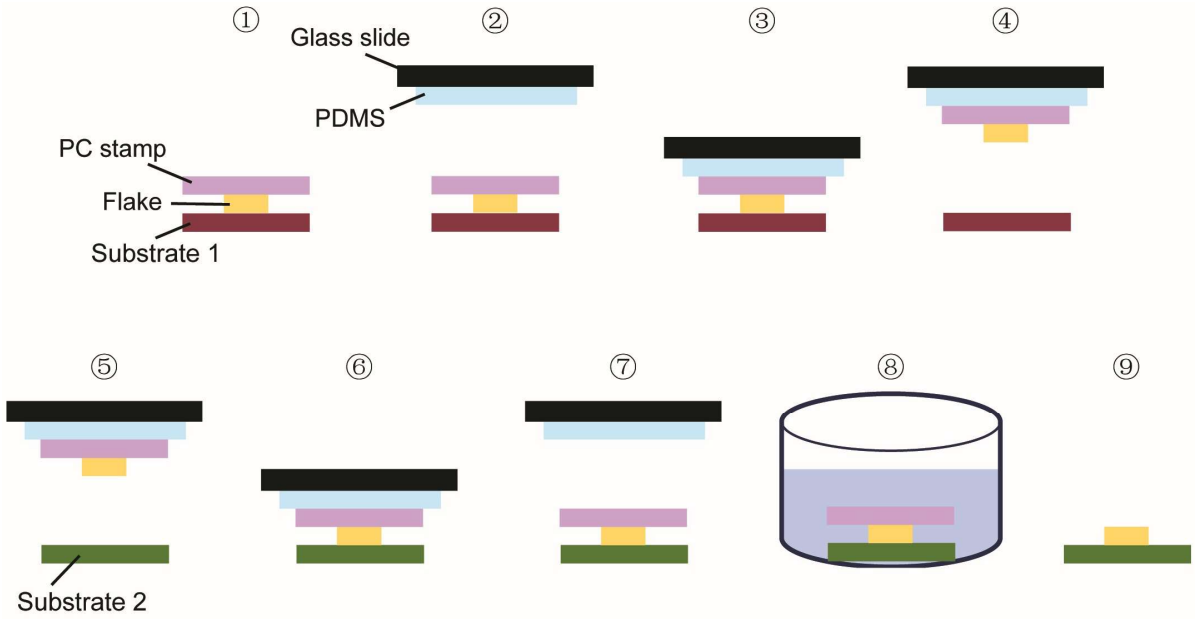

Figure 3.31. Schematic of wet transfer of exfoliated TMDs across various substrates. Steps ① – ⑧ are described in the text.

This PC-assisted wet-transfer method was optimized by transferring pristine MoS_2 from one SiO_2/Si substrate to another SiO_2/Si substrate and monitoring the morphology and PL changes. The optical microscopy images in **Figure 3.32** show that the transferred flake can maintain the high quality of 2D TMDs without new wrinkles or cracks.

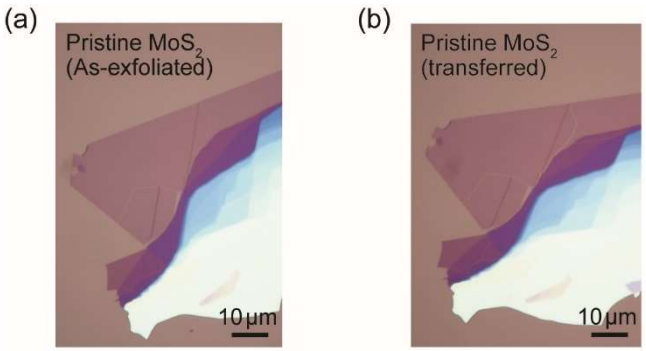

Figure 3.32. Optical microscopy images of exfoliated pristine MoS_2 (a) before and (b) after transfer from a SiO_2/Si substrate to another SiO_2/Si substrate. The transferred flake maintains the high quality, without new wrinkles or cracks.

The transferred flakes were characterized by AFM. On the transferred monolayer MoS_2, PC residues were observed across the whole flake (**Figure 3.33a**). As shown in **Section 3.3**, the PL features of monolayer TMDs are sensitive to extrinsic contaminants that can be identified using the ratio of the integrated intensity of A^- trion to A exciton, $I(A^-)/I(A)$. This ratio increases from 0.47 ± 0.05 in the as-exfoliated sample to 0.84 ± 0.09 in the transferred sample, shown in **Figure 3.33,c**. To remove the PC residues, the transferred sample was post-annealed in Ar/H_2 (95 *vol*.%/5 *vol*.%) at 350 °C for 1 h. AFM image in **Figure 3.33d** shows that the sample was cleaned by post-annealing with the $I(A^-)/I(A)$ ratio restoring to 0.44 ± 0.13 – comparable to the as-exfoliated pristine MoS_2 samples, shown in **Figure 3.33e,f**.

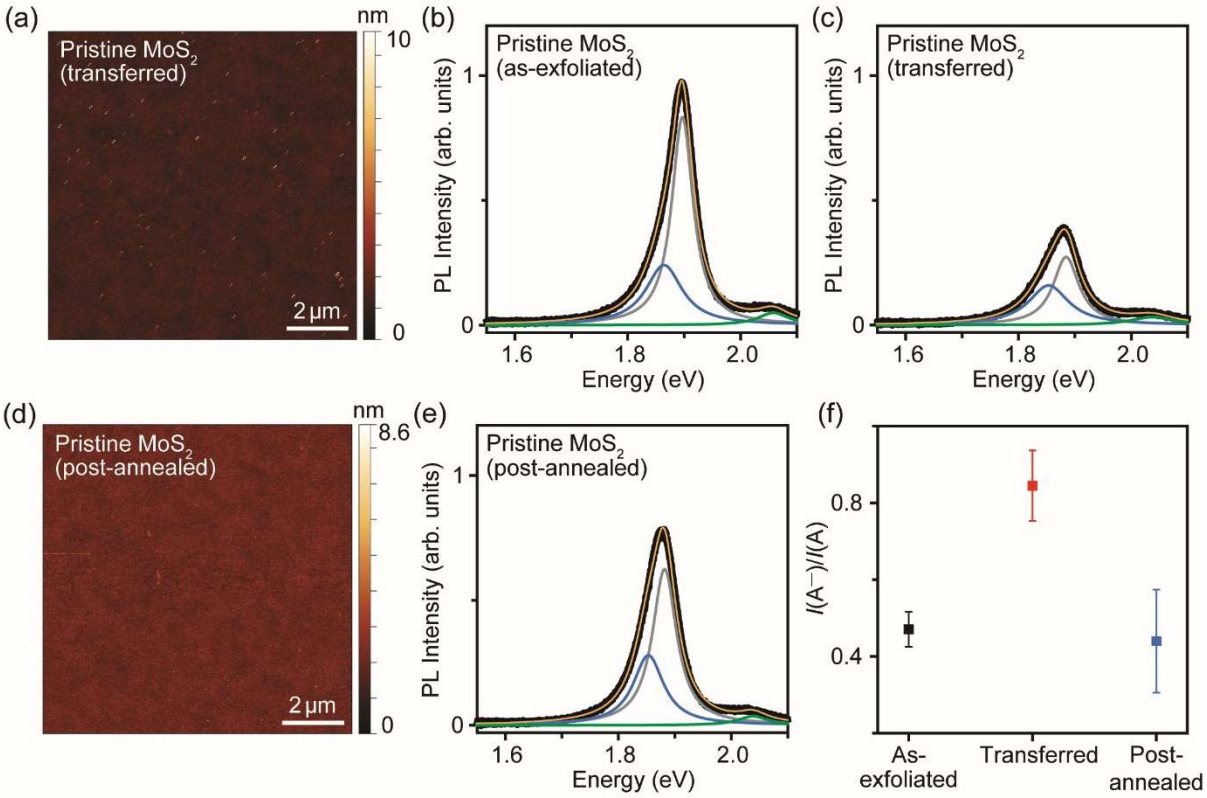

Figure 3.33. Transfer and post-annealing of pristine MoS_2. (a,d) AFM image of transferred and post-annealed pristine monolayer MoS_2. The transferred sample shows PC residues across the whole flake while post-annealed sample shows a clean surface without noticeable residues. (b,c,e) PL spectra of pristine MoS_2 (b) before and (c) after transfer and (e) after post-annealing fitted with Lorentz peaks. Denotation: A exciton in grey, A^- trion in blue, B exciton in green, and cumulative fit curve in yellow. (f) The ratio of the integrated intensity of A^- trion to A exciton, $I(A^-)/I(A)$, for pristine, transferred, and post-annealed MoS_2. The ratio is increased by transferring the flake and restored by post-annealing.

Chapter 4 Photoluminescence from Sulfur Vacancies in Monolayer MoS_2

In this chapter, absorption and photoluminescence (PL) from sulfur vacancy-induced in-gap states (**Section 3.2.3** and **3.2.4**) were used to investigate changes in the electronic structure of 2D TMDs. Absorption from such defect states has been observed at room temperature (RT, ~300 K),[118] whereas light emission from excitons bound to defect states is typically observed at low temperatures (≤77 K).[119,120] The localization of excitons at defects leads to long lifetimes for defect-mediated emission.[107] In this chapter, I demonstrate that it is possible to observe emission from trapped excitons (labelled as LX_D) at RT when defect density (n_d) is in the range of 10^{13} cm^{-2} < n_d < 10^{15} cm^{-2}. The influence of temperature and excitation power on LX_D emission is explored. Time-resolved PL measurements reveal that the lifetime of LX_D emission is longer than band edge excitons, both at room and low temperatures (~2.44 ns at 8 K). In this chapter, I designed the experiments, synthesized samples, and conducted Raman and PL measurements at RT. Synchrotron XPS was done by Dr. Yan Wang and Mr. Han Yan. RT reflection spectra, PL imaging and time-resolved PL measurements at RT were done by Dr. Juhwan Lim. Low-temperature PL spectra, PL mapping, and time-resolved PL measurements were measured by Dr. Zhepeng Zhang. This chapter has been published on ACS Nano.

4.1 Defect Generation in Exfoliated Monolayer MoS_2

4.1.1 Defect Generation by Ar/H_2 Annealing

Monolayer MoS_2 samples on SiO_2 (300 nm)/Si wafers were prepared by mechanical exfoliation, as described in **Section 3.1**. To generate sulfur vacancies, the samples were annealed in an Ar/H_2 (95 *vol.*%/5 *vol.*%) atmosphere for 30 min at temperatures ranging from 300 to 650 °C (see schematic in **Figure 4.1a**). The RT Raman spectrum of pristine monolayer MoS_2 in **Figure 4.1b** shows that it consists of a characteristic E^1_{2g} in-plane mode peak at ~385 cm^{-1} and A_{1g} out-of-plane mode peak at ~405 cm^{-1}.[121] The weak satellite peak at ~380 cm^{-1} is generally assigned to a longitudinal optical branch phonon LO(*M*) due to sulfur vacancies.[112,122] The intensity of the defect mode increases with annealing from 300 – 600 °C, indicating an increases in sulfur vacancy creation (**Figure 4.1c**). The most intense LO(*M*)

defect mode was found in 600 °C annealed MoS_2. Above 600 °C, I observed a change in optical contrast due to material damage (**Figure 4.1d**).

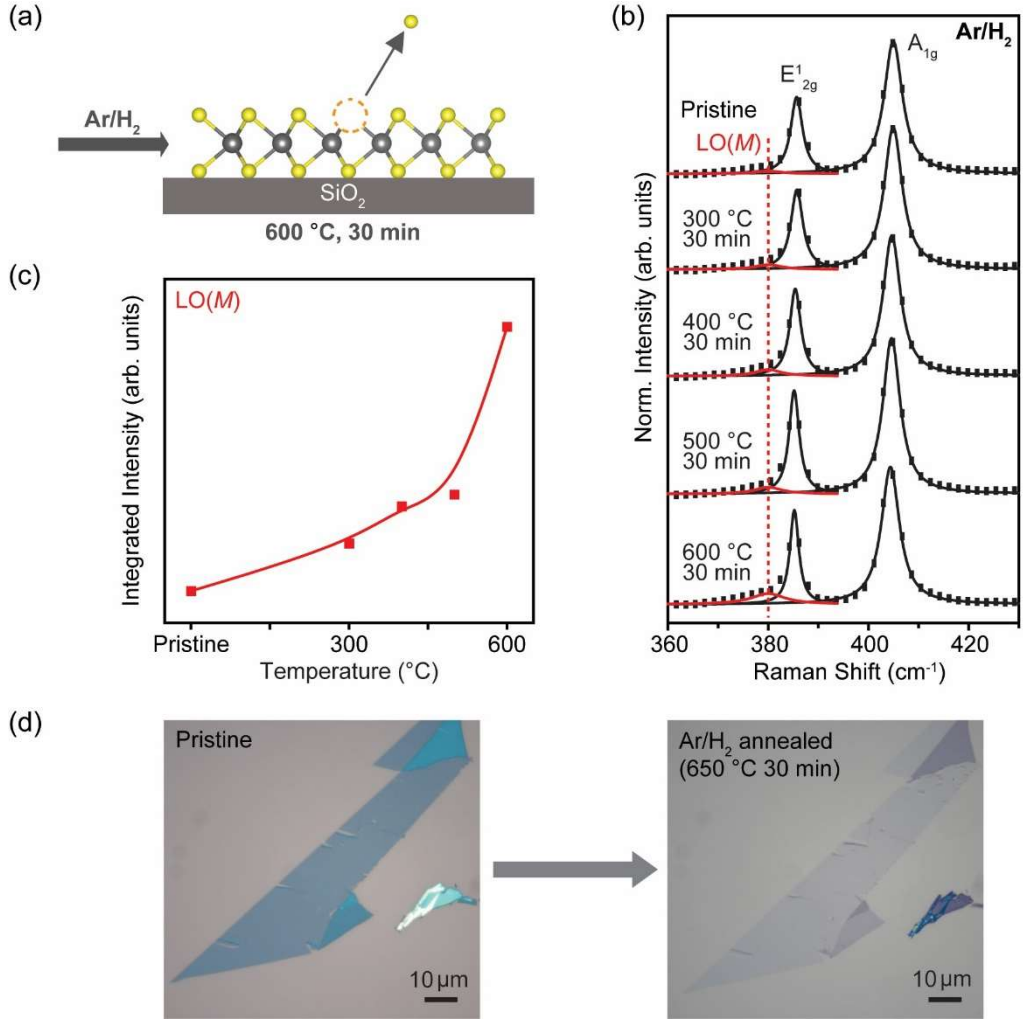

Figure 4.1. Defect generation in monolayer MoS_2 by annealing in Ar/H_2 (95 vol.%/5 vol.%). (a) Schematic of sulfur vacancy generation. (b) Raman spectra of pristine and Ar/H_2 annealed (300 – 600 °C) monolayer MoS_2 through Ar/H_2 annealing, normalized to the intensity of Si reference peak. The spectra are fitted with Lorentz peaks. Pristine MoS_2 shows an E^1_{2g} in-plane mode and A_{1g} out-of-plane mode, denoted in black. The low-frequency shoulder on the left of E^1_{2g} mode indicates the LO(M) defect mode, denoted in red. The increased intensity of the defect mode in annealed MoS_2 indicates generation of sulfur vacancies. (c) Integrated intensity plot of the LO(M) mode as a function of annealing temperature. The red line is a guide to the eye. (d) Optical microscopy images of monolayer MoS_2 before and after 650 °C Ar/H_2 annealing, showing material damage through annealing.

Synchrotron X-ray photoelectron spectroscopy (XPS) at Diamond Light Source was used to obtain information about the defects in annealed samples (**Figure 4.2**). The exfoliated monolayer flakes (lateral size of ~20 μm, similar to the x-ray beam spot size) were grounded using electron-beam lithographically patterned In/Au electrodes[115] to avoid charging during XPS. The electron beam lithography (EBL) follows a standard procedure: spin-coating electron-beam resist MMA 495 EL6 and then PMMA 950 A6, electron-beam exposure, resist development, metal deposition by electron-beam evaporator, and lift-off. For transporting samples from Cambridge to Diamond Light Source, the samples were sealed in vacuum in glovebox using Geryon vacuum sealer machine to minimize exposure to air.

For the XPS measurements, the samples were baked at 80 °C in XPS preparation chamber with base pressure of 10^{-7} mbar for one hour to remove physisorbed species. The samples were then transferred to analysis chamber (10^{-10} mbar). Radiation damage tests using 3 keV X-rays were performed. No obvious changes in the XPS spectra were observed over several measurements at a fixed sample position (**Figure 4.2a**), indicating that beam-induced number of defects during measurements is small. XPS spectra of Mo 3d doublet were measured using 1 keV soft X-rays. The binding energies were calibrated by using Au 4f core level of Au electrode as reference. Pristine MoS_2 shows the characteristic Mo 3d doublet corresponding to the binding energy of stoichiometric MoS_2 at 230.4 eV (Mo $3d_{5/2}$).[123] The XPS results were fitted with Casa XPS software, using a Shirley background and line shape LA(2,1.2,100). Referring to XPS fitting database, each Mo $3d_{3/2}$ – $3d_{5/2}$ doublet was constrained with position separation of 3.1 eV, peak area ratio of 2:3 (Mo $3d_{3/2}$: $3d_{5/2}$), and equal full width at half maximum (FWHM). No constraint was used for S 2s peak. The chi-square was always below 3.5.

The annealed MoS_2 shows the Mo 3d doublet of stoichiometric MoS_2 at 231.0 eV (Mo $3d_{5/2}$), as well as peaks from nonstoichiometric MoS_x ($0<x<2$) at 230.1 eV (Mo $3d_{5/2}$), respectively. The defect concentration for both pristine and annealed MoS_2 are extracted from stoichiometry calculation, using the core level spectra of Mo 3d and S 2s. The actual stoichiometry is given by:

$$\frac{\mathrm{S}\ (at.\%)}{\mathrm{Mo}\ (at.\%)} = \left(\frac{I_{\mathrm{S\ 2s}}}{\sigma_{\mathrm{S\ 2s}}}\right)/\left(\frac{I_{\mathrm{Mo\ 3d\ 5/2}}}{\sigma_{\mathrm{Mo\ 3d\ 5/2}}}\right)$$

here, S $(at.\%)$ and Mo $(at.\%)$ are the atomic percents $(at.\%)$ of S and Mo, $I_{\mathrm{S\ 2s}}$ and $I_{\mathrm{Mo\ 3d\ 5/2}}$ are the integrated intensities of S 2s peak and Mo $3d_{5/2}$ peak. $\sigma_{\mathrm{S\ 2s}}$ and $\sigma_{\mathrm{Mo\ 3d\ 5/2}}$ are the

photoionization cross-sections at photon energy of 1 keV modeled by Scofield, where $\sigma_{S\ 2s}$ = 0.44168, and $\sigma_{Mo\ 3d\ 5/2}$ = 2.4679.[124] For pristine MoS_2, the actual stoichiometry is calculated to be $MoS_{1.99\pm0.03}$ which leads to a defect concentration of 0.5±1.5%. In a perfect superstructure of 1H MoS_2, the sulfur-sulfur distance is 3.162 Å,[18] thus the density of S atoms in monolayer MoS_2 can be calculated to be ~2.3×10^{15} cm^{-2}. For a defect concentration of 0.5%, the defect density is approximated to be ~1.15×10^{13} cm^{-2}, similar to reported values on pristine sample.[8] For the annealed MoS_2, the calculated stoichiometry is $MoS_{1.84\pm0.02}$ with a defect concentration of ~7.7±0.8%, equivalent to a sulfur vacancy density of ~$1.8\pm0.2\times10^{14}$ cm^{-2}. It is worth noting that for the defective sample, the Mo 3d doublet is shifted to higher binding energies by

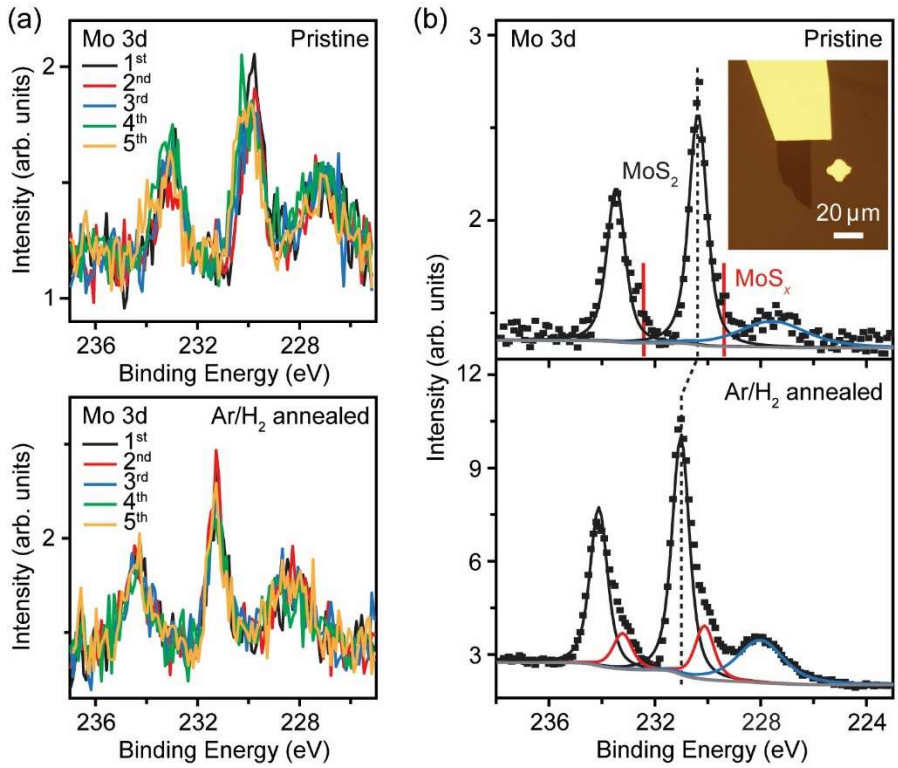

Figure 4.2. Synchrotron XPS measurements of pristine and 600 °C Ar/H_2 annealed monolayer MoS_2. (a) Synchrotron X-ray radiation damage tests of (top) pristine and (bottom) Ar/H_2 annealed monolayer MoS_2 using 3 keV X-rays. No obvious damage in MoS_2 is observed. (b) XPS spectra of the Mo 3d core level in pristine and Ar/H_2 annealed MoS_2. This measurement was performed using 1 keV X-rays. Pristine MoS_2 shows the characteristic Mo 3d doublet from stoichiometric MoS_2 (denoted in black) and S 2s peak (denoted in blue). Annealed MoS_2 shows a second Mo 3d doublet from nonstoichiometric MoS_x ($0<x<2$, denoted in red). Inset: Optical microscopy image of monolayer MoS_2 grounded with In/Au electrode. Scale bar = 20 µm.

0.6 eV (as indicated by the dashed vertical red line in **Figure 4.2b**), indicating electron doping mediated by sulfur vacancies – consistent with donor states detected by scanning tunneling microscopy/spectroscopy[86] and deep-level transient spectroscopy (DLTS)[125].

There is a question whether the sulfur vacancies are oxidized when the samples are exposed to air. However, my analysis suggests that the sulfur vacancies generated in the Ar/H_2 annealed MoS_2 are unlikely to be oxidized. Kong's group showed that it was possible to incorporate oxygen in CVD-grown MoS_2.[164] Compared to MoS_2 grown without oxygen, the oxygen-incorporated MoS_2 shows Mo–O bond at higher binding energies in the XPS spectra while the non-stoichiometric MoS_x XPS peak in my Ar/H_2 annealed MoS_2 appears at lower binding energies. Therefore, I tend to believe that chemisorption of oxygen at sulfur vacancies is unlikely to be the case in the Ar/H_2 annealed MoS_2. However, the possibility of physisorption of oxygen (or other molecules) cannot be excluded.

4.1.2 Room-temperature Photoluminescence from Sulfur Vacancies

The defects generated through annealing lead to the formation of electronic in-gap states in monolayer MoS_2, as shown in the schematic energy band diagram in **Figure 4.3a** – consistent with the band structure of sulfur-deficient monolayer MoS_2 by density functional theory (DFT) calculations.[74] The grey arrow (neutral exciton A) represents an electron in the conduction band (CB) recombining with a hole in the valence band (VB). The blue arrow (negative trion A^-) represents the recombination of two electrons and a hole. The red arrow (LX_D) represents a localized electron recombing with a hole. PL spectroscopy (**Figure 4.3b,c**) and reflectance measurements (**Figure 4.3d**) were used to characterize the RT optical properties of monolayer MoS_2. In pristine MoS_2, the RT PL spectrum shows the characteristic A^- trion/A exciton (A^-/A) peak at 1.90 eV and B exciton peak at 2.05 eV. The reflectance spectrum shows corresponding A (1.91 eV) and B (2.06 eV) excitonic transitions.[126] For the 600 °C Ar/H_2 annealed sample, the RT PL spectrum shows a low-energy localized emission peak, LX_D, that originates from defect-induced in-gap states with a large binding energy of 185 meV. The LX_D emission results from excitonic transitions between one unoccupied, in-gap defect state lying ~0.6 eV below the conduction band minimum (CBM), and the other energy state at the valence band maximum (VBM).[74] For monolayer MoS_2, the binding energy of A exciton is ~0.41 eV. Therefore, the binding energy of defect-mediated emission can be approximated to be ~190 meV, which

matches the binding energy of 185 meV of LX_D peak in the PL results. The reflectance spectrum is also broadened in the defective sample. Below 600 °C, the RT LX_D emission peak emerges weakly at 500 °C.

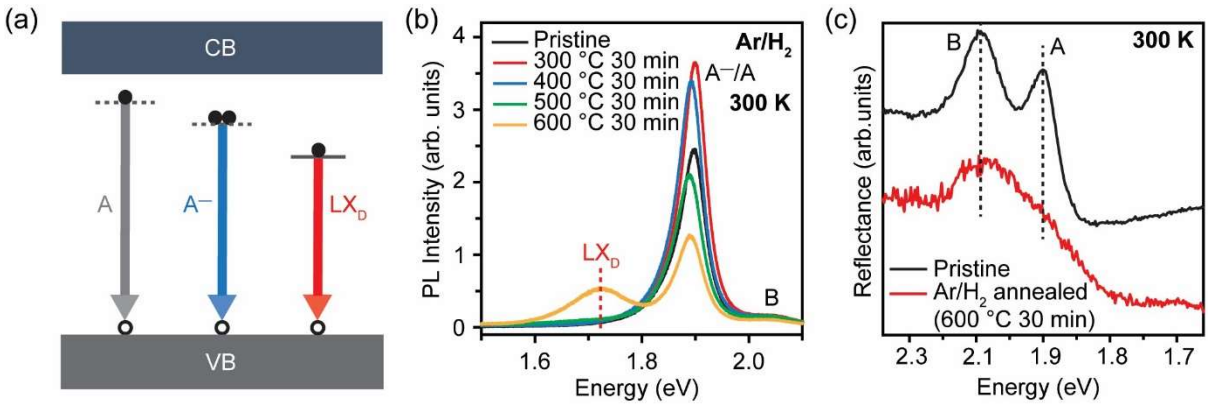

Figure 4.3. RT optical properties induced by sulfur vacancies in monolayer MoS_2. (a) Proposed energy band diagram of sulfur-deficient monolayer MoS_2. The horizontal dashed lines represent virtual energy states due to exciton binding energy, while the horizontal solid line represents real energy states due to defects. (b) RT PL spectra of monolayer MoS_2 annealed in an Ar/H_2 atmosphere at different temperatures. The pristine MoS_2 shows A^- trion/A exciton (A^-/A) and B exciton emission. With annealing temperature increasing, a low-energy localized emission LX_D weakly starts to appear at 500 °C and reaches its maximum at 600 °C. (c) Reflectance spectra of pristine and 600 °C Ar/H_2 annealed monolayer MoS_2. Pristine MoS_2 indicates the reflectance signals of A exciton and B exciton. The broadening of reflectance spectrum of annealed MoS_2 indicates presence of in-gap defect states.

The RT PL spectra of pristine and 600 °C Ar/H_2 annealed MoS_2 were deconvoluted to extract the ratio of integrated intensity of A^- trion to A exciton, $I(A^-)/I(A)$ (**Figure 4.4a,b**) to indicate electron doping level.[38] The ratio was found to increase from 0.44 in pristine MoS_2 to 1.06 in 600 °C Ar/H_2 annealed MoS_2, indicating increased electron doping from creation of sulfur vacancies – consistent with the XPS peak shift shown in **Figure 4.2b**. The results are reproducible and consistent across 22 samples, as shown in the statistical histogram in **Figure 4.4c**. The A exciton peak is found at 1.888 ± 0.005 eV, together with the A^- trion peak at 1.864 ± 0.007 eV, and LX_D peak at 1.716 ± 0.005 eV.

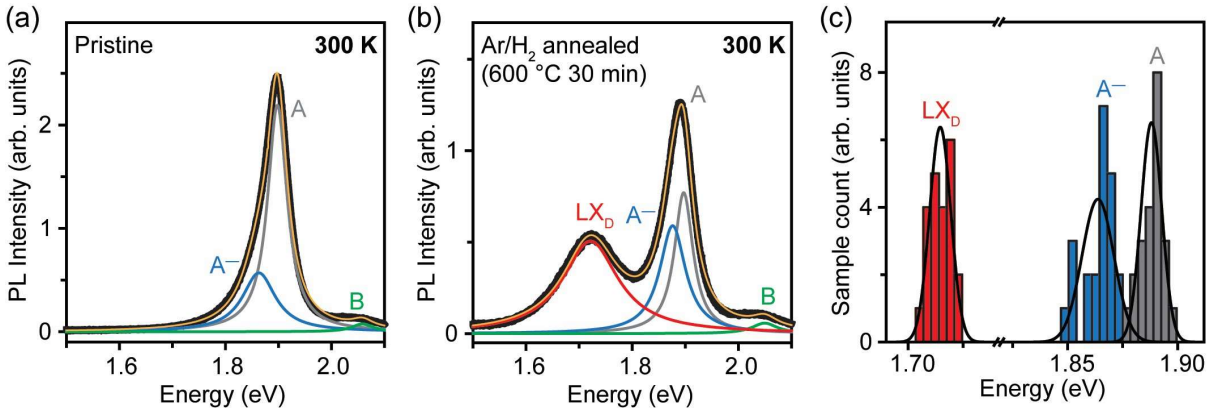

Figure 4.4. Deconvolution of RT PL spectra for pristine and 600 °C Ar/H_2 annealed monolayer MoS_2. (a–b) Deconvoluted RT PL spectra of (a) pristine and (b) 600 °C Ar/H_2 annealed MoS_2, fitted with Lorentz peaks. Denotation: A exciton in grey, A^- trion in blue, B exciton in green, LX_D emission in red, and cumulative fit curve in yellow. (c) Statistical histogram of emission energy of A, A^-, and LX_D emission for 22 individual 600 °C Ar/H_2 annealed samples. LX_D emission appears consistently and reproducibly.

To understand the role of H_2 in defect generation, monolayer MoS_2 were annealed in an inert Ar-only atmosphere. Similar to the Ar/H_2 annealed samples, the Ar-annealed samples show presence of defect mode LO(*M*) in Raman spectra. The LO(*M*) mode weakly emerges with annealing from 300 – 500 °C and then disappears at 550 °C, indicating minor defect generation through Ar-only annealing (**Figure 4.5a**). The presence of only very weak LO(*M*) mode is consistent with absence of the LX_D peak at RT (**Figure 4.5b**). Above 550 °C, monolayer MoS_2 disappears while few-layer flake significantly degrades, as indicated by the optical microscopy images (**Figure 4.5c**).

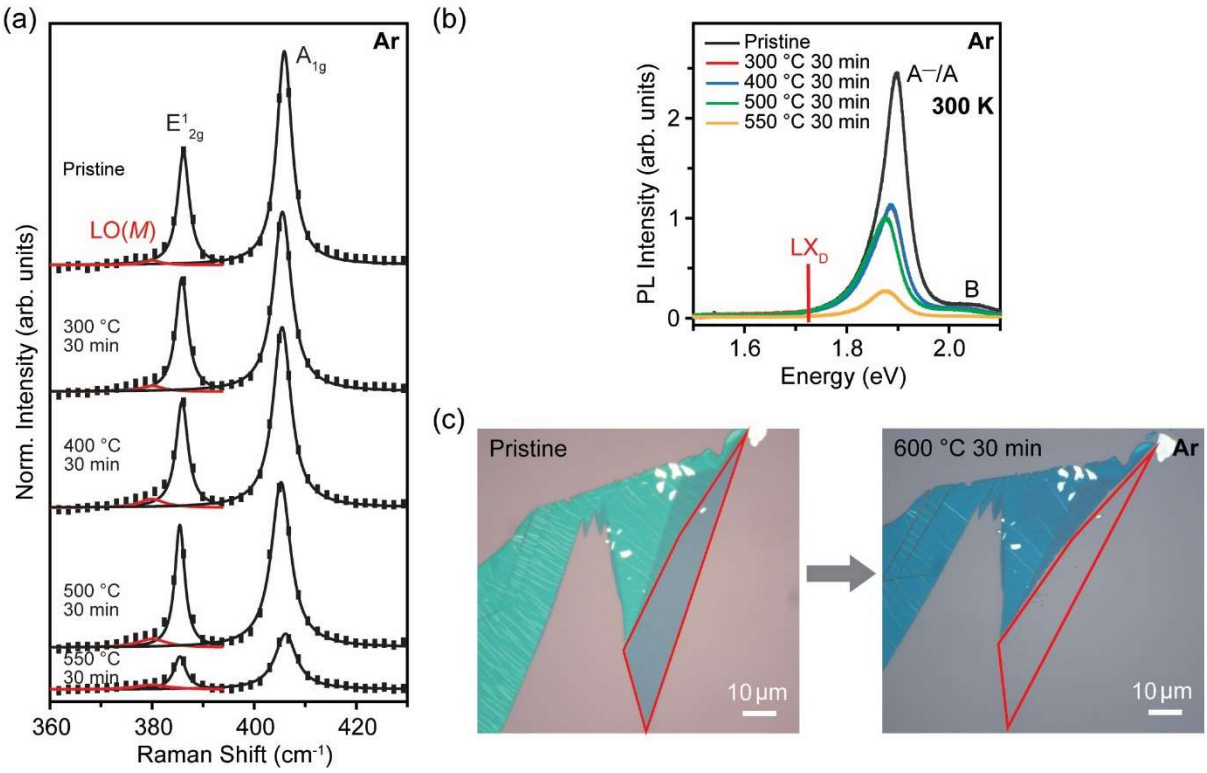

Figure 4.5. Evolution of monolayer MoS_2 annealed in an Ar-only atmosphere. (a) Raman spectra of monolayer MoS_2 through 300 – 550 °C Ar annealing, normalized to the intensity of Si reference peak. The normalized intensity of LO(M) defect mode (denoted in blue) slightly increases with ≤500 °C Ar annealing and then decreases at 550 °C Ar annealing. (b) RT PL spectra and (c) their normalized spectra through 300 – 550 °C Ar annealing, showing an absence of LX_D emission. (c) Optical microscopy images of pristine and 600 °C Ar annealed monolayer MoS_2, showing degradation of monolayer flake.

4.1.3 In-gap States Induced by Sulfur Vacancies

To understand how localization of excitons at defect states is related to evolution of the LX_D peak, temperature-dependent PL was measured (**Figure 4.6**). For pristine MoS_2 at 10 K, the most intense peak is the LX_N peak which is generally attributed to native adsorbates[127], with a weakened A^-/A peak (**Figure 4.6a**). In contrast, for the annealed MoS_2, the most intense emission peak is the LX_D peak, with the LX_N and A^-/A peaks significantly suppressed. The emission energy of LX_D is consistent with that of sulfur-vacancy-induced emission generated by *in-vacuo* annealing[127], focused He^+ irradiation[127], and proton irradiation[107]. As the samples were cooled from 300 K to 10 K, the dominant recombination pathway shows a transition from A^-/A to LX_N emission in the case of pristine MoS_2. For the between the LX_D peak in my Ar/H_2

annealed sample and the defect emission generated by *in-vacuo* annealing further supports that the optically active sulfur vacancies remain 600 °C Ar/H_2 annealed sample, transition from A^-/A to LX_D emission indicates localization of excitons at lower-lying in-gap states. The adsorbates-related emission LX_N can be suppressed by full encapsulation in hexagonal boron nitride, as shown in **Figure 4.6b**.[128–130]

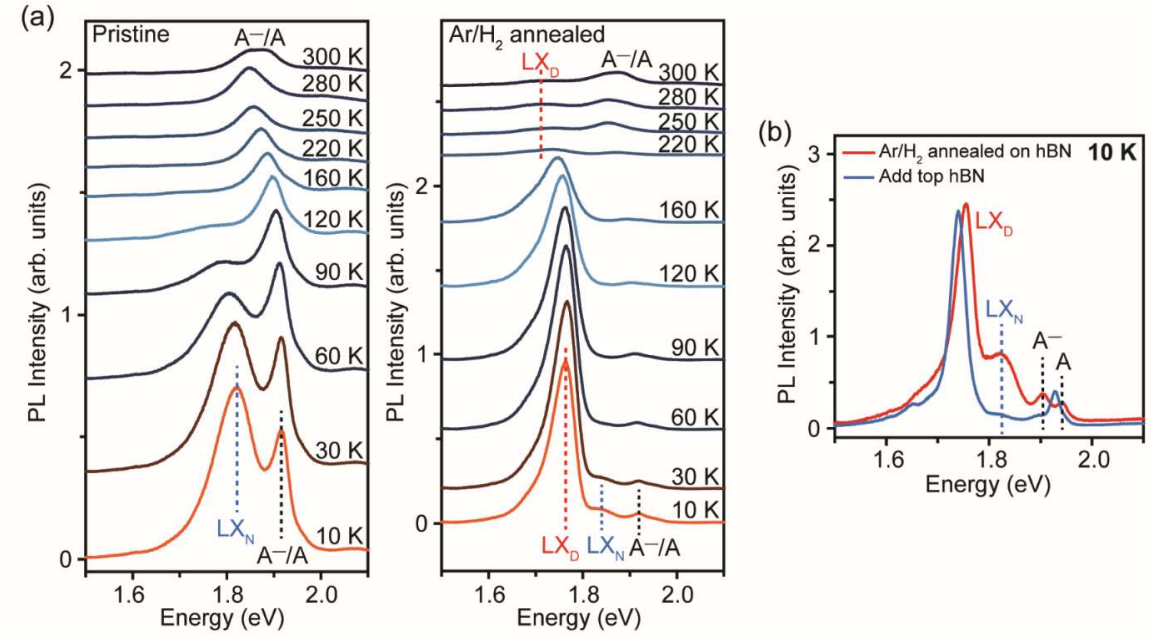

Figure 4.6. In-gap states induced by sulfur vacancies. (a) Temperature-dependent PL spectra of pristine and 600 °C Ar/H_2 annealed monolayer MoS_2. At 10 K, the LX_N peak is attributed to native adsorbates, while LX_D is attributed to sulfur vacancies. The continuous increase of LX_N and LX_D over the A^- trion/A exciton emission with decreasing measurement temperature indicates the temperature-dependent localization of in-gap states. (b) 10 K PL spectra of 600 °C Ar/H_2 annealed monolayer MoS_2 with half and full hBN encapsulation. The decrease of LX_N with full hBN encapsulation indicates the suppression of native adsorbates.

In-gap states trap excitons and subsequently increase PL lifetime.[107,120] The PL decay of the LX_D emission at 300 K and 8 K was measured by time-resolved PL spectroscopy (**Figure 4.7**). All PL decay data were fitted with a bi-exponential decay function *ExpDecay 2*: $y = y_0 + A_1 e^{-(x-x_0)/\tau_1} + A_2 e^{-(x-x_0)/\tau_2}$, where A_1 and A_2 are amplitude constants, τ_1 and τ_2 are time constants (see **Table 4.1**). The amplitude-weighted average lifetimes were calculated by:

$\tau_{average} = \frac{A_1\tau_1 + A_2\tau_2}{A_1 + A_2}$. At 300 K (**Figure 4.7**, left), pristine MoS_2 shows an A^-/A exciton lifetime of 70 ps, and the annealed MoS_2 shows a slightly longer A^-/A exciton lifetime of 163 ps due to the increased electron doping, which results in a larger proportion of trions[131]. The LX_D exciton lifetime was measured to be longer at 428 ps. When cooled to 8 K, the A^-/A exciton lifetime was below the detection limit of our instrument. In contrast, the LX_D exciton in annealed MoS_2 was significantly long-lived with a lifetime of 2.44 ns (**Figure 4.7**, right). The long lifetimes of LX_D excitons support the idea that they are localized at defect sites.

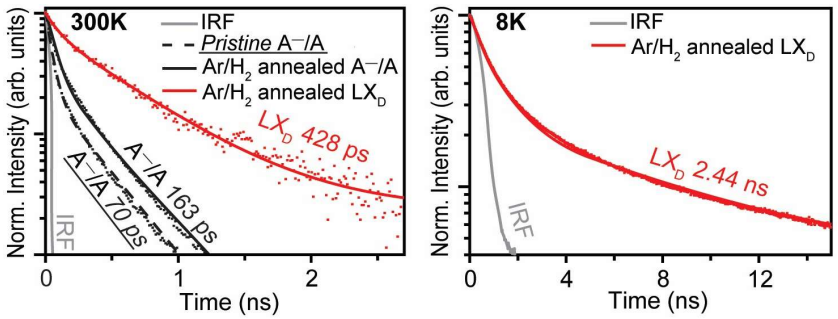

Figure 4.7. PL decay plots for pristine and 600 °C Ar/H_2 annealed monolayer MoS_2 measured at 300 K and 8 K, showing longer lifetimes of localized excitons at in-gap states. The instrument Response Function (IRF) indicates the time resolution of the instrument.

Table 4.1. Time-resolved PL decay fitting parameters at 300 K and 8 K.

Temperature	Sample	PL peak	$\tau_{average}$ (ns)	A_1	τ_1 (ns)	A_2	τ_2 (ns)
300 K	Pristine	A^-/A	0.070	3.005	0.047	0.272	0.322
	Ar/H_2 annealed	A^-/A	0.163	0.687	0.075	0.323	0.351
		LX_D	0.428	0.284	0.094	0.695	0.565
8 K	Pristine	A^-/A	Below the detection limit				
	Ar/H_2 annealed	A^-/A					
		LX_D	2.442	0.757	0.946	0.231	7.348

To probe the distribution of defects in the 600 °C Ar/H_2 annealed MoS_2, intensity maps of LX_D peak were obtained at 300 K and 10 K (**Figure 4.8a**). The LX_D emission is distributed reasonably uniformly over the monolayer. To characterize the consistency of spectral characteristics, 36 points and 37 points were extracted along arrows 1 and 2 from the 10 K intensity map, respectively. All the extracted PL spectra show consistent peak positions (see **Figure 4.8b**).

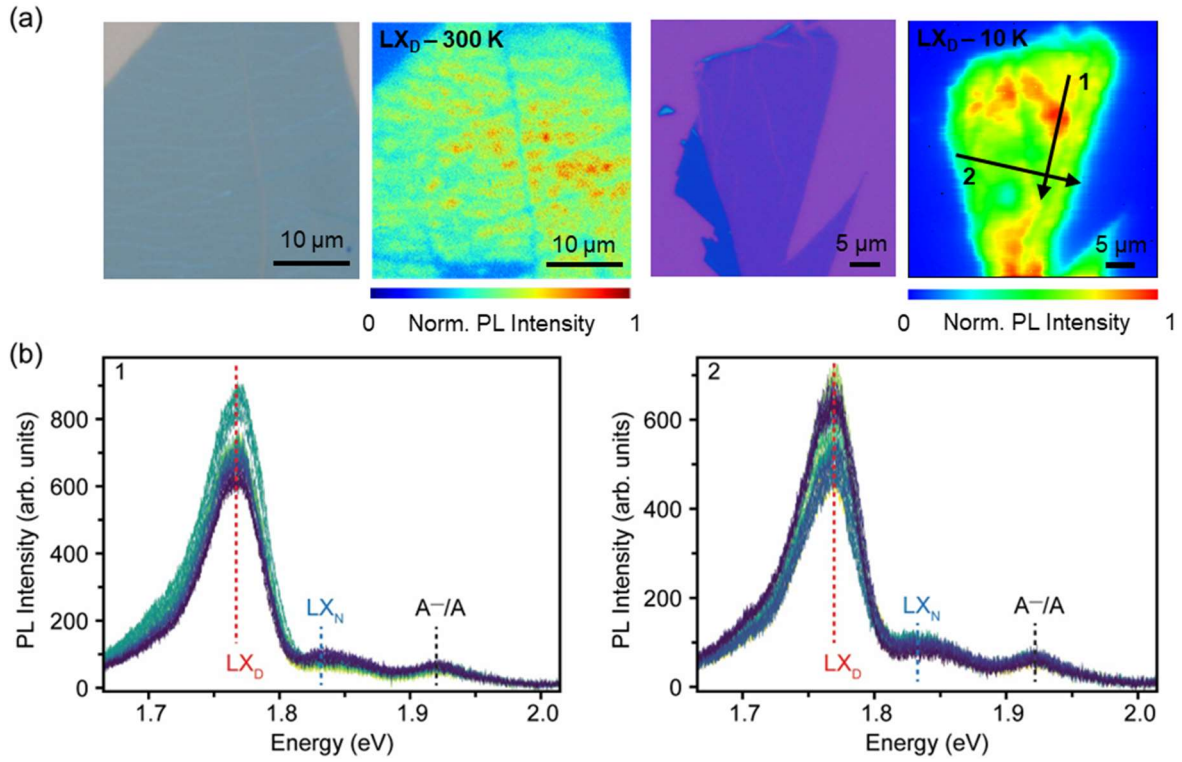

Figure 4.8. Intensity maps of LX_D emission in 600 °C Ar/H_2 annealed monolayer MoS_2. (a) LX_D intensity maps measured at 300 K and 10 K, with corresponding optical microscopy images of target flake, showing the distribution of LX_D emission over the monolayer. 36 points along black arrow 1 and 37 points along black arrow 2 are extracted in 10 K map (upper right). (b) 10 K PL spectra of 36 points along black arrow 1 and 37 points along black arrow 2, showing consistent spectral characteristics at each point.

4.1.4 Defect Generation *vs* Annealing Time

To investigate the evolution of LX_D emission with defect density, I characterized the RT LX_D emission as a function of annealing time at 600 °C (**Figure 4.9**). In pristine MoS_2, in which the

density of sulfur vacancies was ~1.15×10^{13} cm^{-2} (quantified by XPS results in **Section 4.1.1**), the LX_D defect peak was absent. As the annealing time was increased, the LX_D emission rose in intensity, reaching a maximum at 30 min, where the density of defects was ~1.8×10^{14} cm^{-2} (**Figure 4.9a,b**). Increasing the annealing time beyond 30 min results in a decrease in intensity of all spectral features (A^-/A and LX_D emission), which is likely due to gradual material degradation at higher defect densities. A previous work from our group on sulfur vacancy generation using focused He^+ irradiation (0.24 kJ/cm^2) showed that at defect densities >1.5×10^{15} cm^{-2}, the MoS_2 lattice structure is damaged and the PL is quenched[82] – similar to the sample annealed in Ar/H_2 for 3 h (see **Figure 4.9c**). The dependence of the LX_D emission on defect concentration can be well correlated with the LO(*M*) defect mode in Raman spectra, and both reach their maximum intensity at annealing time of 30 min (**Figure 4.9b**). Our results suggest that the strongest RT LX_D emission in 2D MoS_2 occurs at sulfur vacancy concentration of ~1.8×10^{14} cm^{-2}.

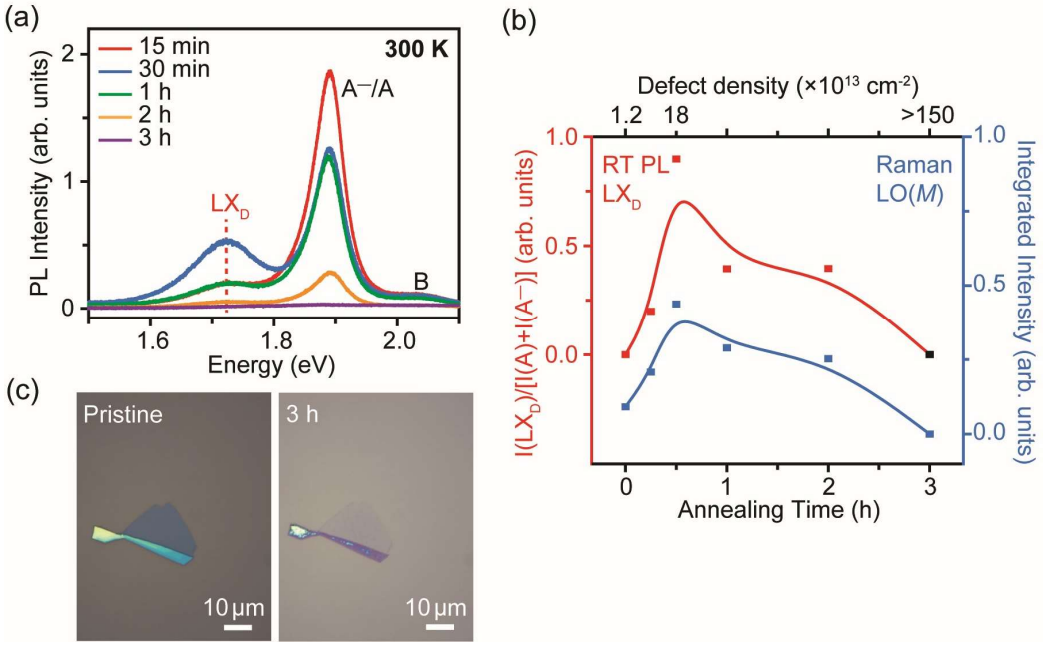

Figure 4.9. Evolution of monolayer MoS_2 with annealing time at 600 °C. (a) RT PL spectra of monolayer MoS_2 with different annealing times. (b) Left: Evolution of integrated RT PL intensity ratio of LX_D emission to the sum of A exciton and A^- trion emission, referred to as $I(LX_D)/[I(A)+I(A^-)]$. Right: Evolution of integrated Raman intensity of LO(M) defect mode. The most intense RT LX_D emission and LO(M) mode are both observed in 30 min annealed MoS_2. (c) Optical microscopy images of pristine and 3 h Ar/H_2 annealed monolayer MoS_2 show clear degradation of monolayer MoS_2 through annealing.

Power-dependent measurements at 10 K were performed to study how the filling of defect states influences PL properties (**Figure 4.10**). As shown in **Figure 4.10a**, pristine MoS_2 shows a linear dependence of the A^-/A peak ($k = 0.97$, see logarithmic plot in **Figure 4.10b**). Similar linear dependence is observed in the A^-/A peak for the 30 min annealed MoS_2 ($k = 0.99$) and 2 h annealed MoS_2 ($k = 0.93$). While LX_D shows a linear dependence in the 30 min annealed MoS_2 ($k = 0.98$), the peak shows a clear sublinear behavior in the 2 h annealed MoS_2 ($k = 0.85$), consistent with previous reports.[104,105] The absence of saturation in the power-dependence of LX_D for the 30 min annealed MoS_2 suggests that this material may host more optically active defect sites for radiative recombination, which possibly requires higher excitation fluence to observe saturation. This in fact allows us to observe a clear PL emission from the defect states at RT, in contrast to previous observations of defect-related emission that have mostly been limited to low temperatures (see **Table 4.2**).

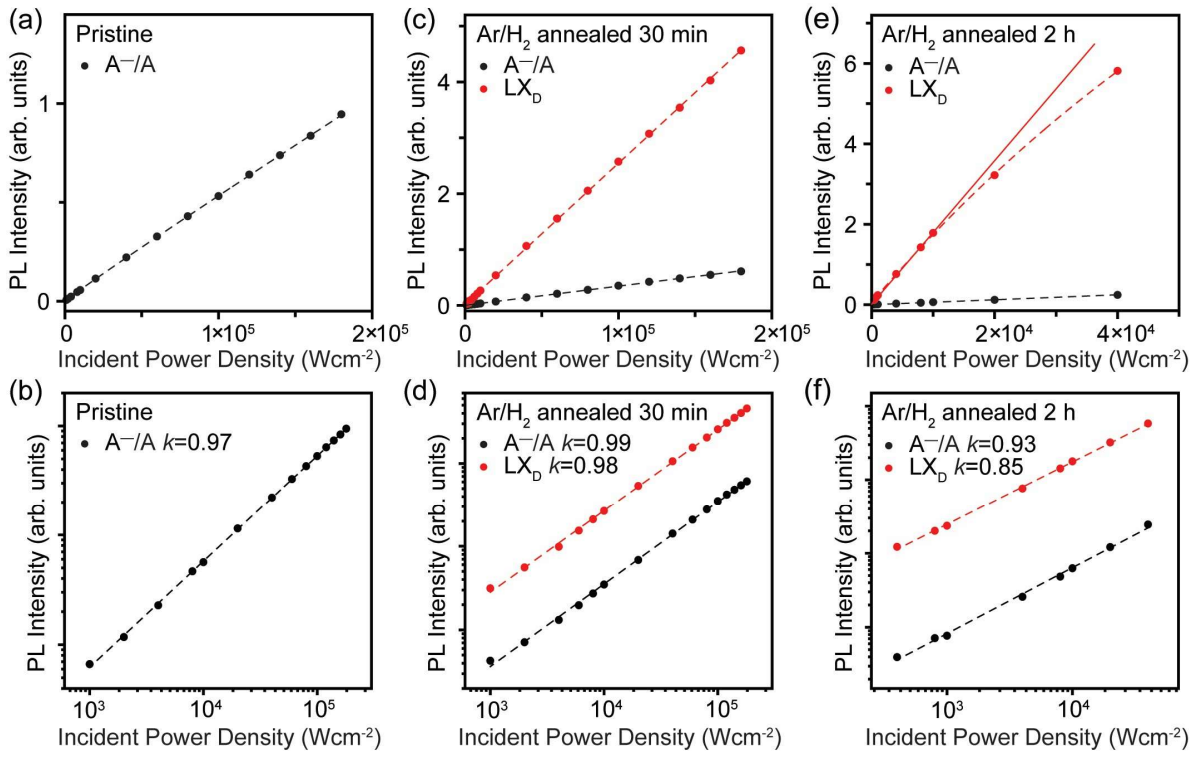

Figure 4.10. Power-dependent PL intensity plots for pristine, 30 min, and 2 h Ar/H_2 annealed monolayer MoS_2 measured at 10 K. (a–c) Power-dependent PL intensity plots. A^-/A shows linear dependence, while LX_D shows linear dependence in 30 min annealed MoS_2 and saturation dependence in 2 h annealed MoS_2. (d–f) Logarithmic plots of (a–c). The power exponent k is obtained from fitting of logarithmic plots, where k = ~1 implies excitonic transition and k < 1 suggests defect-mediated recombination.

Table 4.2. Comparison between our work and published reports on defect-related optical emissions in monolayer TMDs.

Material	Substrate	Treatment	Emission temperature	Reference
MoS_2	AlO_x/nc-C/SiO_2/Si	X-ray irradiation	10 K	*ACS Nano* **2022**, *16*, 20364–20375.[132]
MoS_2	hBN (full encapsulation)	*In-vacuo* annealing	~20 K	*Nat. Commun.* **2021**, *12*, 1–8.[127]
MoS_2	SiO_2/Si	Electron irradiation	No defect PL at RT	*npj 2D Mater. Appl.* **2022**, *6*, 31.[133]
MoS_2	hBN (full encapsulation)	Focused He ion irradiation	15 K	*ACS Photonics* **2021**, *8*, 669–677.[130]
MoS_2	SiO_2/Si, SiN_x	H_2/He annealing	No defect PL at RT	*ACS Nano* **2022**, *16*, 6725–6733.[134]
MoS_2	SiO_2/Si	Electron irradiation	Weak & broad PL at RT	*2D Materials* **2023**, *10*, 035002.[135]
MoS_2	SiO_2/Si	Hydrogen plasma treatment	Weak & broad PL at RT	*Commun. Mater.* **2021**, *2*, 80.[136]
MoS_2	SiO_2/Si	Focused He ion irradiation	Weak & broad PL at RT	*ACS Nano* **2019**, *13*, 9958–9964.[82]
WS_2	hBN (full encapsulation)	Focused He ion irradiation	10 K	*Appl. Phys. Lett.* **2022**, *121*, 183101.[137]
WS_2, WSe_2, MoS_2, $MoSe_2$	hBN (full encapsulation)	Proton irradiation	77 K	*Adv. Opt. Mater.* **2022**, *10*, 2201350.[107]
WS_2	SiO_2/Si	Proton irradiation	4 K	*Nano Lett.* **2023**, *23*, 3754–3761.[138]
WSe_2	hBN (full encapsulation)	Electron irradiation & strain engineering	150 K	*Nat. Commun.* **2021**, *12*, 3585.[139]
MoS_2	SiO_2/Si	Ar/H_2 annealing	RT	This work

4.1.5 Defect Generation in Other TMDs

Having optimized these protocols for MoS_2, I extended them to other TMDs such as WS_2, $MoSe_2$, and WSe_2, as shown in **Figure 4.12**. The monolayer WS_2, $MoSe_2$, and WSe_2 were

mechanically exfoliated from bulk crystals, as described in **Section 3.1**. Similar RT defect peaks were observed in monolayer WS_2, attributed to generation of sulfur vacancies through Ar/H_2 annealing. Unlike MoS_2 that shows clear evolution of A^-/A peak and LX_D peak, WS_2 only shows minor changes in LX_D peak (**Figure 4.11a**). The low intensity of LX_D peak is possibly due to the relatively larger bandgap of WS_2 with respect to MoS_2, with the in-gap states lying much shallower (closer to the CBM). The binding energy of LX_D is ~150 meV in WS_2 that is smaller than in MoS_2 (~180 eV). This may promotes detrapping of excitons. No RT defect peak was observed in $MoSe_2$ and WSe_2 (**Figure 4.11b,c**). This may be due to the fact that Se vacancies are readily passivated by oxygen.[85]

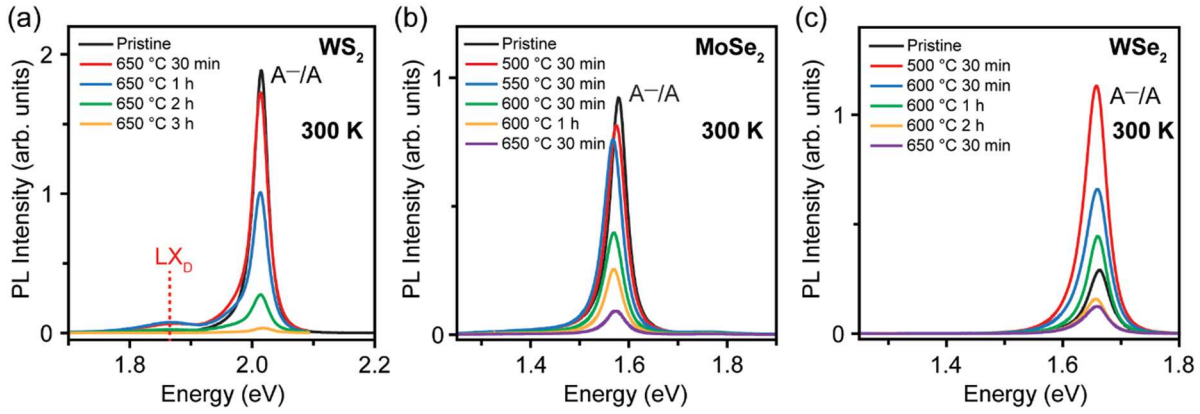

Figure 4.11. Evolution of RT PL spectra in other monolayer TMDs with different annealing temperatures and times. (a) RT PL spectra of monolayer WS_2, showing a RT defect peak LX_D at 1.867 eV. (b–c) RT PL spectra of monolayer $MoSe_2$ and WSe_2. No RT defect peaks are observed in selenide monolayer TMDs.

To characterize the RT defect peak in WS_2, the PL spectrum and power-dependent measurements were taken at 10 K on the sample annealed at 650 °C for 2 h (**Figure 4.12**). The 10 K PL spectrum shows double sets of the exciton/trion peaks (A_1/A^-_1, A_2/A^-_2) with an energy difference of 30 – 40 meV, attributed to inhomogeneous local strain (**Figure 4.12a**).[140] The double sets of exciton/trion peaks exhibit linear excitation power dependence (k = ~1), while the LX_D peak saturates at higher power values (k < 1), suggesting strong localization of excitons at in-gap states (**Figure 4.12b**).

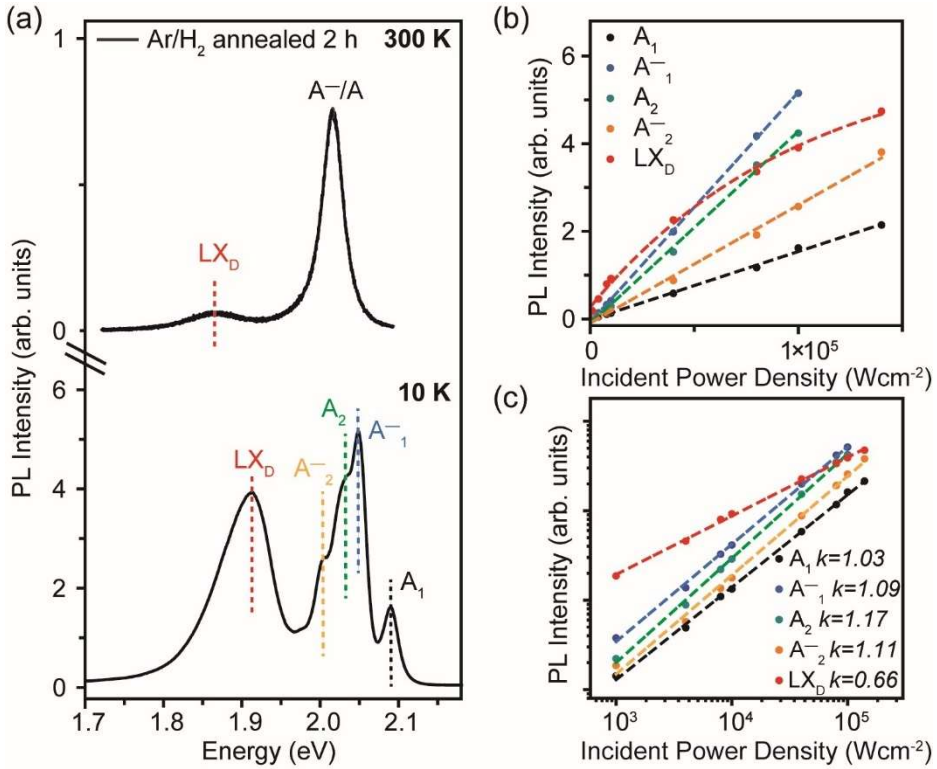

Figure 4.12. PL properties of Ar/H_2 annealed monolayer WS_2 at 650 °C for 2 h. (a) PL spectra of monolayer WS_2, showing a RT defect peak LX_D measured at 300 K and 10 K. (b) Power-dependent PL intensity plots for the annealed monolayer WS_2 measured at 10 K. A_1, A^-_1, A_2, and A^-_2 emissions all show linear dependence, while LX_D shows saturation dependence. (c) Logarithmic plots of (b). The power exponent k is obtained from fitting of logarithmic plots, where k = ~1 implies excitonic transition and k < 1 suggests defect-mediated recombination.

4.2 Defect Passivation in Exfoliated Monolayer MoS_2

The controlled generation of atomic vacancy defects in 2D TMDs can induce single photon emission,[141,142] enhance electro-/photo-catalysis,[143,144] and enable sensing.[145] However, defects typically reduce the performance of electronic devices.[146] Thus, there is interest in passivating them to reduce carrier doping and scattering. In this section, it is demonstrated that sulfur vacancies can be passivated by annealing in sulfur/selenium vapor. The optical properties of defective and passivated samples are compared.

4.2.1 Defect Passivation by Annealing in Sulfur Vapor

The filling of sulfur vacancies was investigated by exposing the defective sample (annealed at 600 °C in Ar/H_2) to sulfur vapor at temperatures ranging from 450 – 600 °C (see **Figure 4.13a**). Room temperature (RT, ~300 K) defect-mediated emission (LX_D) was weakly observed at 450 °C but not ≥500 °C (**Figure 4.13b,c**). Therefore, I chose the 500 °C sulfur passivated sample for synchrotron X-ray photoelectron spectroscopy (XPS) measurements. The XPS spectrum of the Mo 3d doublet shows an absence of the nonstoichiometric MoS_x signal in the defective MoS_2 samples after annealing in sulfur vapor (**Figure 4.14**). The fitting procedures followed the same procedure described in **Section 4.1.1**. No constraint was used for S 1s peaks. The actual stoichiometry after sulfur vapor treatment was found to be $MoS_{2.05}$ – comparable to the pristine MoS_2 samples. However, XPS results reveal an unusual shift of Mo 3d doublet in sulfur-passivated MoS_2 to higher binding energies of 231.2 eV (Mo $3d_{5/2}$) that is 0.2 eV higher than the value in the defective sample, which indicates electron doping.

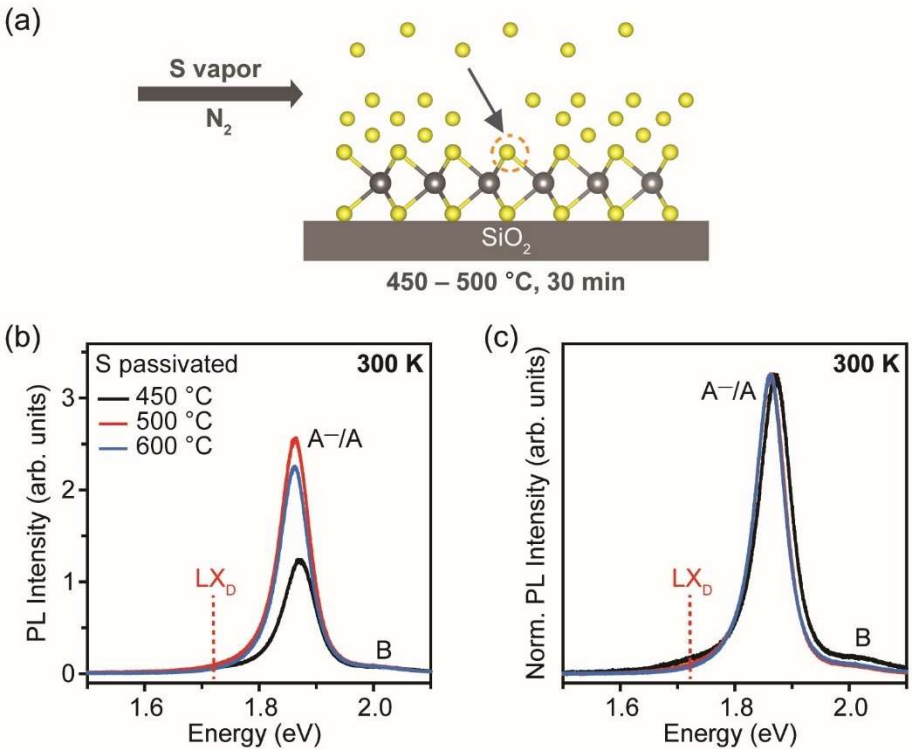

Figure 4.13. Sulfur passivation of Ar/H_2 annealed (600 °C, 30min) monolayer MoS_2 at different temperatures. (a) Schematic of annealing MoS_2 in sulfur vapor. (b) RT PL spectra and (c) their normalized spectra for passivated MoS_2. Weak LX_D peak is observed in the 450 °C sulfur passivated sample but not in samples passivated at 500 and 600 °C.

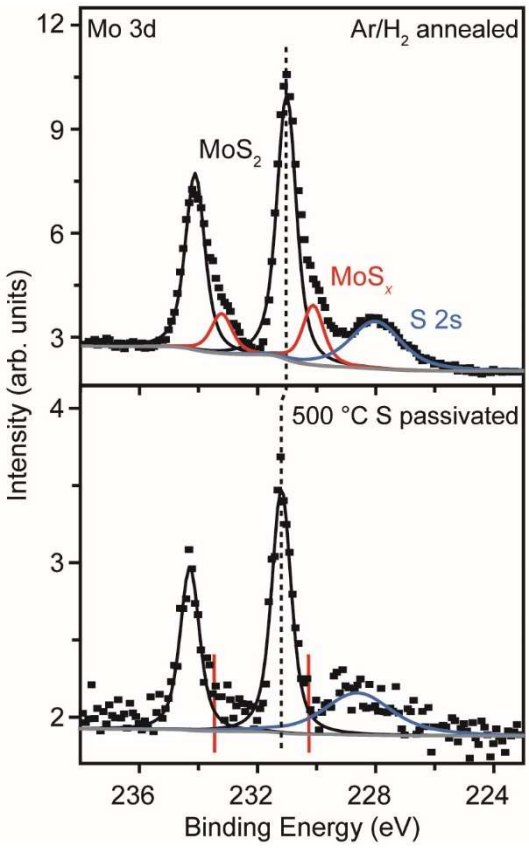

Figure 4.14. Sulfur passivation (500 °C, 30min) of sulfur-deficient monolayer MoS_2. XPS spectra of the Mo 3d core level in Ar/H_2 annealed MoS_2 and sulfur passivated MoS_2. The annealed MoS_2 shows the characteristic Mo 3d doublet from stoichiometric MoS_2 (denoted in black) and S 2s peak (denoted in blue), with a second Mo 3d doublet from nonstoichiometric MoS_x ($0<x<2$, denoted in red). The sulfur passivated MoS_2 shows Mo 3d doublet and S 2s peak from stoichiometric MoS_2 only. The absence of nonstoichiometric MoS_x indicates the passivation of sulfur vacancies.

In photoluminescence (PL) spectra at 300 K and 10 K, LX_D peak is absent for the 500 °C sulfur-passivated sample (**Figure 4.15a**). The reflectance spectrum of the passivated sample shown in **Figure 4.15b** is similar to that of the pristine MoS_2, with the A and B excitonic edges recovered. I noticed an unusual red-shift in the A^-/A peak of the passivated sample. This is attributed to a larger proportion of trions by deconvoluting the RT PL spectrum and calculating the ratio of integrated intensity of A^- trion to A exciton, $I(A^-)/I(A)$. The passivated MoS_2 shows a higher $I(A^-)/I(A)$ ratio of 2.05 than 1.06 in annealed MoS_2 (**Figure 4.15c**). This can be correlated with the XPS peak shift shown in **Figure 4.14**.

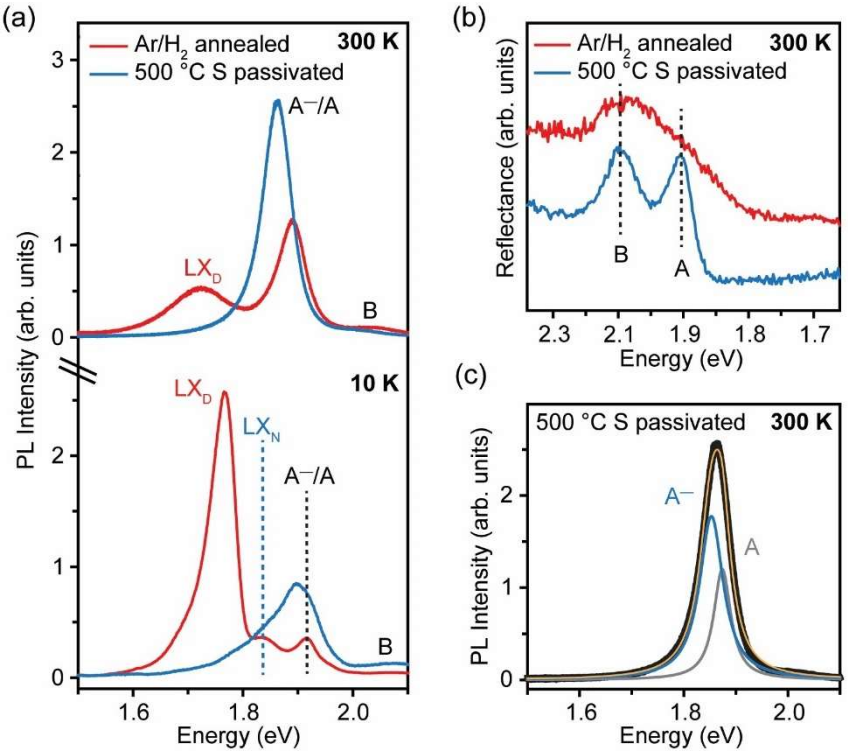

Figure 4.15. Optical properties of sulfur passivated (500 °C, 30min) monolayer MoS_2. (a) PL spectra of Ar/H_2 annealed (600 °C, 30min) and sulfur passivated monolayer MoS_2. The LX_D peak is absent in sulfur-passivated MoS_2 both at 300 K and 10 K. (b) Reflectance spectra of sulfur-passivated MoS_2 restoring to pristine, with the A and B excitonic edges recovered. (c) Deconvoluted RT PL spectra of passivated monolayer MoS_2, fitted with Lorentz peaks. Denotation: A exciton in grey, A^- trion in blue, and cumulative fit curve in yellow.

The electron doping in sulfur passivated MoS_2 is likely due to excessive physisorbed sulfur on the surface of MoS_2 during passivation. To confirm this, XPS S 1s spectra were measured using synchrotron 3 keV hard X-rays. The Ar/H_2 annealed MoS_2 only shows a pristine S 1s peak at 2475.0 eV, whereas passivated MoS_2 shows two peaks (**Figure 4.16**). The second peak with a lower binding energy of 2473.2 eV can be attributed to physisorbed sulfur on the MoS_2 surface.[147]

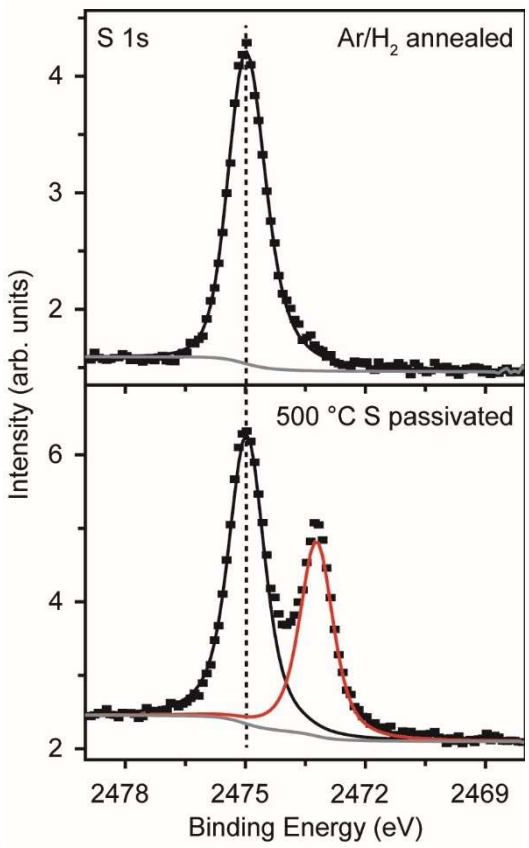

Figure 4.16. XPS spectra of S 1s core level in Ar/H_2 annealed (600 °C, 30min) and sulfur passivated (500 °C, 30min) monolayer MoS_2 probed by synchrotron 3 keV hard X-rays. The Ar/H_2 annealed MoS_2 only shows pristine S 1s peak (denoted in black), whereas the passivated MoS_2 shows two peaks. The second S 1s peak (denoted in red) indicates the physisorbed sulfur on MoS_2 surface.

I sought to remove the weakly-physisorbed sulfur on MoS_2 by annealing the passivated sample at 100 °C for 6 h in a high vacuum of $<10^{-6}$ mbar (see schematic in **Figure 4.17a**). The PL spectra in **Figure 4.17b** show that the A^-/A peak is blue-shifted close to the value measured for pristine MoS_2. Furthermore, the $I(A^-)/I(A)$ ratio decreases to 0.19, indicating that electron doping is largely reduced (**Figure 4.17c**). At 10 K, the defect-mediated LX_D emission reappears, albeit with lower intensity than adsorbates-related LX_N emission, showing that the passivation of in-gap states by annealing in sulfur vapor is a combination of chemical bonding and electron doping. 100 °C was chosen because it is sufficient for subliming unbonded sulfur, but not high enough to create new vacancies.[127]

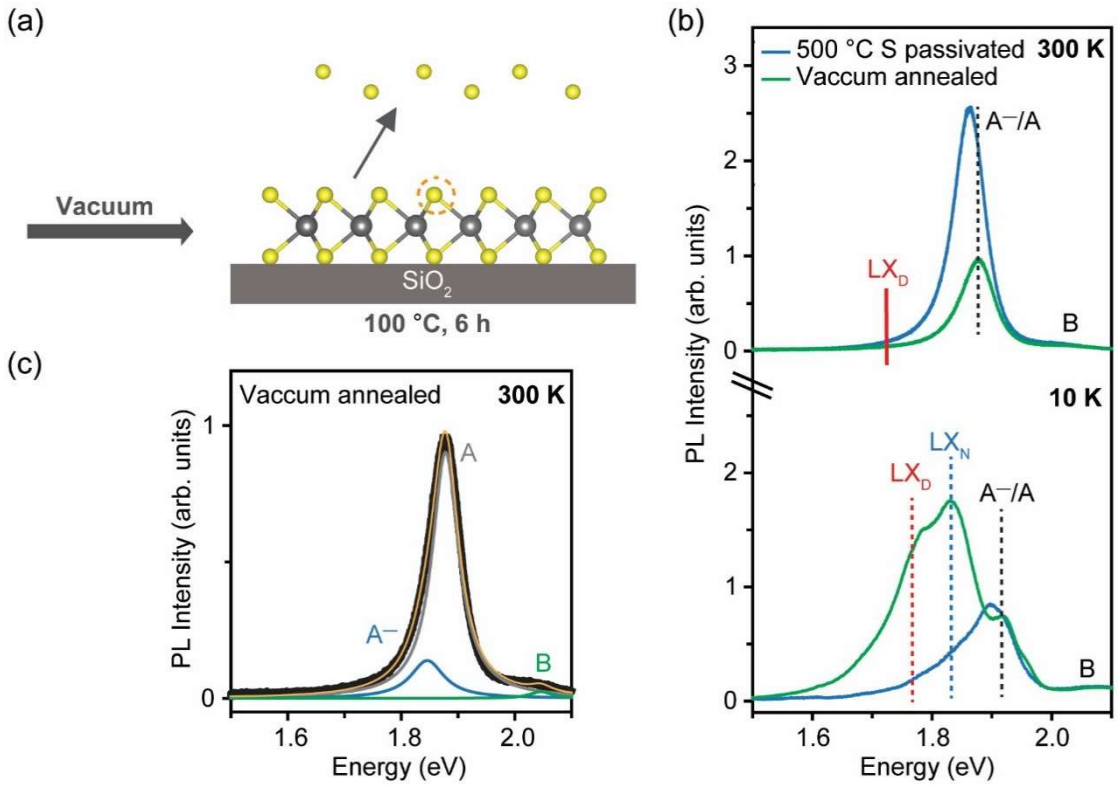

Figure 4.17. Vacuum annealing of sulfur passivated (500 °C, 30min) monolayer MoS_2. (a) Schematic of annealing the sulfur passivated monolayer MoS_2 in a high vacuum of $<10^{-6}$ mbar. (b) PL spectra of sulfur passivated and vacuum annealed monolayer MoS_2. In vacuum annealed MoS_2, the LX_D remains absent at 300 K whereas weakly reappears at 10 K. (c) Deconvoluted RT PL spectra of vacuum annealed monolayer MoS_2, fitted with Lorentz peaks. Denotation: A exciton in grey, A^- trion in blue, and cumulative fit curve in yellow.

To further illustrate the influence of vacuum annealing on the PL properties of MoS_2, pristine MoS_2 was annealed under vacuum (**Figure 4.18**). In pristine MoS_2, no noticeable change of $I(A^-)/I(A)$ is observed at RT by vacuum annealing, indicating no RT-detectable defect generation or electron doping. Therefore, the changes in the PL features of the passivated sample through vacuum annealing are due to the removal of unbonded sulfur. It will be good if synchrotron XPS can be measured on the vacuum annealed sample to confirm the removal of physisorbed sulfur in the future.

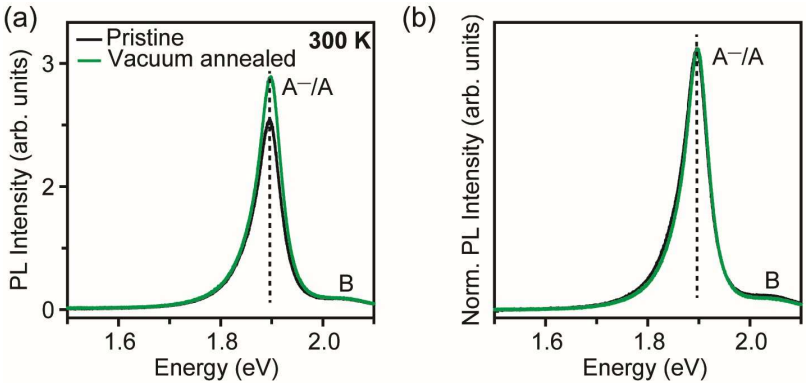

Figure 4.18. Vacuum annealing of pristine monolayer MoS_2. (a) RT PL spectra and (b) their normalized spectra for pristine and vacuum annealed pristine MoS_2, showing no observable changes in the spectral features.

4.2.2 Defect Passivation by Annealing in Selenium Vapor

I also exposed the sulfur-deficient monolayer MoS_2 to selenium to see whether sulfur vacancies can be filled by selenium (see schematic in **Figure 4.19a**). Annealing the sample in selenium vapor at 500 to 600 °C, no new Raman signals were observed, with the LX_D PL peak showing a large decrease at 500 °C and absence at 600 °C (**Figure 4.19b,c**). Above 600 °C, I observed $MoSe_2$ Raman signals at 700 °C and possible Janus MoSSe signals at 800 °C, with significantly weakened in-plane E^1_{2g} and out-of-plane A_{1g} peaks of MoS_2, showing the incorporation of selenium onto MoS_2. Correspondingly, the A^-/A peak of MoS_2 is red-shifted and reaches the largest shift in the 800 °C selenium filled sample. This is attributed to $MoSe_2$ and possible Janus MoSSe that have a narrower bandgap – consistent with previous reports.[148,149]

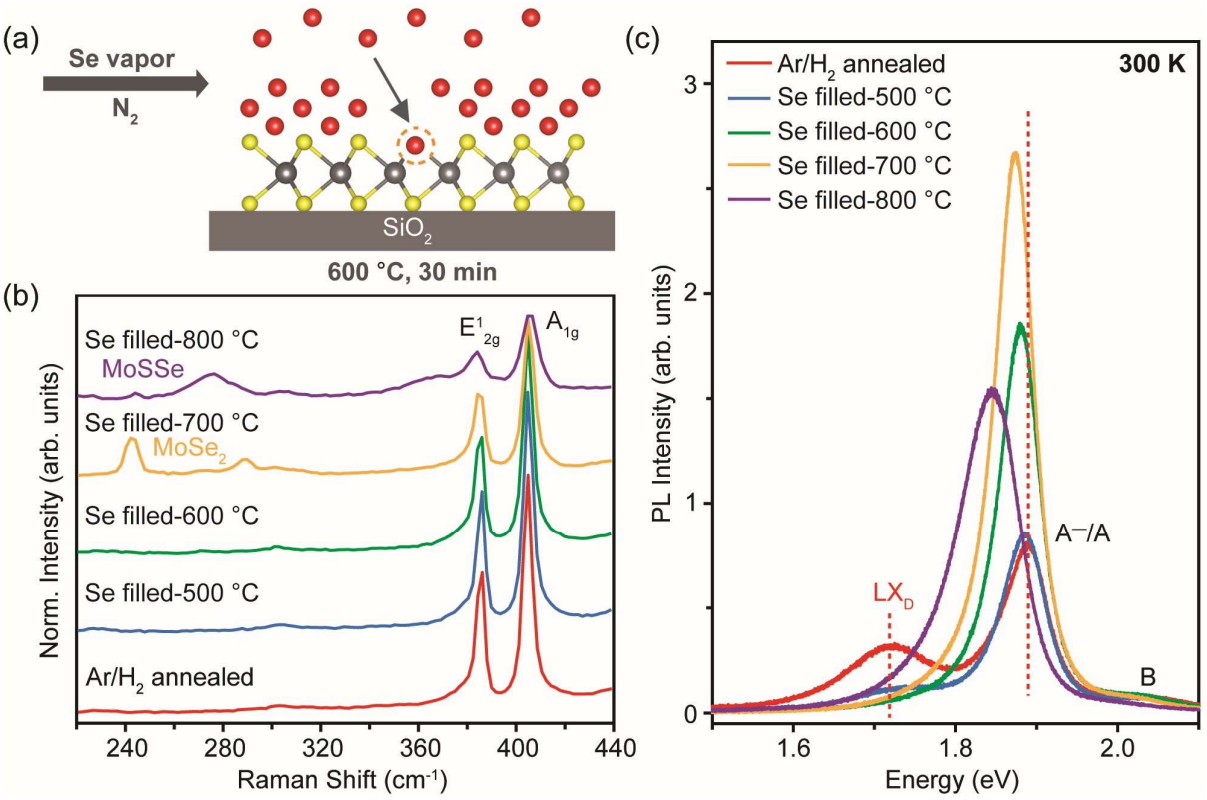

Figure 4.19. Selenium filling of Ar/H₂ annealed (600 °C, 30min) monolayer MoS₂. (a) Schematic of annealing the Ar/H₂ annealed MoS₂ in selenium vapor (600 °C, 30min). (b) Raman spectra of Ar/H₂ annealed MoS₂, and selenium filled MoS₂ through 500 – 800 °C annealing. The new Raman signals from MoSe₂ at 700 °C and MoSSe at 800 °C indicate the formation of Mo–Se bond. (c) RT PL spectra of Ar/H₂ annealed and selenium filled MoS₂. Above 600 °C, the LX$_D$ peak remains absent. The red shift of A⁻/A peak is attributed to the formation of MoSe₂ and possible MoSSe with a narrower bandgap.

The unusual electron doping shown in XPS spectra and RT PL spectra of sulfur passivated MoS_2 leads to the identification of physisorbed sulfur. Similarly, the larger proportion of trions in the RT spectra of selenium filled MoS_2 could be attributed to extra electron doping induced by physisorbed selenium. Thus, the vacuum annealing method was adapted to remove the physisorbed selenium (see schematic in **Figure 4.20a**) by raising the annealing temperature to 200 °C because selenium vaporizes at a higher temperature than sulfur. When I annealed the 600 °C selenium filled MoS_2 in a high vacuum of $<10^{-6}$ mbar, the LX_D peak remained absent at RT while appearing at 10 K with an intensity comparable to the A^-/A peak (**Figure 4.20b**). The decrease of the proportion of A^- peak suggests the removal of physisorbed selenium (**Figure 4.20c**).

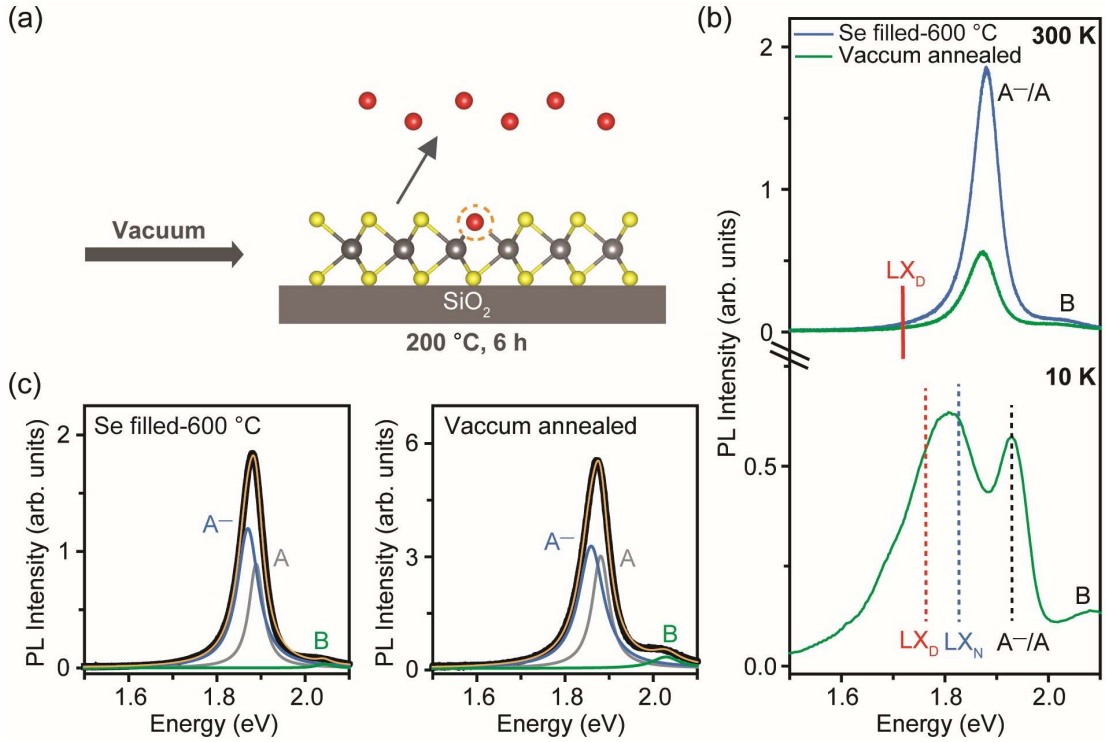

Figure 4.20. Vacuum annealing of 600 °C selenium filled monolayer MoS_2. (a) Schematic of annealing the selenium filled MoS_2 in a high vacuum of $<10^{-6}$ mbar. (b) PL spectra of selenium filled and vacuum annealed monolayer MoS_2 at 300 K and 10 K. The LX_D peak is absent in selenium filled MoS_2 at 300 K. In vacuum annealed MoS_2, the LX_D peak remains absent at 300 K whereas appears at 10 K. (c) Deconvoluted RT PL spectra of (left) selenium filled and (right) vacuum annealed MoS_2, fitted with Lorentz peaks. Denotation: A exciton in grey, A^- trion in blue, B exciton in green, and cumulative fit curve in yellow.

To understand whether the formation of $MoSe_2$ and MoSSe is related to the density of sulfur vacancies, selenium vapor was supplied to highly defective MoS_2 (annealed at 600 °C for 2 h in Ar/H_2). As shown in **Figure 4.21a**, $MoSe_2$ Raman signals are observed at 600 °C while MoSSe signals appear at 700 °C. The suppression of LX_D peak in passivated samples at both 300 K and 10 K supports the filling of sulfur vacancies by selenium (**Figure 4.21b,c**).

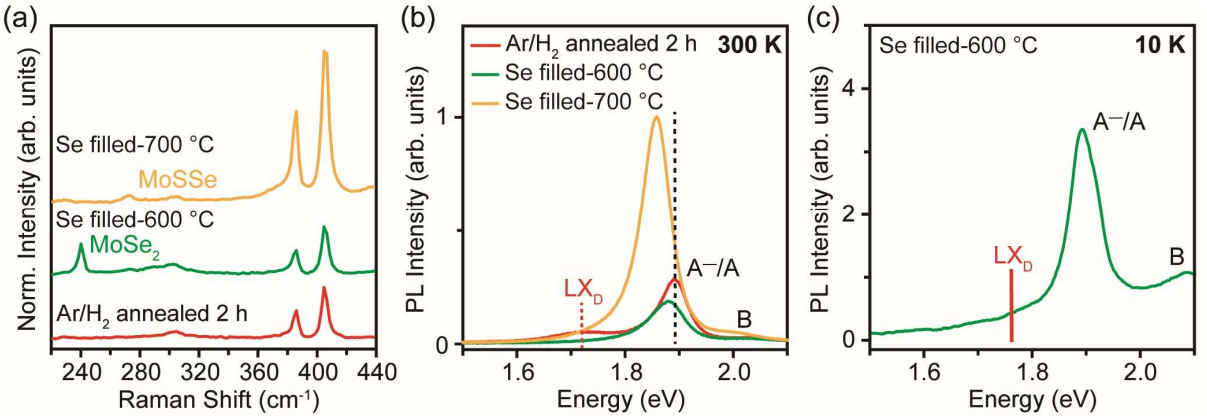

Figure 4.21. Selenium filling of Ar/H_2 annealed (600 °C, 2 h) monolayer MoS_2. (a) Raman spectra of Ar/H_2 annealed MoS_2, and selenium filled MoS_2 through 600 – 700 °C annealing, showing $MoSe_2$ signals at 600 °C and possible MoSSe signals at 700 °C. (b) RT PL spectra of Ar/H_2 annealed and selenium filled MoS_2, and (c) 10 K PL spectrum of selenium filled MoS_2, showing an absence of the LX_D peak both at 300 K and 10 K.

4.3 Defect Generation & Passivation in CVD-Grown Monolayer MoS_2

I also explored whether it was possible to controllably engineer defects in CVD-grown monolayer MoS_2 (see **Figure 4.22a**). With respect to pristine MoS_2, the dominant PL peak was red-shifted in annealed samples through 550 – 600 °C Ar/H_2 annealing. Despite the broadening of PL peaks that makes it difficult to deconvolute the spectra, I found that the electronic bandgap remained unchanged using B exciton peaks. Thus, the PL peak shift is likely due to exciton trapping at in-gap states. Compared to mechanically exfoliated samples that show an optimum defect-mediated emission at 600 °C, the strongest low-energy shoulder in CVD samples was observed at 550 °C due to higher starting defect density. As discussed in **Section 3.1**, CVD samples typically contain more sulfur vacancies than mechanically exfoliated samples. To achieve an equivalent density of sulfur vacancies for optimal defect-related emission, a lower annealing temperature is required for CVD-grown MoS_2 in our experiments, as fewer defects need to be generated. Then the defective MoS_2 (annealed at 550 °C for 30 min in Ar/H_2) was exposed to sulfur vapor at 500 °C, showing an absence of RT LX_D peak which remained through vacuum annealing (**Figure 4.22b**).

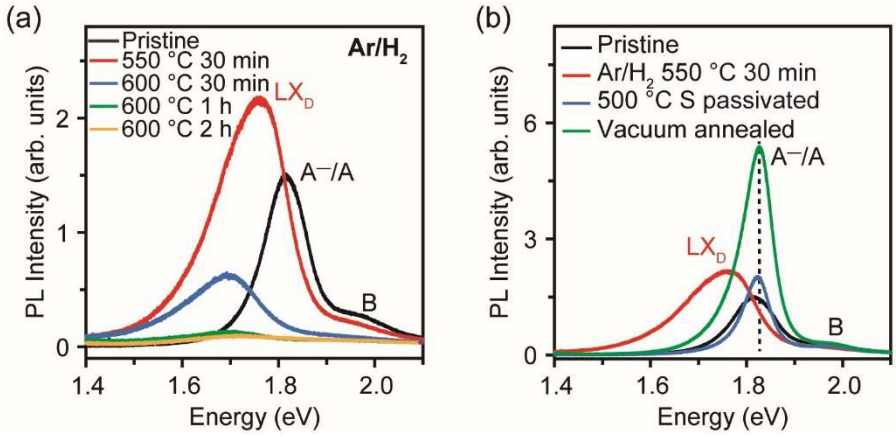

Figure 4.22. Defect generation and passivation in CVD-grown monolayer MoS_2 (a) RT PL spectra of MoS_2 with sulfur vacancies generated at different Ar/H_2 annealing temperatures and times. The PL red-shift in the Ar/H_2 annealed MoS_2 indicates defect generation. (b) RT PL spectra of Ar/H_2 annealed MoS_2 (550 °C, 30min) passivated by annealing in sulfur vapor by post annealed in vacuum. The restoration of PL suggests the passivation of sulfur vacancies.

4.4 Summary

It has been demonstrated that by controlling the temperature, duration, and environment of thermal annealing, it is possible to generate sulfur vacancies in 2D MoS_2. The sulfur vacancies induce in-gap electronic states and lead to RT localized exciton emission. Time-resolved PL measurements reveal that the defect-mediated emission shows longer lifetime than band edge excitons, both at room and low temperatures. Using XPS measurements, I have identified that at sulfur vacancy densities of ~1.8×10^{14} cm^{-2}, the RT defect-mediated emission is the most intense. This annealing method was extended to 2D WS_2 in which similar RT defect-mediated emission was observed, but not in 2D $MoSe_2$ and WSe_2. I also show that the sulfur vacancies can be passivated by annealing in sulfur vapor. At annealing temperatures ≥500 °C, the defect-mediated emission is fully suppressed both at RT and 10 K. The passivation via chemical bonding is confirmed by XPS that shows the absence of non-stoichiometric Mo 3d doublet. The physisorbed sulfur is identified by a second S 1s peak in XPS. The generated sulfur vacancies can also be filled by selenium at annealing temperatures ≥600 °C in selenium vapor.

Chapter 5 Substrate Effects on Photoluminescence from Sulfur Vacancies in Monolayer MoS_2

2D semiconducting TMDs feature reduced dielectric screening and enhanced Coulomb interactions. Therefore, monolayer TMDs are easily electronically influenced by the substrates. Typical substrate effects include strain[101,150,151], dielectric screening[34,152,153], and charge transfer[154,155]. In this chapter, it is shown that photoluminescence (PL) from sulfur vacancies is sensitive to doping from surface states of dielectrics. In this chapter, I designed the experiments, synthesized samples, and conducted Raman and PL measurements at RT. Atomic layer deposition (ALD) of 50 nm HfO_2 on Si substrates was done by Dr. Soumya Sarkar. Low-temperature PL spectra, and PL mapping were measured by Dr. Zhepeng Zhang. Field-effect transistors (FETs) for gate-dependent PL measurements were fabricated by Dr. Ye Wang. Synchrotron XPS was done by Dr. Yan Wang and Mr. Han Yan.

5.1 Annealing of MoS_2 on HfO_2

To investigate the influence of substrate on defect-mediated PL, I performed annealing of MoS_2 on HfO_2. The 50 nm HfO_2 films were grown on doped silicon substrates using thermal ALD in a Veeco Fiji G2 reactor. A metal alkylamide hafnium precursor tetrakis (dimethyl amido)hafnium (TDMAH) was used as the Hf source and deionized water was the oxygen source. The reaction has been reported as follows[156]: $Hf[(CH_3)_2N]_4 + 2H_2O \rightarrow HfO_2 + 4HN(CH_3)_2$. The TMDAH precursor was heated to 75 °C during the growth. The films were grown at a substrate temperature of 200 °C. At this temperature, the growth rate was estimated to be 1.2 Å/cycle. TDMAH and H_2O precursors were pulsed/purged per cycle for 0.25 s /10 s and 0.06 s /10 s, respectively. 60 sccm Ar was used as the carrier gas. Monolayer MoS_2 was mechanically exfoliated on HfO_2 (50 nm)/Si and then annealed in an Ar/H_2 (95 *vol.*%/5 *vol.*%) atmosphere at 600 °C for 30 min – similar to samples on SiO_2 in **Chapter 4**. Room temperature (RT, ~300 K) PL spectra of pristine and annealed MoS_2 on HfO_2 are shown in **Figure 5.1a**. All the PL spectra show a broad background from annealed HfO_2 substrate, as indicated by the brown curve in **Figure 5.1a**. The PL signals from MoS_2 were extracted by subtracting the background substrate signal as shown in **Figure 5.1b**. Surprisingly, the defect-mediated emission peak (LX_D) is absent in the annealed MoS_2 on HfO_2 samples and only the A^-/A and B exciton peaks are present (**Figure 5.1b**).

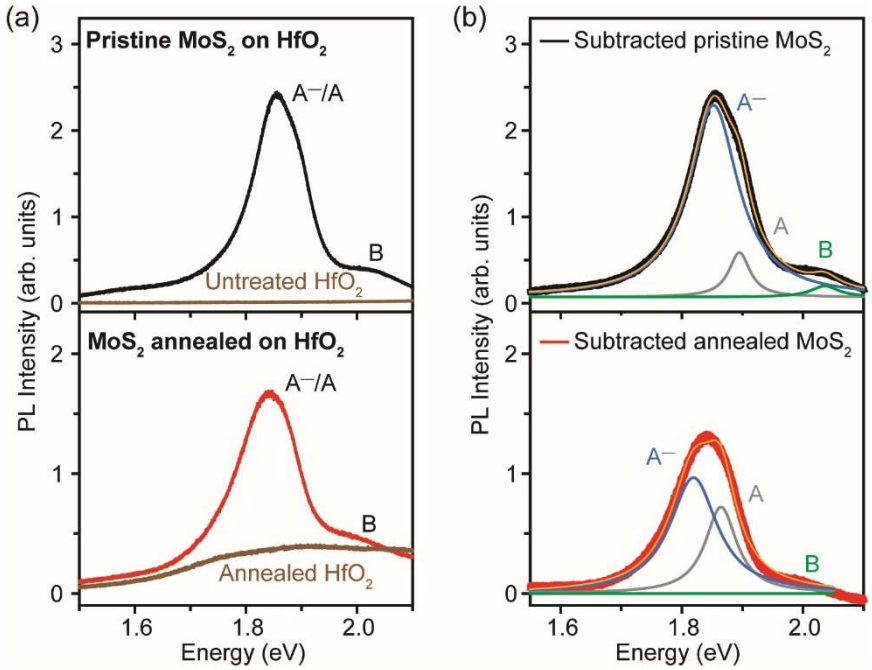

Figure 5.1. Ar/H_2 annealing (600 °C, 30 min) of monolayer MoS_2 on HfO_2. (a) RT PL spectra of pristine MoS_2 on HfO_2 (top panel) and annealed MoS_2 (bottom panel). The background PL signals from HfO_2 substrate are shown in brown. (b) Background-subtracted RT PL spectra of pristine and annealed MoS_2, deconvoluted with Lorentz peaks. Denotation: A exciton in grey, A^- trion in blue, B exciton in green, and cumulative fit curve in yellow. Only the A^-/A peak and B exciton peaks are present in both pristine and annealed MoS_2.

The PL spectra of MoS_2 annealed on HfO_2 measured as a function of temperature ranging from 300 K to 10 K are shown in **Figure 5.2a**. It can be seen that the spectra show A^-/A peaks along with the broad background from the substrate at all temperatures. **Figure 5.2b** shows that the A^-/A peak dominates over B exciton peak after subtracting the contributions from HfO_2 in the 10 K PL spectrum. The intensity of A^-/A peak is linearly dependent on excitation laser fluence with power exponent $k = 0.96$, suggesting that A^-/A peak is excitonic emission that is typically associated with $k = \sim 1$ (**Figure 5.3**).[105] It is worth noting that the PL features in annealed MoS_2 on HfO_2 were red-shifted by ~30 meV both at RT and 10 K compared to pristine MoS_2. The origin of this shift is unclear but it could be due to strain from thermal mismatch or due to crystallization of HfO_2.

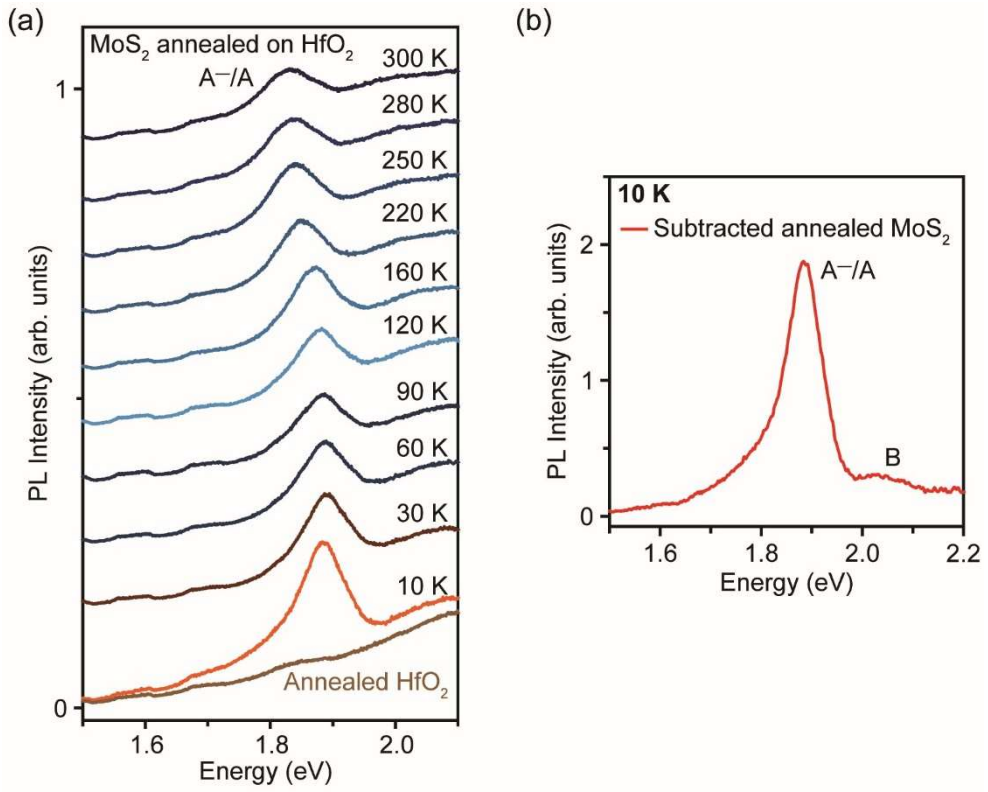

Figure 5.2. Low-temperature PL measurement of monolayer MoS_2 annealed on HfO_2. (a) Temperature-dependent PL spectra showing dominant A^-/A peak. Background PL signals (brown) from HfO_2 substrate are also shown. (b) Background-subtracted 10 K PL spectrum of MoS_2 annealed on HfO_2, showing dominant A^-/A and B peaks only.

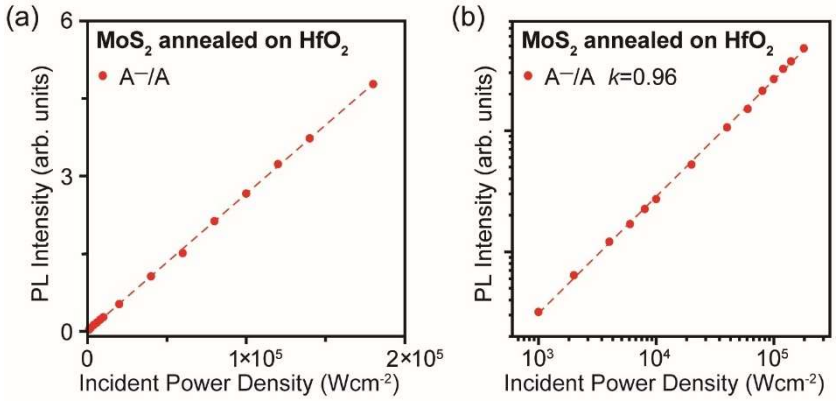

Figure 5.3. Power-dependent PL intensity plots for MoS_2 annealed on HfO_2 measured at 10 K. (a) Power-dependent PL intensity plots. A^-/A shows linear dependence. (b) Logarithmic plot of (a), showing a power exponent k of 0.96 that corresponds to excitonic transition.

To understand the absence of LX_D emission peak, changes in HfO_2 due to Ar/H_2 annealing were investigated by X-ray diffraction (XRD), shown in **Figure 5.4**. The untreated HfO_2 shows signals from underlying crystalline Si (111) only because it is amorphous. The Ar/H_2 annealed HfO_2 shows additional peaks that are attributed to the monoclinic phase of crystalline HfO_2.[157] Here XRD was conducted on HfO_2 substrates only, thus there were no signals from MoS_2.

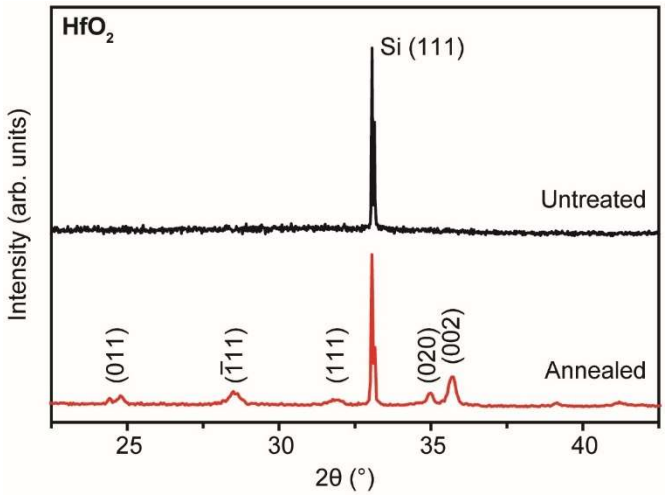

Figure 5.4. XRD patterns of untreated and Ar/H_2 annealed (600 °C, 30 min) HfO_2. The untreated HfO_2 shows sharp peaks of Si (111) from the underlying Si substrate. The annealed HfO_2 shows additional peaks that are attributed to the monoclinic phase of crystalline HfO_2.

To understand the red-shift of PL and absence of LX_D peak in samples of MoS_2 annealed on HfO_2, I carried out some control experiments. First, I annealed the HfO_2 in Ar/H_2 for 30 mins. Then we transferred MoS_2 on the annealed HfO_2. The PL from this sample is labeled as pristine MoS_2 in **Figure 5.5a**. The subtracted PL spectrum of pristine MoS_2 on annealed HfO_2 shows A^-/A peak at ~1.89 eV. Then I reannealed the HfO_2 with MoS_2 on top. The PL from HfO_2 after the second annealing increases slightly (green curve in **Figure 5.5a**). The subtracted PL spectrum of annealed MoS_2 on 2^{nd} annealed HfO_2 MoS_2 shows similar A^-/A peak to annealed MoS_2 (**Figure 5.5b**). These results show that the red-shift of PL features is not prominent in any of the samples, while the LX_D peak remains absent. Two possible reasons for the absence of the LX_D peak can be: sulfur vacancies are not created in the MoS_2 when annealed on HfO_2 or HfO_2 somehow suppresses emission from vacancy defects.

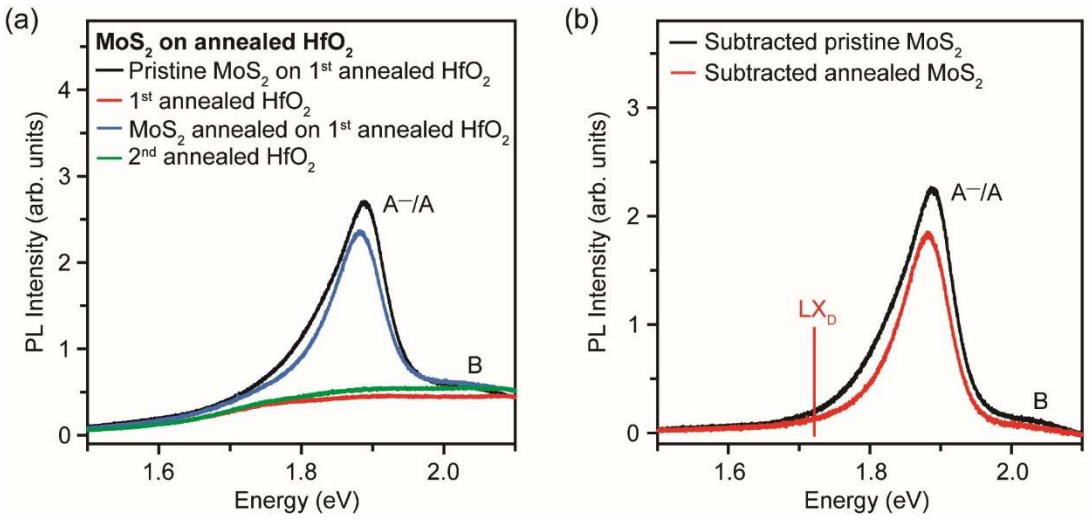

Figure 5.5. RT PL spectra of monolayer MoS_2 on annealed HfO_2. (a) RT PL spectra of pristine MoS_2 on 1st annealed HfO_2 and MoS_2 annealed on 1st annealed HfO_2. (b) Background-subtracted RT PL spectra of pristine, and Ar/H_2 annealed MoS_2, showing the absence of LX_D peak.

5.2 Annealing of MoS_2 on hBN

I then checked whether LX_D was substrate-dependent by measuring the PL of MoS_2 on ~27 nm hBN on SiO_2 (300 nm)/Si annealed in Ar/H_2 for 30 mins (**Figure 5.6a–c**). The hBN flakes were directly exfoliated from bulk crystals onto SiO_2 (300 nm)/Si substrates. The thickness of hBN was measured by atomic force microscopy (AFM) and the target flake was selected accordingly. The monolayer MoS_2 was mechanically exfoliated from bulk crystals onto PDMS and transferred onto selected hBN flake, following the procedure described in **Section 3.1**. Like HfO_2, the hBN shows some background PL as indicated by brown curves in **Figure 5.6c**. A clear LX_D is present in the sample annealed on hBN on SiO_2 as indicated by the background-subtracted spectrum in **Figure 5.6d**.

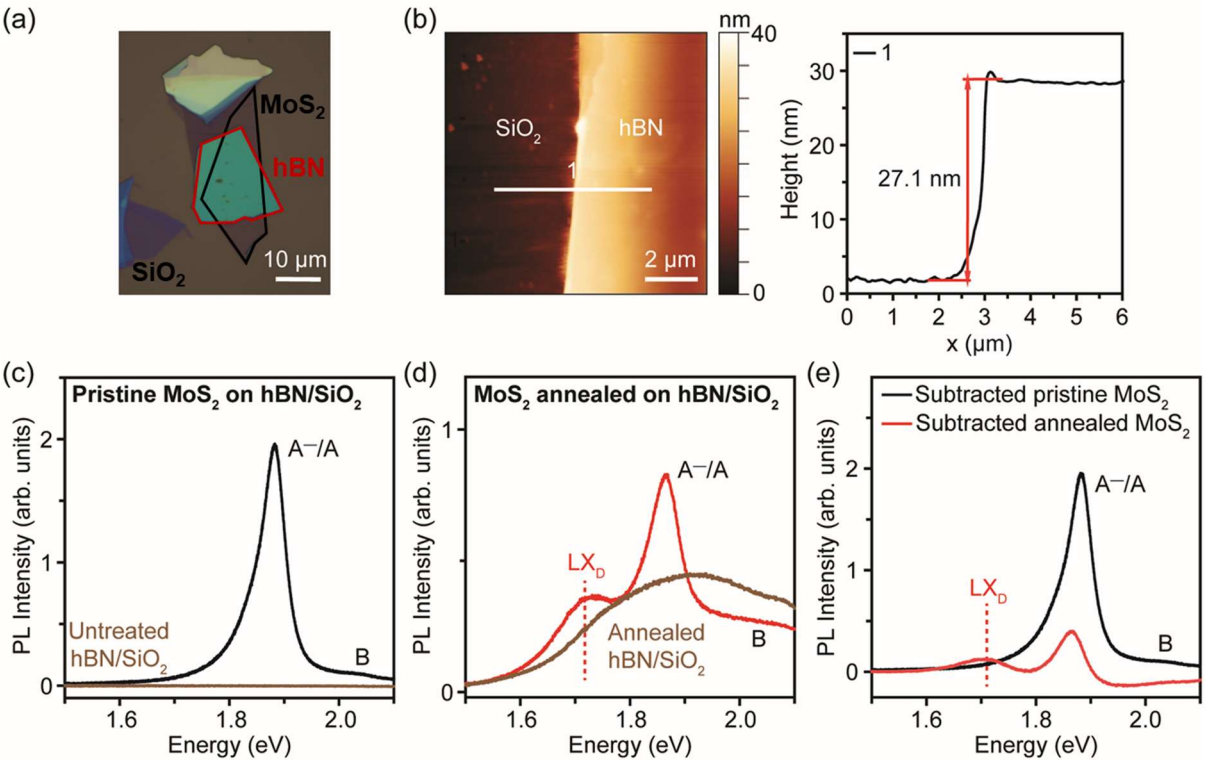

Figure 5.6. Ar/H_2 annealing (600 °C, 30 min) of monolayer MoS_2 on hBN on SiO_2. (a) Optical microscopy image of monolayer MoS_2 on hBN on SiO_2. (b) AFM image (left) and height profile (right) of hBN on SiO_2. (c–d) RT PL spectra of (c) pristine and (d) annealed MoS_2/hBN, with background signals from hBN (brown). LX_D emission in annealed MoS_2 is accompanied by stronger emission from hBN. (e) Background-subtracted RT PL spectra of pristine and annealed MoS_2, showing the LX_D peak.

I have also measured the PL of MoS_2 annealed on hBN on HfO_2. The results of this study are shown in **Figure 5.7**. Surprisingly, the results are different from MoS_2 on hBN on SiO_2. It can be seen from **Figure 5.7c–e** that the LX_D peak is absent in all RT measurements for both pristine and annealed samples.

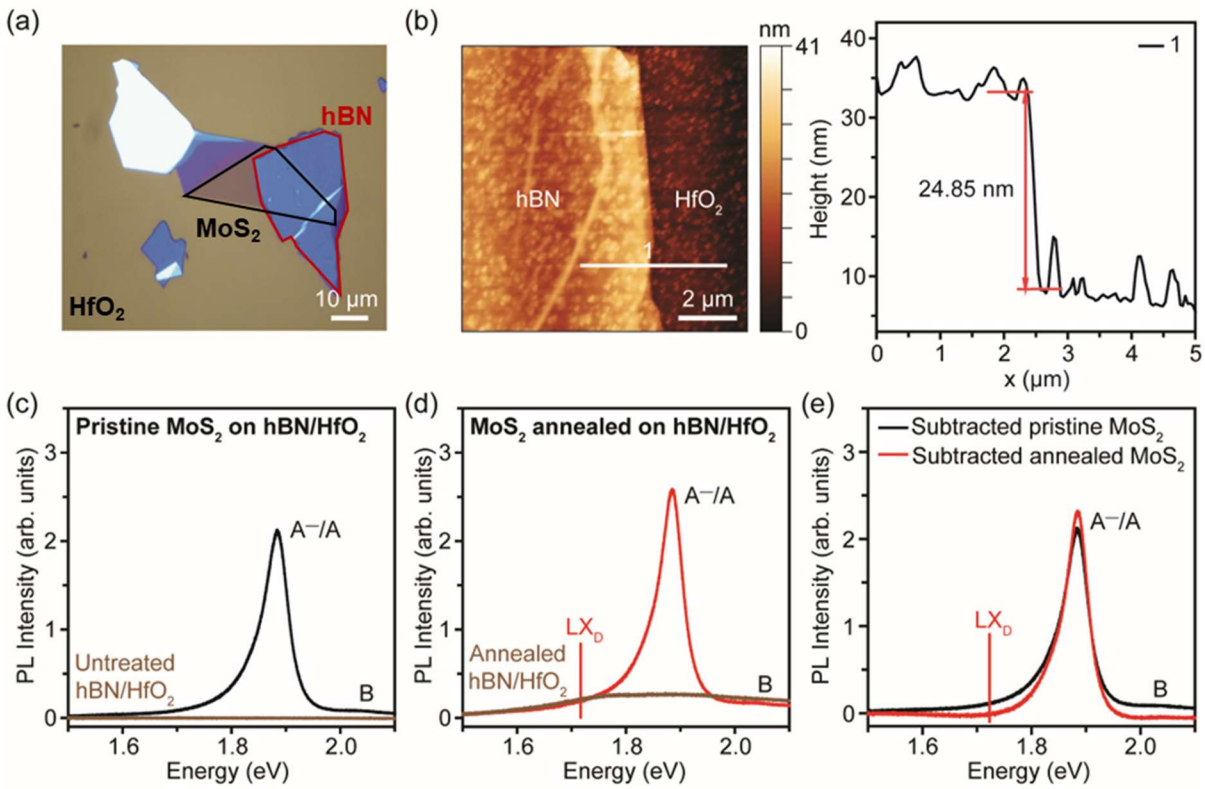

Figure 5.7. Ar/H₂ annealing (600 °C, 30 min) of monolayer MoS_2 on hBN/HfO_2. (a) Optical microscopy image of monolayer MoS_2 on hBN/HfO_2. (b) AFM image (left) and height profile (right) of hBN on HfO_2. (c–d) RT PL spectra of (c) pristine, and (d) annealed MoS_2 on hBN/HfO_2, with background signals from hBN/HfO_2 (brown). The LX_D is absent in both pristine and annealed MoS_2 on hBN/HfO_2. (e) Subtracted RT PL spectra of pristine and annealed MoS_2, showing an absence of LX_D peak.

The PL from this annealed sample was also measured at 10 K (**Figure 5.8**). The optical microscope image in **Figure 5.8a** shows that MoS_2 is partially located on HfO_2 and hBN. In **Figure 5.8b**, the PL intensity maps of the A^-/A peak and LX_D peaks are shown, respectively. The A^-/A emission was observed in both MoS_2 on hBN/HfO_2 and MoS_2 on HfO_2 whereas LX_D emission was only observed on MoS_2 on hBN/HfO_2. Further, the spectrum from MoS_2 on hBN/HfO_2 (indicated by red star) and another spectrum from MoS_2 on HfO_2 (green star) were extracted. The LX_D peak is clearly visible for MoS_2 on hBN/HfO_2 region but is suppressed in MoS_2 on HfO_2 region (**Figure 5.8c)**. The observation of LX_D peak at RT on MoS_2 that is deposited on hBN on SiO_2 is likely due to strong optical interference and reflection at the Si/SiO_2 interface which leads to enhancement in signals compared to hBN on HfO_2.

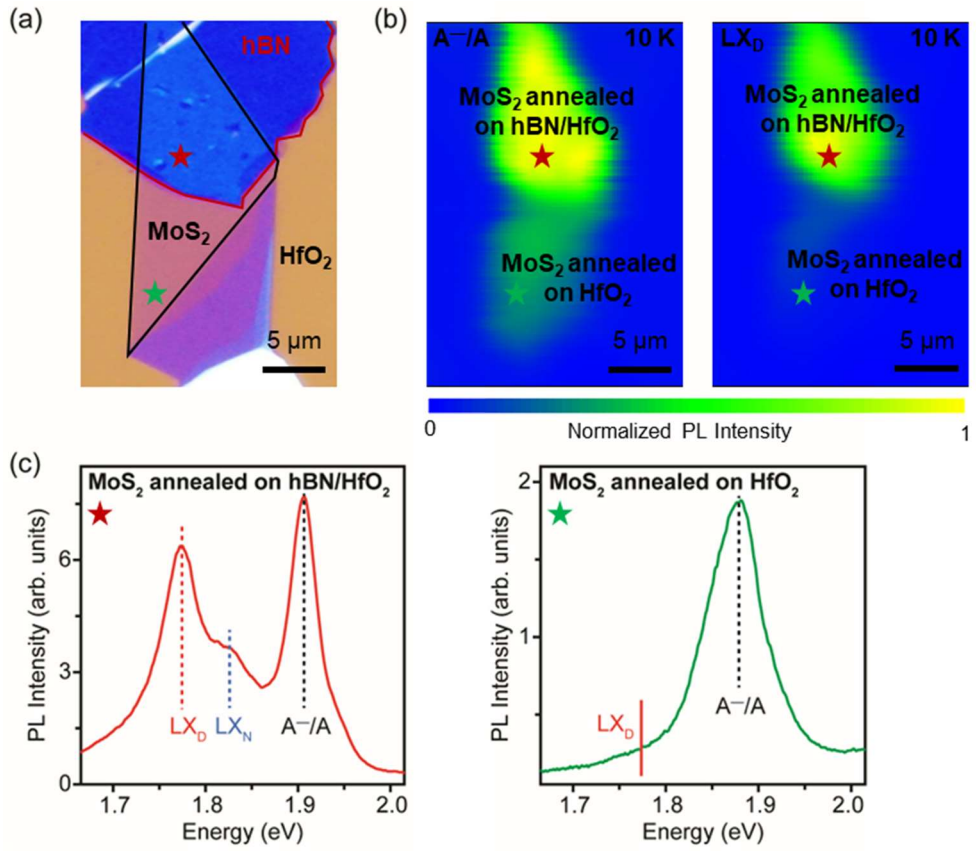

Figure 5.8. Intensity maps of A^-/A and LX_D emission in Ar/H_2 annealed (600 °C, 30 min) monolayer MoS_2 on hBN/HfO_2 and MoS_2 on HfO_2. (a) Optical microscopy image of MoS_2 on hBN/HfO_2 and MoS_2 on HfO_2. (b) Corresponding A^-/A and LX_D intensity maps measured at 10 K. A^-/A emission is distributed across MoS_2 on hBN/HfO_2 and MoS_2 on HfO_2 [left panel in (b)], whereas LX_D emission is only observed in MoS_2 on hBN/HfO_2 [right panel in (b)]. PL from two points is extracted from regions indicated by red and green stars in (a). (c) 10 K PL spectra, showing LX_D peak in MoS_2 on hBN/HfO_2 but not in MoS_2 on HfO_2.

5.3 Transfer of Defective MoS_2 from SiO_2 to SiO_2

In the annealing experiments, two processes may occur: (i) creation of sulfur vacancies in MoS_2; (ii) annealing of SiO_2 or HfO_2 substrates that can change the substrate or the interface between MoS_2 and the oxide. To check the contributions of these possibilities, I performed some control experiments. First, I annealed the MoS_2 on SiO_2 in Ar/H_2 at 600 °C for 30 mins and confirmed the presence of the LX_D peak. I then mechanically transferred the defective MoS_2 onto a different SiO_2 substrate. I found that the MoS_2 adhered strongly to SiO_2 after annealing. Because of this, I adopted the poly(bisphenol A carbonate) (PC) transfer method

(see **Section 3.4** for details). This was used to transfer annealed monolayer MoS_2 onto SiO_2 (see schematic in **Figure 5.9a**). Raman spectrum of transferred MoS_2 showed the LO(*M*) defect mode (similar to results in **Chapter 4**), shown in in **Figure 5.9b**. However, the LX_D peak was absent when the defective MoS_2 was transferred onto a new SiO_2 substrate (**Figure 5.9c**, black curve). These results suggest that annealing of SiO_2 is also important in observing the LX_D peak in MoS_2.

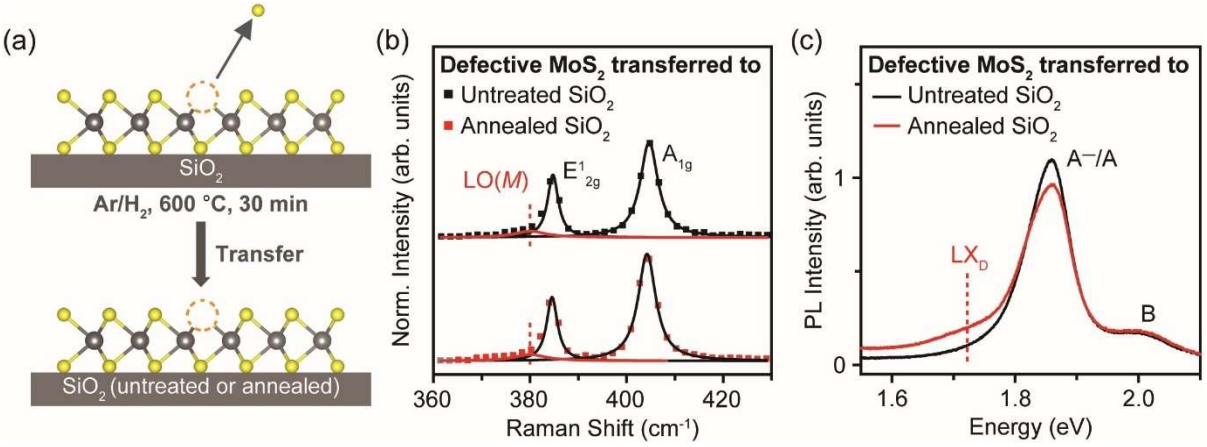

Figure 5.9. Transfer of defective monolayer MoS_2 onto untreated and annealed SiO_2. (a) Schematic of defective MoS_2 transfer from the original SiO_2 substrate to another untreated or annealed SiO_2 substrate. (b) Raman spectra of transferred defective monolayer MoS_2 on untreated and annealed SiO_2, normalized to the intensity of Si reference peak. The LO(M) mode remains in transferred samples, implying that the samples are defective. (c) PL spectra of transferred defective monolayer MoS_2 on untreated and annealed SiO_2. The LX_D peak is observed in defective MoS_2 on annealed SiO_2 but not on untreated SiO_2.

Therefore, I fabricated defective samples on SiO_2 and transferred them onto SiO_2 substrates that were also separately annealed at 600 °C in Ar/H_2. The PL spectra of defective MoS_2 on annealed SiO_2 shows a small and broad LX_D peak (**Figure 5.9c**, red curve). To exclude the possibility that the LX_D peak is coming from annealed SiO_2, I transferred pristine MoS_2 on annealed SiO_2 and compared it with pristine MoS_2 on untreated SiO_2 (**Figure 5.10**). The deconvoluted spectra of the two show an absence of LX_D peak, suggesting that the LX_D peak does not come from annealed SiO_2.

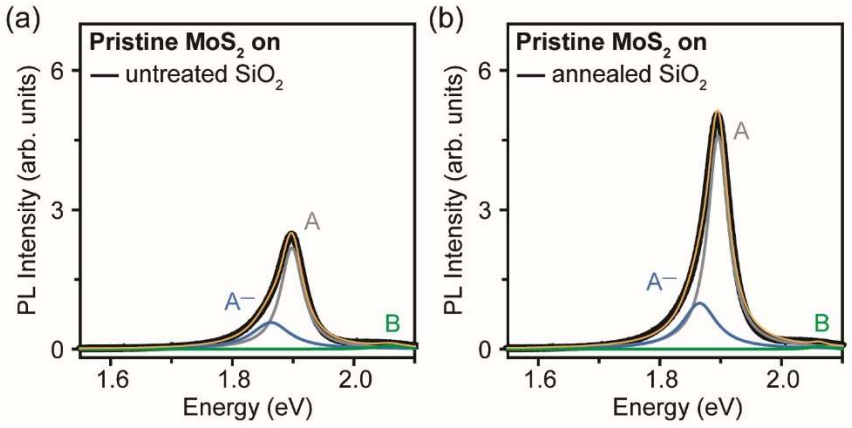

Figure 5.10. Pristine monolayer MoS_2 on untreated and annealed SiO_2. (a–b) RT PL spectra RT PL spectra of pristine monolayer MoS_2 on (a) untreated SiO_2 and (b) annealed SiO_2, fitted with Lorentz peaks. Denotation: A exciton in grey, A^- trion in blue, B exciton in green, and cumulative fit curve in yellow. For pristine MoS_2, the ratio of integrated intensity of A^- trion to A exciton, $I(A^-)/I(A)$, is lower on annealed SiO_2 (0.35) than on untreated SiO_2 (0.44).

The synchrotron results (**Figure 4.2** in **Chapter 4**) show that annealing of MoS_2 on SiO_2 at 600 °C in Ar/H_2 leads to sulfur deficiency. The PL results (**Figure 4.3** in **Chapter 4**) are also consistent with creation of in-gap states close to the conduction band due to creation of sulfur vacancies. Thus, the results of defective MoS_2 on pristine SiO_2 are puzzling. One explanation for this is that pristine SiO_2 contains a high concentration of surface defects such as unsaturated bonds, which leads to a high electron density on the surface.[158] Further, the deconvoluted PL results show that SiO_2 can influence the ratio of integrated intensity of A^- trion to A exciton, $I(A^-)/I(A)$, which indicates doping from the substrate (**Figure 5.10, 5.11**).

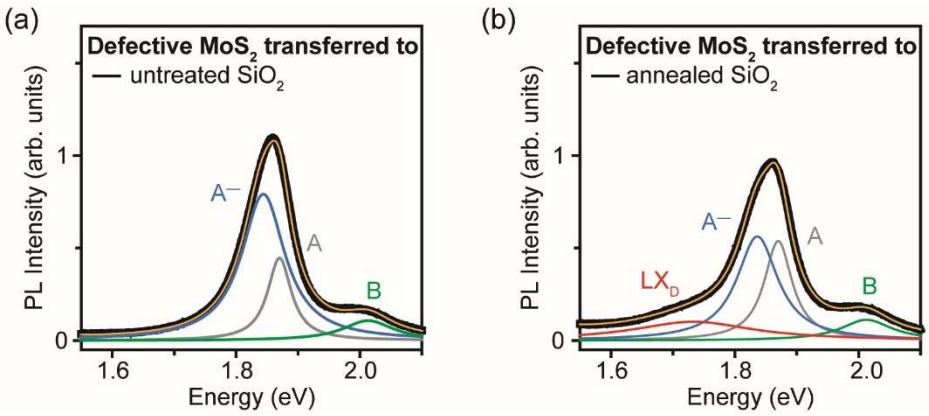

Figure 5.11. Deconvoluted RT PL spectra of defective monolayer MoS_2 on (a) untreated and (b) annealed SiO_2, fitted with Lorentz peaks. Denotation: A exciton in grey, A^- trion in blue, B exciton in green, LX_D emission in red, and cumulative fit curve in yellow. PL spectrum in (a) consists of A exciton, A^- trion, and B exciton only, while in (b) it shows an additional LX_D peak. For defective MoS_2, the ratio of integrated intensity of A^- trion to A exciton, $I(A^-)/I(A)$, is lower on annealed SiO_2 (1.54) than on untreated SiO_2 (3.22).

In the case of untreated SiO_2, it can be seen that the surface states lead to a higher $I(A^-)/I(A)$ ratio relative to the annealed SiO_2 case where the surface states are relatively decreased (**Figure 5.12a**). In the defective MoS_2 samples transferred onto untreated SiO_2, the $I(A^-)/I(A)$ ratio is much higher because the presence of sulfur vacancies introduces free electrons in the MoS_2 (**Figure 5.12a**). The $I(A^-)/I(A)$ ratio decreases substantially when the defective MoS_2 is transferred onto annealed SiO_2, indicating that doping from surface states on SiO_2 is suppressed. The $I(A^-)/I(A)$ ratio in defective MoS_2 is still higher than in pristine MoS_2 because while the electron doping surface states from SiO_2 are suppressed, the presence of sulfur vacancies renders the material n-type doped. A schematic of the energy band diagram of defective monolayer MoS_2 with different doping levels is shown in **Figure 5.12b**. The horizontal dashed lines represent Fermi levels, while the horizontal solid lines represent energy states due to defects. An electron is photoexcited from the valence band to the conduction band (denoted by the green arrow), relaxed to the conduction band edge (denoted by the black arrow), and then relaxed to the in-gap defect state (denoted by the yellow arrow). The localized electron at defect state can be relaxed to valence band edge and recombine with a hole, releasing a LX_D photon (denoted by the red arrow). In defective MoS_2, electron doping from the SiO_2 substrate can occupy the in-gap states of sulfur vacancies as indicated by the shift of

Fermi level close to the defect state energy on the right side of the schematic in **Figure 5.12b**.[159] In contrast, when the doping from the substrate is minimized, the Fermi level remains mid-gap – allowing excited electrons to relax down to the sulfur vacancy in-gap states and radiatively recombine with holes to emit LX_D photons.

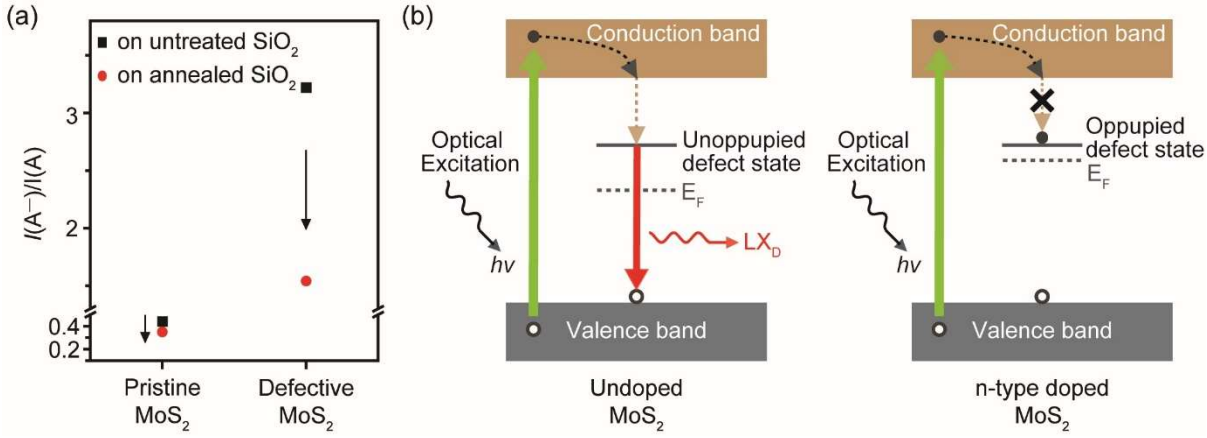

Figure 5.12. Pristine and defective monolayer MoS_2 on untreated and annealed SiO_2 substrate. (a) The ratio of integrated intensity of A^- trion to A exciton, $I(A^-)/I(A)$, for pristine and defective MoS_2 on untreated and annealed SiO_2. For both pristine and defective MoS_2, the $I(A^-)/I(A)$ ratio is lower on annealed SiO_2 than on untreated SiO_2. (b) Proposed schematic energy band diagram of defective monolayer MoS_2.

5.4 Gate Dependence of Defect-Mediated Emission

The influence of electrostatic doping on defect-mediated emission at RT was studied by modulating doping in MoS_2 by electrostatic gating. Defective monolayer MoS_2 was fabricated on 300 nm SiO_2/Si through Ar/H_2 annealing to generate defect-mediated emission. FETs using defective monolayer MoS_2 as the channel were fabricated to conduct gate-dependent PL at RT (see schematic of the device in **Figure 5.13a**). Top electrodes were patterned with photolithography (laser writer LW405B from Microtech, AZ5214E photoresist) followed by metal deposition (10 nm In/80 nm Au) and lift-off process. The gate voltage (V_g) was varied from −30 V to +60V to modulate the doping. It can be seen that both A^-/A and LX_D emission decrease with gate bias due to the non-radiative recombination induced by trions (**Figure 5.13b**).[39] Deconvoluting the spectra reveals monotonic decrease in the integrated intensities of A exciton and LX_D peaks, whereas an increase in A^- trion peak intensity is

observed (**Figure 5.13c**). The $I(A^-)/I(A)$ ratio varied from 0.96 at $V_g = -30$ V (hole doping) to 3.44 at +60 V (electron doping).[38] The integrated RT PL intensity ratio of LX_D emission to the sum of A exciton and A^- trion emission, $I(LX_D)/[I(A)+I(A^-)]$, is inversely proportional to the $I(A^-)/I(A)$ ratio, indicating that electron doping reduces the defect-mediated emission LX_D (**Figure 5.13d**). Therefore, the absence of LX_D peak on untreated SiO_2 despite the fact that MoS_2 contains sulfur vacancies may be attributed to electron doping from the substrate.

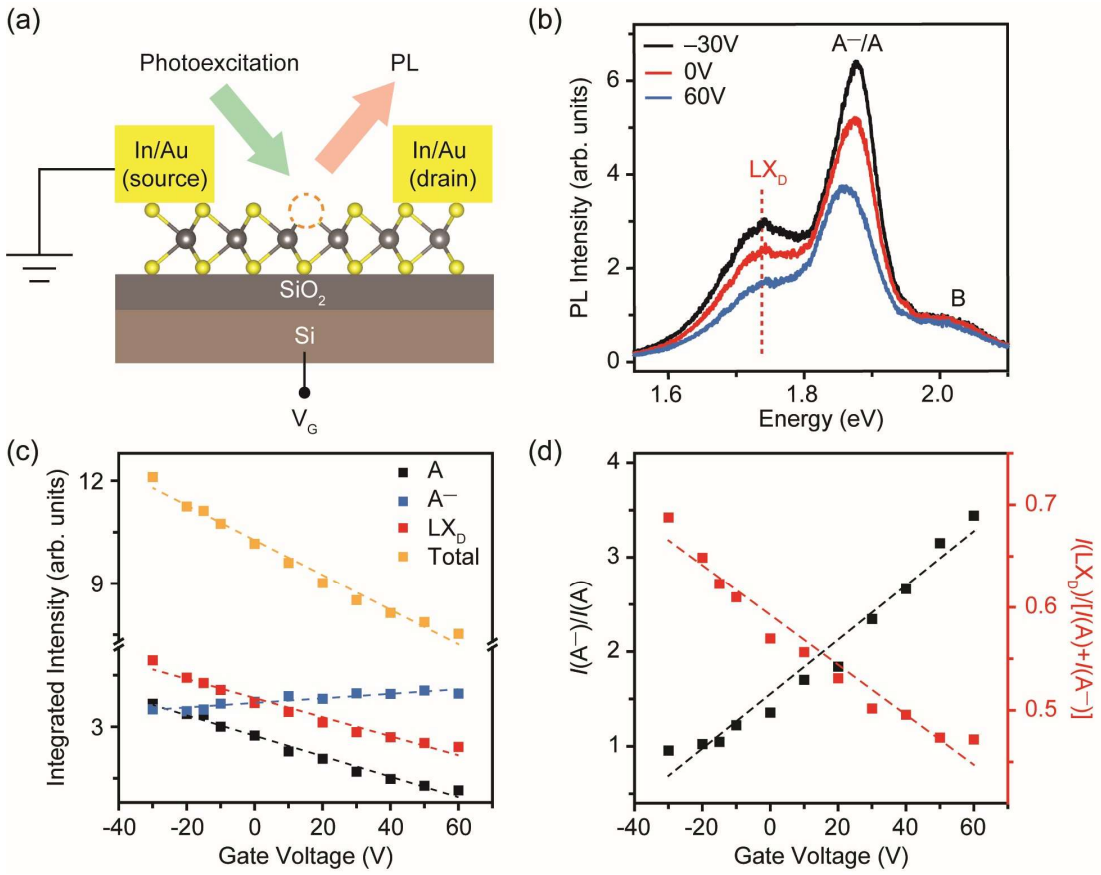

Figure 5.13. Gate dependence of RT LX_D emission. (a) Schematic of MoS_2 FET and gate tuning of PL in defective monolayer MoS_2. (b) RT PL spectra of defective monolayer MoS_2 at different gate voltages (V_g). (c) The integrated intensity of A exciton, A^- trion, and LX_D peak, and their total contribution. (d) The ratio of integrated intensity of A^- trion to A exciton, $I(A^-)/I(A)$, and the integrated RT PL intensity ratio of LX_D emission to the sum of A exciton and A^- trion emission, $I(LX_D)/[I(A)+I(A^-)]$, at different V_g. At negative V_g (hole doping), LX_D emission becomes relatively stronger, while at positive V_g (electron doping), LX_D emission becomes relatively weaker.

5.5 Transfer of Defective MoS_2 from SiO_2 to HfO_2

One more control experiment was performed to understand the role of doping from substrates in influencing the LX_D peak. For this part of the study, defective monolayer MoS_2 was fabricated on SiO_2 and then transferred it onto HfO_2. First, Synchrotron XPS of MoS_2 on untreated HfO_2 was measured, as shown in **Figure 5.14**. Pristine MoS_2 on untreated HfO_2 shows characteristic Mo 3d doublet with a binding energy that is 0.54 eV lower than pristine MoS_2 on SiO_2, implying that MoS_2 is less electron-doped by HfO_2. Accordingly, the lower electron doping leads to appearance of the LX_D peak from sulfur vacancies in the defective MoS_2 samples (**Figure 5.15a**). This suggests that for MoS_2 containing sulfur vacancies, it is indeed possible to observe LX_D peak when deposited on untreated HfO_2. The results in **Figures 5.7 and 5.8** suggest that directly annealing MoS_2 on HfO_2 leads to either change in

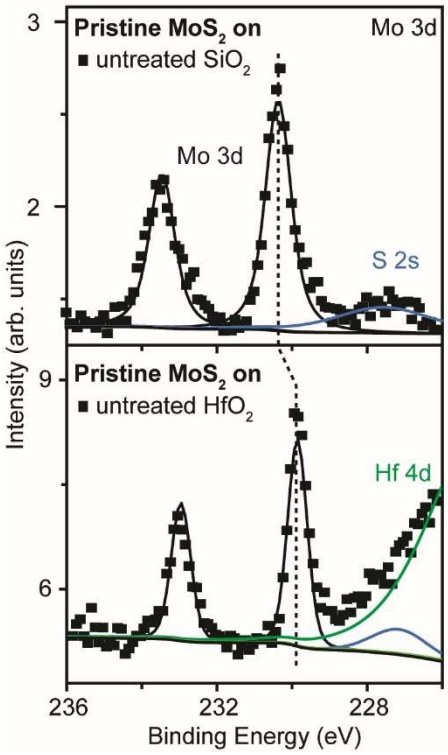

Figure 5.14. XPS spectra of the Mo 3d core level in pristine MoS_2 on untreated SiO_2 and on untreated HfO_2 measured using synchrotron 1 keV soft X-rays. MoS_2 on untreated SiO_2 shows the characteristic Mo 3d doublet from stoichiometric MoS_2 (denoted in black) and S 2s peak (denoted in blue). MoS_2 on untreated HfO_2 shows additional Hf 4d doublet (denoted in green), with Mo 3d doublet and S 2s peak showing lower binding energy than pristine MoS_2/SiO_2, indicating that MoS_2 is less electron-doped by HfO_2.

the substrate or the interface between MoS_2 and HfO_2 that leads to suppression of the LX_D peak. However, I consistently did not observe RT LX_D peak when I annealed HfO_2 first in Ar/H_2 (600 °C, 30min) and then transferred defective MoS_2 onto annealed HfO_2 (**Figure 5.15a**). This indicates that the absence of defect-mediated emission in defective MoS_2 is due to changes in HfO_2 through annealing. The RT Raman spectra show the red shift of A_{1g} mode of defective MoS_2 on annealed HfO_2, indicating that MoS_2 is more electron-doped by annealed HfO_2 than untreated HfO_2 (**Figure 5.15b**). While it was not possible to investigate these changes in HfO_2 after annealing in this thesis, this could be an interesting future project for the next PhD student.

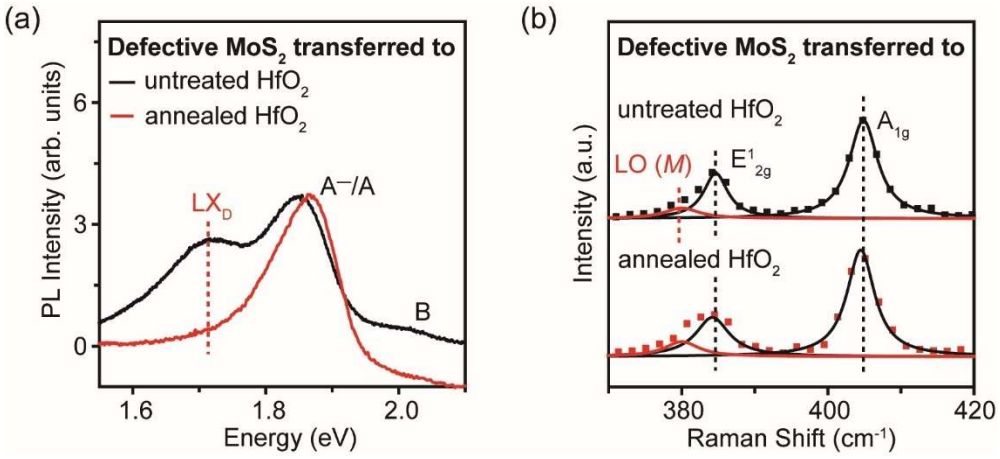

Figure 5.15. (a) RT PL spectra of defective monolayer MoS_2 on HfO_2. The defective MoS_2 shows strong LX_D emission on untreated HfO_2, but not on annealed HfO_2. (b) RT Raman spectra of defective monolayer MoS_2 on HfO_2. The red shift of A_{1g} peak is attributed to stronger electron doping of MoS_2 on annealed HfO_2.

6.6 Summary

The LX_D peak has been shown to be influenced by the substrate. Specifically, doping from the substrate can fill the in-gap states created by sulfur vacancies – reducing the concentration of defect states available for radiative recombination. The LX_D peak is present when MoS_2 is annealed on hBN because of the absence of doping from the substrate. When defective MoS_2 is fabricated on SiO_2 and then transferred to an untreated SiO_2, the LX_D peak disappears. This is attributed to electron doping from adsorbates or surface states from the SiO_2. Annealing the SiO_2 substrates to remove adsorbates or surface states through reconstruction to suppress

doping leads to observation of the LX_D peak. I demonstrate the role of doping on the PL emission peaks – including the LX_D peak – by performing the measurements in the presence of gate bias. The results show that gate doping of MoS_2 leads to suppression of LX_D – consistent with the argument that suppression of LX_D comes from doping effects from the substrate. Transfer of defective MoS_2 from SiO_2 to an untreated HfO_2 leads to the appearance of LX_D peak due to decreased electron doping as observed by XPS. In contrast, the LX_D emission is suppressed when defective MoS_2 is transferred to an annealed HfO_2. The results for this chapter are summarized in **Table 5.1** on the next page.

Table 5.1. Summary of control experiments presented in this chapter. Substrates: SiO_2 = SiO_2 (300 nm thick) on Si; hBN = 24 – 27 nm thick hBN; HfO_2 = HfO_2 (50 nm thick) on Si; Ar/H_2 annealed SiO_2 (or HfO_2) = SiO_2 (or HfO_2) annealed in Ar/H_2 at 600 °C for 30 min. Samples: ① – ④ MoS_2 annealed on ① SiO_2, ② hBN on SiO_2, ③ hBN on HfO_2, and ④ HfO_2, respectively. ⑤ – ⑦ Defective MoS_2 fabricated on SiO_2 first and then transferred to ⑤ Untreated SiO_2, ⑥ Annealed SiO_2, ⑦ Untreated HfO_2, and ⑧ Annealed HfO_2, respectively.

Sample			**LX_D peak**	**I observe**
MoS_2	annealed on	① SiO_2	Y	When MoS_2 is annealed on SiO_2 and hBN, LX_D peak is observed.
		② hBN on SiO_2	Y	
		③ hBN on HfO_2	Y	
		④ HfO_2	N	When MoS_2 is annealed on HfO_2, LX_D peak is not observed. This could be due to: 1) Sulfur vacancies are not created in MoS_2 when annealed on HfO_2. 2) HfO_2 suppresses LX_D emission.
Transfer of *defective MoS_2*	to	⑤ Untreated SiO_2	N	LX_D peak can be electrostatically suppressed.
		⑥ Annealed SiO_2	Y	
		⑦ Untreated HfO_2	Y	LX_D peak is not suppressed by untreated HfO_2.
		⑧ Annealed HfO_2	N	Annealing of HfO_2 substrate suppresses the LX_D emission and further work is required.

Chapter 6 Conclusion & Perspectives

The strong light-matter interactions in two-dimensional (2D) transition metal dichalcogenides (TMDs) results in high absorption coefficients,[24] photoluminescence (PL) from tightly bound excitons, and valley-selective circular dichroism due to their non-centrosymmetric crystal structure. Further, van der Waals interlayer interactions allow the creation of vertical heterostructures with tunable optoelectronic phenomena. As a result, 2D TMDs are interesting for electronic devices, photovoltaics, and nanophotonics. However, monolayer TMDs prepared by mechanical exfoliation or chemical vapor deposition typically possess a native defect density of ~10^{13} cm^{-2}. These defects are mostly chalcogen vacancies that cause changes in electronic structure by forming in-gap states and carrier doping. Monolayer TMDs are surprisingly tolerant to chalcogen vacancy defects. That is, they can host up to 1×10^{15} cm^{-2} chalcogen vacancies without significant distortion to their atomic structure.[82] Above this concentration, however, damage to their structure occurs and disordered regions appear. Various approaches for defect generation, such as annealing[127,134], electron beam irradiation[133,135,139], focused X-ray beam irradiation[132], and focused ion beam exposure[82,107,130,137,138], have been reported. Despite the high density of defects, previous observations of defect-related emission from in-gap states have mostly been limited to low temperatures. The in-gap defect states lie in the bandgap with a binding energy of ~200 meV and are expected to strongly trap excitons at room temperature (RT, ~300 K). In this thesis, electronic structure and excitonic behavior of atomically thin 2D TMDs affected by vacancy defects have been studied.

Firstly, annealing in an Ar/H_2 (95 *vol.*%/5 *vol.*%) atmosphere has been shown to be a reproducible method for generation of sulfur vacancies in 2D MoS_2. These sulfur vacancies induce in-gap electronic states and lead to RT localized exciton emission that can be tuned with annealing temperature and duration. The RT defect-mediated emission is the strongest when MoS_2 is annealed at 600 °C for 30 mins. The temperature-dependent PL results measured from 300 K to 10 K reveal that the in-gap defect states introduced through annealing are different from the adsorbate-related in-gap states. The trapping behavior of in-gap states is confirmed by time-resolved PL decay that shows longer lifetime for the defect-mediated emission than band edge excitons, both at room and low temperatures. XPS measurements show that the strongest RT defect-mediated emission is observed at sulfur vacancy densities of ~1.8×10^{14}

cm^{-2}. Both PL and XPS results show that sulfur vacancies are electron donors. This annealing method has been extended to 2D WS_2, $MoSe_2$ and WSe_2. Similar RT defect-mediated emission is observed in WS_2, but not in $MoSe_2$ and WSe_2.

Secondly, I have demonstrated that sulfur vacancies can be passivated by annealing in sulfur or selenium vapor. Since the defect-mediated emission is a unique signature of sulfur vacancies, the passivation effect is also monitored by PL spectroscopy. The defect-mediated emission is fully suppressed both at RT and 10 K by annealing the defective MoS_2 in sulfur vapor at 500 °C. XPS measurements show the absence of non-stoichiometric Mo 3d doublet that supports the passivation via chemical bonding. However, both PL and XPS results suggest excess electron doping that is due to the physisorbed sulfur which is identified by a second S 1s peak in XPS. The electron doping can be reduced by removing the physisorbed sulfur via annealing in a high vacuum of $<10^{-6}$ mbar. The sulfur vacancies can also be filled by selenium at annealing temperature of ≥600 °C in selenium vapor.

Lastly, I have explored the influence of dielectric substrates on defect-mediated emission. The Ar/H_2 annealing method has been extended to hBN and HfO_2 substrates. The defect-mediated emission is observed on hBN, but not on HfO_2. However, when defective MoS_2 is fabricated on SiO_2 first and then transferred onto an untreated SiO_2, the defect-mediated emission is not observed. This is attributed to the large electron density at the surface of SiO_2 that leads to substantial electron doping of MoS_2. The PL as a function of doping concentration modulated by gate voltage shows that the defect-mediated emission is sensitive to doping – decreasing with higher electron concentration in the channel. The defect-mediated emission can be recovered by annealing of SiO_2, suggesting that surface reconstruction or removal of adsorbates via annealing decreases the influence of doping on MoS_2. The decreased electron doping in MoS_2 on untreated HfO_2 as observed by XPS leads to the observation of defect-mediated emission. However, the defect-mediated emission is suppressed by annealing of HfO_2.

Overall, I have shown that RT PL from defects in 2D TMDs can be tuned by controlling defect density in TMDs. Chalcogen vacancies in 2D TMDs (*e.g.*, WSe_2) have been utilized as single photon emitters at low temperatures (up to 150 K).[141,142] However, it remains challenging to achieve single photon emission at RT. I have shown that it is possible to observe PL from sulfur vacancies in monolayer MoS_2 and WS_2 at RT. However, the defect-mediated emission peak was broad, with the full width at half maximum (FWHM) of ~120 meV at RT and ~55 meV at

10 K. These broad emission features indicate that the emitters lack antibunching characteristics, hindering the utilization of MoS_2 as RT single photon emission source. This is probably due to the high density of sulfur vacancies (~1.8×10^{14} cm^{-2}). Future work includes decreasing the density of sulfur vacancies by defect passivation strategy while enhancing the PL from sulfur vacancies. The latter includes electrostatically or chemically reducing electron concentration in MoS_2 to expose more in-gap defect states for radiative recombination. Strain engineering is another strategy to tune the in-gap defect states with respect to the band edges, thus affecting the trapping rate of electrons at defect states. For the mechanically exfoliated samples on support substrates used in this thesis, the PL emission energies are very close to those of free-standing samples.[31] This indicates that these mechanically exfoliated samples contain negligible strain. Typical strategies for applying strain include transferring 2D TMDs onto nanopillar-patterned substrates[160,161], thermal expansion[162], and flexible polymer substrates[163].

Previous work has shown that sulfur vacancies in MoS_2 can be passivated by incorporating oxygen in chemical vapor deposition (CVD). Compared to passivating sulfur vacancies with extrinsic atomic species (*e.g.*, oxygen[164]), I think passivation with native sulfur atoms may be a better way. In this study, I have shown that the sulfur vacancies can be passivated by annealing in sulfur vapor and the defect density has been calculated from the XPS stoichiometry. However, the detection limits for atomic composition from XPS generally range from 0.1% atomic percent (*at*%) to 1 *at*%.[165] For sulfur vacancies in MoS_2, this is translated to ~2.3×10^{12} cm^{-2} to ~2.3×10^{13} cm^{-2}. Therefore, it is essential to extend the characterization to atomic-scale microscopy measurements, including typical scanning transmission electron microscopy (STEM) and scanning tunneling microscopy (STM). However, STEM typically introduces additional defects due to electron beam damage, while STM requires complex sample preparation to create conductive pathways. Recently, atomic force microscopy (AFM) has been explored for the characterization of atomic defects, including conductive AFM (CAFM)[87] and lateral force microscopy (LFM). CAFM is also limited to measuring conductive materials only, while LFM has the potential to measure semiconducting TMDs without the need to transfer TMDs from non-conductive substrates (typically used for growth) to conductive substrates. With reliable techniques to characterize chalcogen vacancies in a low defect density regime, the passivated samples can be systematically compared across various passivation parameters (*e.g.*, temperature, partial pressure of gaseous components, carrier gas flow) and minimize the defect concentration accordingly.

More importantly, I would like to emphasize passivating chalcogen vacancies in large-scale CVD-grown MoS_2. Studies on CVD-grown MoS_2 have shown that it is free of adsorbate-related emission even at low temperatures and this is attributed to the chemisorption of oxygen.[166] Therefore, it might be important to anneal CVD-grown MoS_2 in Ar/H_2 (95 *vol.*%/5 *vol.*%) atmosphere to remove chemisorbed oxygen first and then expose it to sulfur vapor for passivation without exposing the sample to air.

Another factor that may affect the density of chalcogen vacancies is strain (typically tensile strain) that is applied on TMDs during sample cooling down through CVD growth. In principle, the tensile strain deforms the lattice by increasing the interatomic spacing that can affect the bond length and bond strength, thereby affecting the formation energy of vacancy defects. Therefore, it might be worthwhile to study the influence of strain on formation energy of defects for further optimization of passivating chalcogen vacancies.

Besides physically passivating defects, I also consider the possibility of shifting the in-gap defect states outside the bandgap to eliminate the active carrier trapping sites to improve the electronic performance of 2D TMDs. I think this can be achieved by strain engineering considering the fact that the selenium single-vacancy level shifts closer to the conduction band under tensile strain.[142] However, this is experimentally limited by technical difficulties due to the deep nature of in-gap states of chalcogen vacancies. The tensile strain can be applied up to 300 meV for MoS_2 but is still not enough to overcome the barrier of ~600 meV.[163] This requires polymers with sufficiently high Young's modulus or substrates with significant thermal mismatch to transfer strain to TMDs more effectively.

List of Abbreviation

Abbreviation	Definition
2D	Two-dimensional
3D	Three-dimensional
AFM	Atomic force microscopy
ALD	Atomic layer deposition
CAFM	Conductive atomic force microscopy
CB	Conduction band
CBM	Conduction band minimum
CLQB	Covalent-like quasi bonding
CVD	Chemical vapor deposition
DFT	Density Functional Theory
FWHM	Full width at half maximum
HAADF	High-angle annular dark-field
LVM	Local vibrational mode
MOCVD	Metal-organic chemical vapor deposition
PL	Photoluminescence
PLE	Photoluminescence excitation
PLD	Pulsed laser deposition
PVD	Physical vapor deposition
QY	Quantum yield
RT	Room temperature
STEM	Scanning transmission electron microscope
STM/STS	Scanning tunneling microscopy/spectroscopy
TMD	Transition metal dichalcogenides
VB	Valence band
VBM	Valence band maximum
vdW	van der Waals
XPS	X-ray photoelectron spectroscopy

References

(1) Shimoda, T.; Matsuki, Y.; Furusawa, M.; Aoki, T.; Yudasaka, I.; Tanaka, H.; Iwasawa, H.; Wang, D.; Miyasaka, M.; Takeuchi, Y. Solution-Processed Silicon Films and Transistors. *Nature* **2006**, *440* (7085), 783–786.

(2) Nomura, K.; Ohta, H.; Ueda, K.; Kamiya, T.; Hirano, M.; Hosono, H. Thin-Film Transistor Fabricated in Single-Crystalline Transparent Oxide Semiconductor. *Science* **2003**, *300* (5623), 1269–1272.

(3) Ryu, Y. R.; Lee, T. S.; Lubguban, J. A.; White, H. W.; Park, Y. S.; Youn, C. J. ZnO Devices: Photodiodes and P-Type Field-Effect Transistors. *Appl. Phys. Lett.* **2005**, *87* (15), 153504.

(4) Saga, T. Advances in Crystalline Silicon Solar Cell Technology for Industrial Mass Production. *NPG Asia Mater.* **2010**, *2* (3), 96–102.

(5) Dai, Q.; Duty, C. E.; Hu, M. Z. Semiconductor-Nanocrystals-Based White Light-Emitting Diodes. *Small* **2010**, *6* (15), 1577–1588.

(6) Qiao, L.; Xiao, H. Y.; Meyer, H. M.; Sun, J. N.; Rouleau, C. M.; Puretzky, A. A.; Geohegan, D. B.; Ivanov, I. N.; Yoon, M.; Weber, W. J.; Biegalski, M. D. Nature of the Band Gap and Origin of the Electro-/Photo-Activity of Co_3O_4. *J. Mater. Chem. C* **2013**, *1* (31), 4628–4633.

(7) Zheng, X.; Chen, B.; Dai, J.; Fang, Y.; Bai, Y.; Lin, Y.; Wei, H.; Zeng, X. C.; Huang, J. Defect Passivation in Hybrid Perovskite Solar Cells Using Quaternary Ammonium Halide Anions and Cations. *Nat. Energy* **2017**, *2* (7), 17102.

(8) Zhou, H.; Song, T. Bin; Hsu, W. C.; Luo, S.; Ye, S.; Duan, H. S.; Hsu, C. J.; Yang, W.; Yang, Y. Rational Defect Passivation of $Cu_2ZnSn(S,Se)_4$ Photovoltaics with Solution-Processed Cu_2ZnSnS_4:Na Nanocrystals. *J. Am. Chem. Soc.* **2013**, *135* (43), 15998–16001.

(9) Hallam, B. J.; Hamer, P. G.; Wenham, S. R.; Abbott, M. D.; Sugianto, A.; Wenham, A. M.; Chan, C. E.; Xu, G.; Kraiem, J.; Degoulange, J.; Einhaus, R. Advanced Bulk Defect Passivation for Silicon Solar Cells. *IEEE J. Photovolt.* **2014**, *4* (1), 88–95.

(10) Nicoara, N.; Manaligod, R.; Jackson, P.; Hariskos, D.; Witte, W.; Sozzi, G.; Menozzi, R.; Sadewasser, S. Direct Evidence for Grain Boundary Passivation in Cu(In,Ga)Se_2 Solar Cells through Alkali-Fluoride Post-Deposition Treatments. *Nat. Commun.* **2019**, *10* (1), 3980.

(11) Otto, M.; Kroll, M.; Käsebier, T.; Salzer, R.; Tünnermann, A.; Wehrspohn, R. B. Extremely Low Surface Recombination Velocities in Black Silicon Passivated by Atomic Layer Deposition. *Appl. Phys. Lett.* **2012**, *100* (19), 191603.

(12) Marschall, R. Semiconductor Composites: Strategies for Enhancing Charge Carrier Separation to Improve Photocatalytic Activity. *Adv. Funct. Mater.* **2014**, *24* (17), 2421–2440.

(13) Jin, L.; Pfender, M.; Aslam, N.; Neumann, P.; Yang, S.; Wrachtrup, J.; Liu, R. B. Proposal for a Room-Temperature Diamond Maser. *Nat. Commun.* **2015**, *6* (1), 8251.

(14) Breeze, J. D.; Salvadori, E.; Sathian, J.; Alford, N. M. N.; Kay, C. W. M. Continuous-Wave Room-Temperature Diamond Maser. *Nature* **2018**, *555* (7697), 493–496.

(15) Cui, Y.; Wang, H.; Yuan, H.; Seung Sae Hong, A.; Li, Y. Physical and Chemical Tuning of Two-Dimensional Transition Metal Dichalcogenides. *Chem. Soc. Rev.* **2015**, *44*, 2664.

(16) Voiry, D.; Mohite, A.; Chhowalla, M. Phase Engineering of Transition Metal Dichalcogenides. *Chem. Soc. Rev.* **2015**, *44* (9), 2702–2712.

(17) Yang, H.; Kim, S. W.; Chhowalla, M.; Lee, Y. H. Structural and Quantum-State Phase Transitions in van Der Waals Layered Materials. *Nat. Phys.* **2017**, *13* (10), 931–937.

(18) Kolobov, A. V.; Tominaga, J. Two-Dimensional Transition-Metal Dichalcogenides. *Springer Ser. Mater. Sci.* **2016**, *239*, 148–153.

(19) Kappera, R.; Voiry, D.; Yalcin, S. E.; Branch, B.; Gupta, G.; Mohite, A. D.; Chhowalla, M. Phase-Engineered Low-Resistance Contacts for Ultrathin MoS_2 Transistors. *Nat. Mater.* **2014**, *13* (12), 1128–1134.

(20) Chhowalla, M.; Shin, H. S.; Eda, G.; Li, L.-J.; Loh, K. P.; Zhang, H. The Chemistry of Two-Dimensional Layered Transition Metal Dichalcogenide Nanosheets. *Nat. Chem.* **2013**, *5* (4), 263–275.

(21) Liu, H. L.; Shen, C. C.; Su, S. H.; Hsu, C. L.; Li, M. Y.; Li, L. J. Optical Properties of Monolayer Transition Metal Dichalcogenides Probed by Spectroscopic Ellipsometry. *Appl. Phys. Lett.* **2014**, *105* (20), 201905.

(22) Ahn, E. C. 2D Materials for Spintronic Devices. *NPJ 2D Mater. Appl.* **2020**, *4* (1), 17.

(23) Schaibley, J. R.; Yu, H.; Clark, G.; Rivera, P.; Ross, J. S.; Seyler, K. L.; Yao, W.; Xu, X. Valleytronics in 2D Materials. *Nat. Rev. Mater.* **2016**, *1* (11), 16055.

(24) Li, Y.; Chernikov, A.; Zhang, X.; Rigosi, A.; Hill, H. M.; Van Der Zande, A. M.; Chenet, D. A.; Shih, E. M.; Hone, J.; Heinz, T. F. Measurement of the Optical Dielectric Function of Monolayer Transition-Metal Dichalcogenides: MoS_2, $MoSe_2$, WS_2, and WSe_2. *Phys. Rev. B* **2014**, *90* (20), 205422.

(25) Nassiri Nazif, K.; Nitta, F. U.; Daus, A.; Saraswat, K. C.; Pop, E. Efficiency Limit of Transition Metal Dichalcogenide Solar Cells. *Commun. Phys.* **2023**, *6* (1), 367.

(26) Vogl, T.; Sripathy, K.; Sharma, A.; Reddy, P.; Sullivan, J.; Machacek, J. R.; Zhang, L.; Karouta, F.; Buchler, B. C.; Doherty, M. W.; Lu, Y.; Lam, P. K. Radiation Tolerance of Two-Dimensional Material-Based Devices for Space Applications. *Nat. Commun.* **2019**, *10* (1), 1202.

(27) Regan, E. C.; Wang, D.; Paik, E. Y.; Zeng, Y.; Zhang, L.; Zhu, J.; MacDonald, A. H.; Deng, H.; Wang, F. Emerging Exciton Physics in Transition Metal Dichalcogenide Heterobilayers. *Nat. Rev. Mater.* **2022**, *7* (10), 778–795.

(28) Sung, J.; Shin, D.; Cho, H.; Lee, S. W.; Park, S.; Kim, Y. D.; Moon, J. S.; Kim, J.-H.; Gong, S.-H. Room-Temperature Continuous-Wave Indirect-Bandgap Transition Lasing in an Ultra-Thin WS_2 Disk. *Nat. Photonics* **2022**, *16* (11), 792–797.

(29) Tebyetekerwa, M.; Zhang, J.; Xu, Z.; Truong, T. N.; Yin, Z.; Lu, Y.; Ramakrishna, S.; Macdonald, D.; Nguyen, H. T. Mechanisms and Applications of Steady-State Photoluminescence Spectroscopy in Two-Dimensional Transition-Metal Dichalcogenides. *ACS Nano* **2020**, *14* (11), 14579–14604.

(30) Mak, K. F.; Lee, C.; Hone, J.; Shan, J.; Heinz, T. F. Atomically Thin MoS_2: A New Direct-Gap Semiconductor. *Phys. Rev. Lett.* **2010**, *105* (13), 136805.

(31) Peimyoo, N.; Deilmann, T.; Withers, F.; Escolar, J.; Nutting, D.; Taniguchi, T.; Watanabe, K.; Taghizadeh, A.; Craciun, M. F.; Thygesen, K. S.; Russo, S. Electrical Tuning

of Optically Active Interlayer Excitons in Bilayer MoS_2. *Nat. Nanotechnol.* **2021**, *16* (8), 888–893.

(32) Mueller, T.; Malic, E. Exciton Physics and Device Application of Two-Dimensional Transition Metal Dichalcogenide Semiconductors. *NPJ 2D Mater. Appl.* **2018**, *2* (1), 29.

(33) Chernikov, A.; Berkelbach, T. C.; Hill, H. M.; Rigosi, A.; Li, Y.; Aslan, O. B.; Reichman, D. R.; Hybertsen, M. S.; Heinz, T. F. Exciton Binding Energy and Nonhydrogenic Rydberg Series in Monolayer WS_2. *Phys. Rev. Lett.* **2014**, *113* (7), 076802.

(34) Ugeda, M. M.; Bradley, A. J.; Shi, S.-F.; da Jornada, F. H.; Zhang, Y.; Qiu, D. Y.; Ruan, W.; Mo, S.-K.; Hussain, Z.; Shen, Z.-X.; Wang, F.; Louie, S. G.; Crommie, M. F. Giant Bandgap Renormalization and Excitonic Effects in a Monolayer Transition Metal Dichalcogenide Semiconductor. *Nat. Mater.* **2014**, *13* (12), 1091–1095.

(35) Sergeev, R. A.; Suris, R. A.; Astakhov, G. V.; Ossau, W.; Yakovlev, D. R. Universal Estimation of X-Trion Binding Energy in Semiconductor Quantum Wells. *Eur. Phys. J. B* **2005**, *47* (4), 541–547.

(36) Huang, J.; Hoang, T. B.; Mikkelsen, M. H. Probing the Origin of Excitonic States in Monolayer WSe_2. *Sci. Rep.* **2016**, *6* (1), 22414.

(37) Drüppel, M.; Deilmann, T.; Krüger, P.; Rohlfing, M. Diversity of Trion States and Substrate Effects in the Optical Properties of an MoS_2 Monolayer. *Nat. Commun.* **2017**, *8*(1), 2117.

(38) Mak, K. F.; He, K.; Lee, C.; Lee, G. H.; Hone, J.; Heinz, T. F.; Shan, J. Tightly Bound Trions in Monolayer MoS_2. *Nat. Mater.* **2013**, *12* (3), 207–211.

(39) Lien, D.-H.; Uddin, S. Z.; Yeh, M.; Amani, M.; Kim, H.; Ager, J. W.; Yablonovitch, E.; Javey, A. Electrical Suppression of All Nonradiative Recombination Pathways in Monolayer Semiconductors. *Science* **2019**, *364* (6439), 468–471.

(40) Amani, M.; Lien, D.-H.; Kiriya, D.; Xiao, J.; Azcatl, A.; Noh, J.; Madhvapathy, S. R.; Addou, R.; KC, S.; Dubey, M.; Cho, K.; Wallace, R. M.; Lee, S.-C.; He, J.-H.; Ager, J. W.; Zhang, X.; Yablonovitch, E.; Javey, A. Near-Unity Photoluminescence Quantum Yield in MoS_2. *Science* **2015**, *350* (6264), 1065–1068.

(41) Yan, J.-Q.; Sales, B. C.; Susner, M. A.; McGuire, M. A. Flux Growth in a Horizontal Configuration: An Analog to Vapor Transport Growth. *Phys. Rev. Mater.* **2017**, *1* (2), 023402.

(42) Ubaldini, A.; Jacimovic, J.; Ubrig, N.; Giannini, E. Chloride-Driven Chemical Vapor Transport Method for Crystal Growth of Transition Metal Dichalcogenides. *Cryst. Growth Des.* **2013**, *13* (10), 4453–4459.

(43) Hu, S. Y.; Liang, C. H.; Tiong, K. K.; Lee, Y. C.; Huang, Y. S. Preparation and Characterization of Large Niobium-Doped $MoSe_2$ Single Crystals. *J. Cryst. Growth* **2005**, *285* (3), 408–414.

(44) Bougouma, M.; Batan, A.; Guel, B.; Segato, T.; Legma, J. B.; Reniers, F.; Delplancke-Ogletree, M.-P.; Buess-Herman, C.; Doneux, T. Growth and Characterization of Large, High Quality $MoSe_2$ Single Crystals. *J. Cryst. Growth* **2013**, *363*, 122–127.

(45) Hu, D.; Xu, G.; Xing, L.; Yan, X.; Wang, J.; Zheng, J.; Lu, Z.; Wang, P.; Pan, X.; Jiao, L. Two-Dimensional Semiconductors Grown by Chemical Vapor Transport. *Angew. Chem. Int. Ed.* **2017**, *56* (13), 3611–3615.

(46) Li, H.; Liu, J.; Guo, N.; Xiao, L.; Zhang, H.; Zhou, S.; Wu, Y.; Fan, S. Seeded Growth of High-Quality Transition Metal Dichalcogenide Single Crystals *via* Chemical Vapor Transport. *CrystEngComm* **2020**, *22* (46), 8017–8022.

(47) Zhang, X.; Lou, F.; Li, C.; Zhang, X.; Jia, N.; Yu, T.; He, J.; Zhang, B.; Xia, H.; Wang, S.; Tao, X. Flux Method Growth of Bulk MoS_2 Single Crystals and Their Application as a Saturable Absorber. *CrystEngComm* **2015**, *17* (21), 4026–4032.

(48) Edelberg, D.; Rhodes, D.; Kerelsky, A.; Kim, B.; Wang, J.; Zangiabadi, A.; Kim, C.; Abhinandan, A.; Ardelean, J.; Scully, M.; Scullion, D.; Embon, L.; Zu, R.; Santos, E. J. G.; Balicas, L.; Marianetti, C.; Barmak, K.; Zhu, X.; Hone, J.; Pasupathy, A. N. Approaching the Intrinsic Limit in Transition Metal Diselenides via Point Defect Control. *Nano Lett.* **2019**, *19* (7), 4371–4379.

(49) Gustafsson, M. V.; Yankowitz, M.; Forsythe, C.; Rhodes, D.; Watanabe, K.; Taniguchi, T.; Hone, J.; Zhu, X.; Dean, C. R. Ambipolar Landau Levels and Strong Band-Selective Carrier Interactions in Monolayer WSe_2. *Nat. Mater.* **2018**, *17* (5), 411–415.

(50) Liu, S.; Liu, Y.; Holtzman, L.; Li, B.; Holbrook, M.; Pack, J.; Taniguchi, T.; Watanabe, K.; Dean, C. R.; Pasupathy, A. N.; Barmak, K.; Rhodes, D. A.; Hone, J. Two-Step Flux Synthesis of Ultrapure Transition-Metal Dichalcogenides. *ACS Nano* **2023**, *17* (17), 16587–16596.

(51) Li, Y.; Kuang, G.; Jiao, Z.; Yao, L.; Duan, R. Recent Progress on the Mechanical Exfoliation of 2D Transition Metal Dichalcogenides. *Mater. Res. Express* **2022**, *9* (12), 122001.

(52) Huang, Y.; Pan, Y.-H.; Yang, R.; Bao, L.-H.; Meng, L.; Luo, H.-L.; Cai, Y.-Q.; Liu, G.-D.; Zhao, W.-J.; Zhou, Z.; Wu, L.-M.; Zhu, Z.-L.; Huang, M.; Liu, L.-W.; Liu, L.; Cheng, P.; Wu, K.-H.; Tian, S.-B.; Gu, C.-Z.; Shi, Y.-G.; Guo, Y.-F.; Cheng, Z. G.; Hu, J.-P.; Zhao, L.; Yang, G.-H.; Sutter, E.; Sutter, P.; Wang, Y.-L.; Ji, W.; Zhou, X.-J.; Gao, H.-J. Universal Mechanical Exfoliation of Large-Area 2D Crystals. *Nat. Commun.* **2020**, *11* (1), 2453.

(53) Velický, M.; Donnelly, G. E.; Hendren, W. R.; McFarland, S.; Scullion, D.; DeBenedetti, W. J. I.; Correa, G. C.; Han, Y.; Wain, A. J.; Hines, M. A.; Muller, D. A.; Novoselov, K. S.; Abruña, H. D.; Bowman, R. M.; Santos, E. J. G.; Huang, F. Mechanism of Gold-Assisted Exfoliation of Centimeter-Sized Transition-Metal Dichalcogenide Monolayers. *ACS Nano* **2018**, *12* (10), 10463–10472.

(54) Nicolosi, V.; Chhowalla, M.; Kanatzidis, M. G.; Strano, M. S.; Coleman, J. N. Liquid Exfoliation of Layered Materials. *Science* **2013**, *340* (6139), 1226419.

(55) Coleman, J. N.; Lotya, M.; O'Neill, A.; Bergin, S. D.; King, P. J.; Khan, U.; Young, K.; Gaucher, A.; De, S.; Smith, R. J.; Shvets, I. V.; Arora, S. K.; Stanton, G.; Kim, H.-Y.; Lee, K.; Kim, G. T.; Duesberg, G. S.; Hallam, T.; Boland, J. J.; Wang, J. J.; Donegan, J. F.; Grunlan, J. C.; Moriarty, G.; Shmeliov, A.; Nicholls, R. J.; Perkins, J. M.; Grieveson, E. M.; Theuwissen, K.; McComb, D. W.; Nellist, P. D.; Nicolosi, V. Two-Dimensional Nanosheets Produced by Liquid Exfoliation of Layered Materials. *Science* **2011**, *331* (6017), 568–571.

(56) Manzeli, S.; Ovchinnikov, D.; Pasquier, D.; Yazyev, O. V.; Kis, A. 2D Transition Metal Dichalcogenides. *Nat. Rev. Mater.* **2017**, *2* (8), 17033.

(57) Lee, Y.; Zhang, X.; Zhang, W.; Chang, M.; Lin, C.; Chang, K.; Yu, Y.; Wang, J. T.; Chang, C.; Li, L.; Lin, T. Synthesis of Large-Area MoS_2 Atomic Layers with Chemical Vapor Deposition. *Adv. Mater.* **2012**, *24* (17), 2320–2325.

(58) Yu, Y.; Li, C.; Liu, Y.; Su, L.; Zhang, Y.; Cao, L. Controlled Scalable Synthesis of Uniform, High-Quality Monolayer and Few-Layer MoS_2 Films. *Sci. Rep.* **2013**, *3* (1), 1866.

(59) Zhan, Y.; Liu, Z.; Najmaei, S.; Ajayan, P. M.; Lou, J. Large-Area Vapor-Phase Growth and Characterization of MoS_2 Atomic Layers on a SiO_2 Substrate. *Small* **2012**, *8* (7), 966–971.

(60) Song, J.-G.; Park, J.; Lee, W.; Choi, T.; Jung, H.; Lee, C. W.; Hwang, S.-H.; Myoung, J. M.; Jung, J.-H.; Kim, S.-H.; Lansalot-Matras, C.; Kim, H. Layer-Controlled, Wafer-Scale, and Conformal Synthesis of Tungsten Disulfide Nanosheets Using Atomic Layer Deposition. *ACS Nano* **2013**, *7* (12), 11333–11340.

(61) Zhang, T.; Wang, J.; Wu, P.; Lu, A.-Y.; Kong, J. Vapour-Phase Deposition of Two-Dimensional Layered Chalcogenides. *Nat. Rev. Mater.* **2023**, *8* (12), 799–821.

(62) Kang, K.; Xie, S.; Huang, L.; Han, Y.; Huang, P. Y.; Mak, K. F.; Kim, C.-J.; Muller, D.; Park, J. High-Mobility Three-Atom-Thick Semiconducting Films with Wafer-Scale Homogeneity. *Nature* **2015**, *520* (7549), 656–660.

(63) Tao, J.; Chai, J.; Lu, X.; Wong, L. M.; Wong, T. I.; Pan, J.; Xiong, Q.; Chi, D.; Wang, S. Growth of Wafer-Scale MoS_2 Monolayer by Magnetron Sputtering. *Nanoscale* **2015**, *7* (6), 2497–2503.

(64) Krbal, M.; Prokop, V.; Kononov, A. A.; Pereira, J. R.; Mistrik, J.; Kolobov, A. V.; Fons, P. J.; Saito, Y.; Hatayama, S.; Shuang, Y.; Sutou, Y.; Rozhkov, S. A.; Stellhorn, J. R.; Hayakawa, S.; Pis, I.; Bondino, F. Amorphous-to-Crystal Transition in Quasi-Two-Dimensional MoS_2: Implications for 2D Electronic Devices. *ACS Appl. Nano Mater.* **2021**, *4* (9), 8834–8844.

(65) Zeng, L.; Tao, L.; Tang, C.; Zhou, B.; Long, H.; Chai, Y.; Lau, S. P.; Tsang, Y. H. High-Responsivity UV-Vis Photodetector Based on Transferable WS_2 Film Deposited by Magnetron Sputtering. *Sci. Rep.* **2016**, *6* (1), 20343.

(66) Yang, Z.; Hao, J. Progress in Pulsed Laser Deposited Two-Dimensional Layered Materials for Device Applications. *J Mater. Chem. C* **2016**, *4* (38), 8859–8878.

(67) Serrao, C. R.; Diamond, A. M.; Hsu, S.-L.; You, L.; Gadgil, S.; Clarkson, J.; Carraro, C.; Maboudian, R.; Hu, C.; Salahuddin, S. Highly Crystalline MoS_2 Thin Films Grown by Pulsed Laser Deposition. *Appl. Phys. Lett.* **2015**, *106* (5), 052101.

(68) Serna, M. I.; Yoo, S. H.; Moreno, S.; Xi, Y.; Oviedo, J. P.; Choi, H.; Alshareef, H. N.; Kim, M. J.; Minary-Jolandan, M.; Quevedo-Lopez, M. A. Large-Area Deposition of MoS_2 by Pulsed Laser Deposition with *In Situ* Thickness Control. *ACS Nano* **2016**, *10* (6), 6054–6061.

(69) Peng, Q.; Chen, N.; Huang, D.; Heller, E.; Cardimona, D.; Gao, F. First-Principles Assessment of the Structure and Stability of 15 Intrinsic Point Defects in Zinc-Blende Indium Arsenide. *Crystals* **2019**, *9* (1), 48.

(70) Carvalho, A.; Neto, A. H. C. Donor and Acceptor Levels in Semiconducting Transition-Metal Dichalcogenides. *Phys. Rev. B* **2014**, *89* (8), 081406.

(71) Nienhaus, L.; Sereika, R.; MacManus-Driscoll, J. L.; Bawendi, M.; Wilson, M. W. B.; Buonassisi, T.; Gorai, P.; Stevanović, V.; Brandt, R. E.; Žaltauskas, R.; Lee, L. C.; Kurchin, R. C.; Hoye, R. L. Z.; Poindexter, J. R.; Polizzotti, J. A. Searching for "Defect-Tolerant" Photovoltaic Materials: Combined Theoretical and Experimental Screening. *Chem. Mater.* **2017**, *29* (11), 4667–4674.

(72) Feng, L. P.; Su, J.; Chen, S.; Liu, Z. T. First-Principles Investigations on Vacancy Formation and Electronic Structures of Monolayer MoS_2. *Mater. Chem. Phys.* **2014**, *148* (1–2), 5–9.

(73) Chirita Mihaila, A. I.; Susi, T.; Kotakoski, J. Influence of Temperature on the Displacement Threshold Energy in Graphene. *Sci. Rep.* **2019**, *9* (1), 12981.

(74) Zhou, W.; Zou, X.; Najmaei, S.; Liu, Z.; Shi, Y.; Kong, J.; Lou, J.; Ajayan, P. M.; Yakobson, B. I.; Idrobo, J.-C. Intrinsic Structural Defects in Monolayer Molybdenum Disulfide. *Nano. Lett.* **2013**, *13* (6), 2615–2622.

(75) Jin, H.; Debroye, E.; Keshavarz, M.; Scheblykin, I. G.; Roeffaers, M. B. J.; Hofkens, J.; Steele, J. A. It's a Trap! On the Nature of Localised States and Charge Trapping in Lead Halide Perovskites. *Mater. Horiz.* **2020**, *7* (2), 397–410.

(76) Li, L.; Long, R.; Bertolini, T.; Prezhdo, O. V. Sulfur Adatom and Vacancy Accelerate Charge Recombination in MoS_2 but by Different Mechanisms: Time-Domain Ab Initio Analysis. *Nano Lett.* **2017**, *17* (12), 7962–7967.

(77) Alberi, K.; Scarpulla, M. A. Effects of Excess Carriers on Charged Defect Concentrations in Wide Bandgap Semiconductors. *J. Appl. Phys.* **2018**, *123* (18), 185702.

(78) Yang, J. H.; Shi, L.; Wang, L. W.; Wei, S. H. Non-Radiative Carrier Recombination Enhanced by Two-Level Process: A First-Principles Study. *Sci. Rep.* **2016**, *6* (1), 21712.

(79) Wang, D.; Han, D.; West, D.; Chen, N. K.; Xie, S. Y.; Tian, W. Q.; Meunier, V.; Zhang, S.; Li, X. Bin. Excitation to Defect-Bound Band Edge States in Two-Dimensional Semiconductors and Its Effect on Carrier Transport. *NPJ Comput. Mater.* **2019**, *5* (1), 8.

(80) Das, B.; Aguilera, I.; Rau, U.; Kirchartz, T. What Is a Deep Defect? Combining Shockley-Read-Hall Statistics with Multiphonon Recombination Theory. *Phys. Rev. Mater.* **2020**, *4* (2), 024602.

(81) Noh, J. Y.; Kim, H.; Kim, Y. S. Stability and Electronic Structures of Native Defects in Single-Layer MoS_2. *Phys. Rev. B* **2014**, *89* (20), 205417.

(82) Yang, J.; Wang, Y.; Lagos, M. J.; Manichev, V.; Fullon, R.; Song, X.; Voiry, D.; Chakraborty, S.; Zhang, W.; Batson, P. E.; Feldman, L.; Gustafsson, T.; Chhowalla, M. Single Atomic Vacancy Catalysis. *ACS Nano* **2019**, *13* (9), 9958–9964.

(83) Robertson, A. W.; Lin, Y. C.; Wang, S.; Sawada, H.; Allen, C. S.; Chen, Q.; Lee, S.; Lee, G. Do; Lee, J.; Han, S.; Yoon, E.; Kirkland, A. I.; Kim, H.; Suenaga, K.; Warner, J. H. Atomic Structure and Spectroscopy of Single Metal (Cr, V) Substitutional Dopants in Monolayer MoS_2. *ACS Nano* **2016**, *10* (11), 10227–10236.

(84) Qiu, H.; Xu, T.; Wang, Z.; Ren, W.; Nan, H.; Ni, Z.; Chen, Q.; Yuan, S.; Miao, F.; Song, F.; Long, G.; Shi, Y.; Sun, L.; Wang, J.; Wang, X. Hopping Transport through Defect-Induced Localized States in Molybdenum Disulphide. *Nat. Commun.* **2013**, *4*, 3–8.

(85) Barja, S.; Refaely-Abramson, S.; Schuler, B.; Qiu, D. Y.; Pulkin, A.; Wickenburg, S.; Ryu, H.; Ugeda, M. M.; Kastl, C.; Chen, C.; Hwang, C.; Schwartzberg, A.; Aloni, S.; Mo, S. K.; Ogletree, D. F.; Crommie, M. F.; Yazyev, O. V; Louie, S. G.; Neaton, J. B.; Weber-Bargioni, A. Identifying Substitutional Oxygen as a Prolific Point Defect in Monolayer Transition Metal Dichalcogenides. *Nat. Commun.* **2019**, *10* (1), 3382.

(86) Liu, M.; Shi, J.; Li, Y.; Zhou, X.; Ma, D.; Qi, Y.; Zhang, Y.; Liu, Z. Temperature-Triggered Sulfur Vacancy Evolution in Monolayer MoS_2/Graphene Heterostructures. *Small* **2017**, *13* (40), 1602967.

(87) Xu, K.; Holbrook, M.; Holtzman, L. N.; Pasupathy, A. N.; Barmak, K.; Hone, J. C.; Rosenberger, M. R. Validating the Use of Conductive Atomic Force Microscopy for Defect Quantification in 2D Materials. *ACS Nano* **2023**, *17* (24), 24743–24752.

(88) Jeong, H. Y.; Lee, S. Y.; Ly, T. H.; Han, G. H.; Kim, H.; Nam, H.; Jiong, Z.; Shin, B. G.; Yun, S. J.; Kim, J.; Kim, U. J.; Hwang, S.; Lee, Y. H. Visualizing Point Defects in Transition-Metal Dichalcogenides Using Optical Microscopy. *ACS Nano* **2016**, *10* (1), 770–777.

(89) Frisenda, R.; Navarro-Moratalla, E.; Gant, P.; Pérez De Lara, D.; Jarillo-Herrero, P.; Gorbachev, R. V.; Castellanos-Gomez, A. Recent Progress in the Assembly of Nanodevices and van Der Waals Heterostructures by Deterministic Placement of 2D Materials. *Chem. Soc. Rev.* **2018**, *47* (1), 53–68.

(90) Kim, H.; Han, G. H.; Yun, S. J.; Zhao, J.; Keum, D. H.; Jeong, H. Y.; Ly, T. H.; Jin, Y.; Park, J.-H.; Moon, B. H.; Kim, S.-W.; Lee, Y. H. Role of Alkali Metal Promoter in Enhancing Lateral Growth of Monolayer Transition Metal Dichalcogenides. *Nanotechnology* **2017**, *28* (36), 36LT01.

(91) Hong, J.; Hu, Z.; Probert, M.; Li, K.; Lv, D.; Yang, X.; Gu, L.; Mao, N.; Feng, Q.; Xie, L.; Zhang, J.; Wu, D.; Zhang, Z.; Jin, C.; Ji, W.; Zhang, X.; Yuan, J.; Zhang, Z. Exploring Atomic Defects in Molybdenum Disulphide Monolayers. *Nat. Commun.* **2015**, *6*, 6293.

(92) Cuenot, S.; Bouchara, J.-P. Atomic Force Microscopy: A Promising Tool for Deciphering the Pathogenic Mechanisms of Fungi in Cystic Fibrosis. *Mycopathologia* **2018**, *183* (1), 291–310.

(93) Krečmarová, M.; Andres-Penares, D.; Fekete, L.; Ashcheulov, P.; Molina-Sánchez, A.; Canet-Albiach, R.; Gregora, I.; Mortet, V.; Martínez-Pastor, J. P.; Sánchez-Royo, J. F. Optical Contrast and Raman Spectroscopy Techniques Applied to Few-Layer 2D Hexagonal Boron Nitride. *Nanomaterials* **2019**, *9* (7), 1047.

(94) Huang, F. Optical Contrast of Atomically Thin Films. *J. Phys. Chem. C* **2019**, *123* (12), 7440–7446.

(95) Roddaro, S.; Pingue, P.; Piazza, V.; Pellegrini, V.; Beltram, F. The Optical Visibility of Graphene: Interference Colors of Ultrathin Graphite on SiO_2. *Nano Lett.* **2007**, *7* (9), 2707–2710.

(96) Blake, P.; Hill, E. W.; Castro Neto, A. H.; Novoselov, K. S.; Jiang, D.; Yang, R.; Booth, T. J.; Geim, A. K. Making Graphene Visible. *Appl. Phys. Lett.* **2007**, *91* (6), 063124.

(97) Li, H.; Wu, J.; Huang, X.; Lu, G.; Yang, J.; Lu, X.; Xiong, Q.; Zhang, H. Rapid and Reliable Thickness Identification of Two-Dimensional Nanosheets Using Optical Microscopy. *ACS Nano* **2013**, *7* (11), 10344–10353.

(98) Kozawa, D.; Kumar, R.; Carvalho, A.; Kumar Amara, K.; Zhao, W.; Wang, S.; Toh, M.; Ribeiro, R. M.; Castro Neto, A. H.; Matsuda, K.; Eda, G. Photocarrier Relaxation Pathway in Two-Dimensional Semiconducting Transition Metal Dichalcogenides. *Nat. Commun.* **2014**, *5* (1), 4543.

(99) Horng, J.; Martin, E. W.; Chou, Y.-H.; Courtade, E.; Chang, T.-C.; Hsu, C.-Y.; Wentzel, M.-H.; Ruth, H. G.; Lu, T.-C.; Cundiff, S. T.; Wang, F.; Deng, H. Perfect Absorption by an Atomically Thin Crystal. *Phys. Rev. Appl.* **2020**, *14*, 24009.

(100) Mallick, S. P.; Hong, Y. H.; Chen, L. R.; Kao, T. S.; Lu, T. C. Effect of Passivation Layer on the Thin Film Perovskite Random Lasers. *Materials* **2020**, *13* (10), 2322.

(101) Lloyd, D.; Liu, X.; Christopher, J. W.; Cantley, L.; Wadehra, A.; Kim, B. L.; Goldberg, B. B.; Swan, A. K.; Bunch, J. S. Band Gap Engineering with Ultralarge Biaxial Strains in Suspended Monolayer MoS_2. *Nano Lett.* **2016**, *16* (9), 5836–5841.

(102) Wu, Z.; Zhao, W.; Jiang, J.; Zheng, T.; You, Y.; Lu, J.; Ni, Z. Defect Activated Photoluminescence in WSe_2 Monolayer. *J. Phys. Chem. C* **2017**, *121* (22), 12294–12299.

(103) Reshchikov, M. A. Temperature Dependence of Defect-Related Photoluminescence in III-V and II-VI Semiconductors. *J Appl Phys* 2014, *115* (1). https://doi.org/10.1063/1.4838038.

(104) Tongay, S.; Suh, J.; Ataca, C.; Fan, W.; Luce, A.; Kang, J. S.; Liu, J.; Ko, C.; Raghunathanan, R.; Zhou, J.; Ogletree, F.; Li, J.; Grossman, J. C.; Wu, J. Defects Activated Photoluminescence in Two-Dimensional Semiconductors: Interplay between Bound, Charged, and Free Excitons. *Sci. Rep.* **2013**, *3* (1), 2657.

(105) Kaplan, D.; Mills, K.; Lee, J.; Torrel, S.; Swaminathan, V. Excitation Intensity Dependent Photoluminescence of Annealed Two-Dimensional MoS_2 Grown by Chemical Vapor Deposition. *J. Appl. Phys.* **2016**, *119* (21), 214301.

(106) Srivastava, A.; Sidler, M.; Allain, A. V.; Lembke, D. S.; Kis, A.; Imamoglu, A. Optically Active Quantum Dots in Monolayer WSe_2. *Nat. Nanotechnol.* **2015**, *10* (6), 491–496.

(107) Zhang, Z.; Liang, H.; Loh, L.; Chen, Y.; Chen, Y.; Watanabe, K.; Taniguchi, T.; Quek, S. Y.; Bosman, M.; Bettiol, A. A.; Eda, G. Optically Active Chalcogen Vacancies in Monolayer Semiconductors. *Adv. Opt. Mater.* **2022**, *10* (23). 2201350.

(108) Baker, M. J.; Hughes, C. S.; Hollywood, K. A. Raman Spectroscopy. *Biophotonics: Vibrational Spectroscopic Diagnostics*. **2016**.

(109) Lee, C.; Yan, H.; Brus, L. E.; Heinz, T. F.; Hone, J.; Ryu, S. Anomalous Lattice Vibrations of Single-and Few-Layer MoS_2. *ACS Nano* **2010**, *4* (5), 2695–2700.

(110) Ferrari, A. C.; Basko, D. M. Raman Spectroscopy as a Versatile Tool for Studying the Properties of Graphene. *Nat. Nanotechnol.* **2013**, *8* (4), 235–246.

(111) Dimitrievska, M.; Fairbrother, A.; Saucedo, E.; Pérez-Rodríguez, A.; Izquierdo-Roca, V. Influence of Compositionally Induced Defects on the Vibrational Properties of Device Grade $Cu_2ZnSnSe_4$ Absorbers for Kesterite Based Solar Cells. *Appl. Phys. Lett.* **2015**, *106* (7), 073903.

(112) Mignuzzi, S.; Pollard, A. J.; Bonini, N.; Brennan, B.; Gilmore, I. S.; Pimenta, M. A.; Richards, D.; Roy, D. Effect of Disorder on Raman Scattering of Single-Layer MoS_2. *Phys. Rev. B* **2015**, *91* (19), 195411.

(113) Stevie, F. A.; Donley, C. L. Introduction to X-Ray Photoelectron Spectroscopy. *J. Vac. Sci. Technol.* **2020**, *38* (6), 63204.

(114) Colón Santana, J. A. Charging Effects in X-Ray Photoelectron Spectroscopy. *J. Electron. Spectrosc.* **1992**, *59* (1), 1–14.

(115) Wang, Y.; Kim, J. C.; Wu, R. J.; Martinez, J.; Song, X.; Yang, J.; Zhao, F.; Mkhoyan, A.; Jeong, H. Y.; Chhowalla, M. Van Der Waals Contacts between Three-Dimensional Metals and Two-Dimensional Semiconductors. *Nature* **2019**, *568* (7750), 70–74.

(116) Harrington, G. F.; Santiso, J. Back-to-Basics Tutorial: X-Ray Diffraction of Thin Films. *J. Electroceram.* **2021**, *47* (4), 141–163.

(117) Chubarov, M.; Choudhury, T. H.; Zhang, X.; Redwing, J. M. In-Plane X-Ray Diffraction for Characterization of Monolayer and Few-Layer Transition Metal Dichalcogenide Films. *Nanotechnol.* **2018**, *29* (5), 055706.

(118) Bretscher, H.; Li, Z.; Xiao, J.; Qiu, D. Y.; Refaely-Abramson, S.; Alexander-Webber, J. A.; Tanoh, A.; Fan, Y.; Delport, G.; Williams, C. A.; Stranks, S. D.; Hofmann, S.; Neaton, J. B.; Louie, S. G.; Rao, A. Rational Passivation of Sulfur Vacancy Defects in Two-Dimensional Transition Metal Dichalcogenides. *ACS Nano* **2021**, *15* (5), 8780–8789.

(119) Verhagen, T.; Guerra, V. L. P.; Haider, G.; Kalbac, M.; Vejpravova, J. Towards the Evaluation of Defects in MoS_2 Using Cryogenic Photoluminescence Spectroscopy. *Nanoscale* **2020**, *12* (5), 3019–3028.

(120) Goodman, A. J.; Willard, A. P.; Tisdale, W. A. Exciton Trapping Is Responsible for the Long Apparent Lifetime in Acid-Treated MoS_2. *Phys. Rev. B* **2017**, *96* (12), 121404.

(121) Sarkar, S.; Goswami, S.; Trushin, M.; Saha, S.; Panahandeh-Fard, M.; Prakash, S.; Tan, S. J. R.; Scott, M.; Loh, K. P.; Adam, S.; Mathew, S.; Venkatesan, T. Polaronic Trions at the $MoS_2/SrTiO_3$ Interface. *Adv. Mater.* **2019**, *31* (41), 1903569.

(122) Bae, S.; Sugiyama, N.; Matsuo, T.; Raebiger, H.; Shudo, K. I.; Ohno, K. Defect-Induced Vibration Modes of Ar^+-Irradiated MoS_2. *Phys. Rev. Appl.* **2017**, *7* (2), 024001.

(123) Kondekar, N. P.; Boebinger, M. G.; Woods, E. V.; McDowell, M. T. *In Situ* XPS Investigation of Transformations at Crystallographically Oriented MoS_2 Interfaces. *ACS Appl. Mater. Interfaces* **2017**, *9* (37), 32394–32404.

(124) Scofield, J. H. *Theoretical Photoionization Cross Sections from 1 to 1500 KeV*; Report No. UCRL-51326; Lawrence Livermore Laboratory, California University: Livermore, CA, 1973.

(125) Zhao, Y.; Tripathi, M.; Čerņevičs, K.; Avsar, A.; Ji, H. G.; Gonzalez Marin, J. F.; Cheon, C. Y.; Wang, Z.; Yazyev, O. V.; Kis, A. Electrical Spectroscopy of Defect States and Their Hybridization in Monolayer MoS_2. *Nat. Commun.* **2023**, *14* (1), 44.

(126) Frisenda, R.; Niu, Y.; Gant, P.; Molina-Mendoza, A. J.; Schmidt, R.; Bratschitsch, R.; Liu, J.; Fu, L.; Dumcenco, D.; Kis, A.; De Lara, D. P.; Castellanos-Gomez, A. Micro-Reflectance and Transmittance Spectroscopy: A Versatile and Powerful Tool to Characterize 2D Materials. *J. Phys. D Appl. Phys.* **2017**, *50* (7), 074002.

(127) Mitterreiter, E.; Schuler, B.; Micevic, A.; Hernangómez-Pérez, D.; Barthelmi, K.; Cochrane, K. A.; Kiemle, J.; Sigger, F.; Klein, J.; Wong, E.; Barnard, E. S.; Watanabe, K.; Taniguchi, T.; Lorke, M.; Jahnke, F.; Finley, J. J.; Schwartzberg, A. M.; Qiu, D. Y.; Refaely-

Abramson, S.; Holleitner, A. W.; Weber-Bargioni, A.; Kastl, C. The Role of Chalcogen Vacancies for Atomic Defect Emission in MoS_2. *Nat. Commun.* **2021**, *12* (1), 3822.

(128) Wierzbowski, J.; Klein, J.; Sigger, F.; Straubinger, C.; Kremser, M.; Taniguchi, T.; Watanabe, K.; Wurstbauer, U.; Holleitner, A. W.; Kaniber, M.; Müller, K.; Finley, J. J. Direct Exciton Emission from Atomically Thin Transition Metal Dichalcogenide Heterostructures near the Lifetime Limit. *Sci. Rep.* **2017**, *7* (1), 12383.

(129) Yagodkin, D.; Greben, K.; Eljarrat, A.; Kovalchuk, S.; Ghorbani-Asl, M.; Jain, M.; Kretschmer, S.; Severin, N.; Rabe, J. P.; Krasheninnikov, A. V.; Koch, C. T.; Bolotin, K. I. Extrinsic Localized Excitons in Patterned 2D Semiconductors. *Adv. Funct. Mater.* **2022**, *32* (31), 2203060.

(130) Klein, J.; Sigl, L.; Gyger, S.; Barthelmi, K.; Florian, M.; Rey, S.; Taniguchi, T.; Watanabe, K.; Jahnke, F.; Kastl, C.; Zwiller, V.; Jöns, K. D.; Müller, K.; Wurstbauer, U.; Finley, J. J.; Holleitner, A. W. Engineering the Luminescence and Generation of Individual Defect Emitters in Atomically Thin MoS_2. *ACS Photonics* **2021**, *8* (2), 669–677.

(131) Wang, H.; Zhang, C.; Chan, W.; Manolatou, C.; Tiwari, S.; Rana, F. Radiative Lifetimes of Excitons and Trions in Monolayers of the Metal Dichalcogenide MoS_2. *Phys. Rev. B* **2016**, *93* (4), 045407.

(132) Grünleitner, T.; Henning, A.; Bissolo, M.; Zengerle, M.; Gregoratti, L.; Amati, M.; Zeller, P.; Eichhorn, J.; Stier, A. V; Holleitner, A. W.; Finley, J. J.; Sharp, I. D. Real-Time Investigation of Sulfur Vacancy Generation and Passivation in Monolayer Molybdenum Disulfide via *in Situ* X-Ray Photoelectron Spectromicroscopy. *ACS Nano* **2022**, *16* (12), 20364–20375.

(133) Wu, X.; Gu, Y.; Ge, R.; Serna, M. I.; Huang, Y.; Lee, J. C.; Akinwande, D. Electron Irradiation-Induced Defects for Reliability Improvement in Monolayer MoS_2-Based Conductive-Point Memory Devices. *Npj 2D Mater. Appl.* **2022**, *6*, 1–12.

(134) Garcia-Esparza, A. T.; Park, S.; Abroshan, H.; Mellone, O. A. P.; Vinson, J.; Abraham, B.; Kim, T. R.; Nordlund, D.; Gallo, A.; Alonso-Mori, R.; Zheng, X.; Sokaras, D. Local Structure of Sulfur Vacancies on the Basal Plane of Monolayer MoS2. *ACS Nano* **2022**, *16* (4), 6725–6733.

(135) Dash, A. K.; Swaminathan, H.; Berger, E.; Mondal, M.; Lehenkari, T.; Prasad, P. R.; Watanabe, K.; Taniguchi, T.; Komsa, H.-P.; Singh, A. Evidence of Defect Formation in Monolayer MoS_2 at Ultralow Accelerating Voltage Electron Irradiation. *2D Materials*, **2023**, *10*(3), 035002.

(136) Lee, J.-Y.; Kim, J. H.; Jung, Y.; Shin, J. C.; Lee, Y.; Kim, K.; Kim, N.; van der Zande, A. M.; Son, J.; Lee, G.-H. Evolution of Defect Formation during Atomically Precise Desulfurization of Monolayer MoS_2. *Commun. Mater.* **2021**, *2* (1), 80.

(137) Micevic, A.; Pettinger, N.; Hötger, A.; Sigl, L.; Florian, M.; Taniguchi, T.; Watanabe, K.; Müller, K.; Finley, J. J.; Kastl, C.; Holleitner, A. W. On-Demand Generation of Optically Active Defects in Monolayer WS_2 by a Focused Helium Ion Beam. *Appl. Phys. Lett.* **2022**, *121* (18), 183101.

(138) Wang, X.; Pettes, M. T.; Wang, Y.; Zhu, J.-X.; Dhall, R.; Song, C.; Jones, A. C.; Ciston, J.; Yoo, J. Enhanced Exciton-to-Trion Conversion by Proton Irradiation of Atomically Thin WS_2. *Nano Lett.* **2023**, *23* (9), 3754–3761.

(139) Parto, K.; Azzam, S. I.; Banerjee, K.; Moody, G. Defect and Strain Engineering of Monolayer WSe_2 Enables Site-Controlled Single-Photon Emission up to 150 K. *Nat. Commun.* **2021**, *12* (1), 3585.

(140) Krustok, J.; Kaupmees, R.; Jaaniso, R.; Kiisk, V.; Sildos, I.; Li, B.; Gong, Y. Local Strain-Induced Band Gap Fluctuations and Exciton Localization in Aged WS_2 Monolayers. *AIP Adv.* **2017**, *7* (6), 65005.

(141) Koperski, M.; Nogajewski, K.; Arora, A.; Cherkez, V.; Mallet, P.; Veuillen, J. Y.; Marcus, J.; Kossacki, P.; Potemski, M. Single Photon Emitters in Exfoliated WSe_2 Structures. *Nat. Nanotechnol.* **2015**, *10* (6), 503–506.

(142) Parto, K.; Azzam, S. I.; Banerjee, K.; Moody, G. Defect and Strain Engineering of Monolayer WSe_2 Enables Site-Controlled Single-Photon Emission up to 150 K. *Nat. Commun.* **2021**, *12* (1), 3585.

(143) Li, L.; Qin, Z.; Ries, L.; Hong, S.; Michel, T.; Yang, J.; Salameh, C.; Bechelany, M.; Miele, P.; Kaplan, D.; Chhowalla, M.; Voiry, D. Role of Sulfur Vacancies and Undercoordinated Mo Regions in MoS2 Nanosheets toward the Evolution of Hydrogen. *ACS Nano* **2019**, *13* (6), 6824–6834.

(144) Lin, L.; Miao, N.; Huang, J.; Zhang, S.; Zhu, Y.; Horsell, D. D.; Ghosez, P.; Sun, Z.; Allwood, D. A. A Photocatalyst of Sulphur Depleted Monolayered Molybdenum Sulfide Nanocrystals for Dye Degradation and Hydrogen Evolution Reaction. *Nano Energy* **2017**, *38*, 544–552.

(145) Zhang, Q.; Wee, A. T. S.; Liang, Q.; Zhao, X.; Liu, M. Defect Engineering of Two-Dimensional Transition-Metal Dichalcogenides: Applications, Challenges, and Opportunities. *ACS nano* **2021**, *15*(2), 2165–2181.

(146) Lee, J.-Y.; Kim, J. H.; Jung, Y.; Shin, J. C.; Lee, Y.; Kim, K.; Kim, N.; van der Zande, A. M.; Son, J.; Lee, G.-H. Evolution of Defect Formation during Atomically Precise Desulfurization of Monolayer MoS_2. *Commun. Mater.* **2021**, *2* (1), 80.

(147) Bowker, M.; Madix, R. J. UPS and Thermal Desorption Studies of Alcohol Adsorption on Cu (110): I. Methanol. *Surf. Sci.* **1980**, *95*, 190–206.

(148) Lu, A.-Y.; Zhu, H.; Xiao, J.; Chuu, C.-P.; Han, Y.; Chiu, M.-H.; Cheng, C.-C.; Yang, C.-W.; Wei, K.-H.; Yang, Y.; Wang, Y.; Sokaras, D.; Nordlund, D.; Yang, P.; Muller, D. A.; Chou, M.-Y.; Zhang, X.; Li, L.-J. Janus Monolayers of Transition Metal Dichalcogenides. *Nat. Nanotechnol.* **2017**, *12* (8), 744–749.

(149) Zhang, J.; Jia, S.; Kholmanov, I.; Dong, L.; Er, D.; Chen, W.; Guo, H.; Jin, Z.; Shenoy, V. B.; Shi, L.; Lou, J. Janus Monolayer Transition-Metal Dichalcogenides. *ACS Nano* **2017**, *11* (8), 8192–8198.

(150) Lin, Z.; Liu, W.; Tian, S.; Zhu, K.; Huang, Y.; Yang, Y. Thermal Expansion Coefficient of Few-Layer MoS_2 Studied by Temperature-Dependent Raman Spectroscopy. *Sci. Rep.* **2021**, *11* (1), 7037.

(151) McCreary, A.; Ghosh, R.; Amani, M.; Wang, J.; Duerloo, K.-A. N.; Sharma, A.; Jarvis, K.; Reed, E. J.; Dongare, A. M.; Banerjee, S. K.; Terrones, M.; Namburu, R. R.; Dubey, M. Effects of Uniaxial and Biaxial Strain on Few-Layered Terrace Structures of MoS_2 Grown by Vapor Transport. *ACS Nano* **2016**, *10* (3), 3186–3197.

(152) Borghardt, S.; Tu, J.-S.; Winkler, F.; Schubert, J.; Zander, W.; Leosson, K.; Kardynał, B. E. Engineering of Optical and Electronic Band Gaps in Transition Metal Dichalcogenide Monolayers through External Dielectric Screening. *Phys. Rev. Mater.* **2017**, *1* (5), 054001.

(153) Raja, A.; Chaves, A.; Yu, J.; Arefe, G.; Hill, H. M.; Rigosi, A. F.; Berkelbach, T. C.; Nagler, P.; Schüller, C.; Korn, T.; Nuckolls, C.; Hone, J.; Brus, L. E.; Heinz, T. F.; Reichman, D. R.; Chernikov, A. Coulomb Engineering of the Bandgap and Excitons in Two-Dimensional Materials. *Nat. Commun.* **2017**, *8* (1), 15251.

(154) Ji, E.; Yang, K.; Shin, J.-C.; Kim, Y.; Park, J.-W.; Kim, J.; Lee, G.-H. Exciton-Dominant Photoluminescence of MoS_2 by a Functionalized Substrate. *Nanoscale* **2022**, *14* (38), 14106–14112.

(155) Nur, R.; Tsuchiya, T.; Toprasertpong, K.; Terabe, K.; Takagi, S.; Takenaka, M. High Responsivity in MoS_2 Phototransistors Based on Charge Trapping HfO_2 Dielectrics. *Commun. Mater.* **2020**, *1* (1), 103.

(156) Gieraltowska, S.; Wachnicki, L.; Dluzewski, P.; Witkowski, B. S.; Godlewski, M.; Guziewicz, E. Atomic Layer Deposition of HfO_2 Films Using TDMAH and Water or Ammonia Water. *Materials* **2023**, *16* (11), 4077.

(157) Ho, M.-Y.; Gong, H.; Wilk, G. D.; Busch, B. W.; Green, M. L.; Voyles, P. M.; Muller, D. A.; Bude, M.; Lin, W. H.; See, A.; Loomans, M. E.; Lahiri, S. K.; Räisänen, P. I. Morphology and Crystallization Kinetics in HfO_2 Thin Films Grown by Atomic Layer Deposition. *J. Appl. Phys.* **2003**, *93* (3), 1477–1481.

(158) Yan, H.; Wang, Y.; Li, Y.; Phuyal, D.; Guo, H.; Guo, Y.; Lee, T.-L.; Chhowalla, M. Ultra-Clean Interface between High k Dielectric and 2D MoS_2. *Under review*.

(159) Hötger, A.; Klein, J.; Barthelmi, K.; Sigl, L.; Sigger, F.; Männer, W.; Gyger, S.; Florian, M.; Lorke, M.; Jahnke, F.; Taniguchi, T.; Watanabe, K.; Jöns, K. D.; Wurstbauer, U.; Kastl, C.; Müller, K.; Finley, J. J.; Holleitner, A. W. Gate-Switchable Arrays of Quantum Light Emitters in Contacted Monolayer MoS_2 van Der Waals Heterodevices. *Nano Lett.* **2021**, *21* (2), 1040–1046.

(160) Palacios-Berraquero, C.; Kara, D. M.; Montblanch, A. R.-P.; Barbone, M.; Latawiec, P.; Yoon, D.; Ott, A. K.; Loncar, M.; Ferrari, A. C.; Atatüre, M. Large-Scale Quantum-Emitter Arrays in Atomically Thin Semiconductors. *Nat. Commun.* **2017**, *8* (1), 15093.

(161) Branny, A.; Kumar, S.; Proux, R.; Gerardot, B. D. Deterministic Strain-Induced Arrays of Quantum Emitters in a Two-Dimensional Semiconductor. *Nat. Commun.* **2017**, *8* (1), 15053.

(162) Plechinger, G.; Castellanos-Gomez, A.; Buscema, M.; van der Zant, H. S. J.; Steele, G. A.; Kuc, A.; Heine, T.; Schüller, C.; Korn, T. Control of Biaxial Strain in Single-Layer Molybdenite Using Local Thermal Expansion of the Substrate. *2D Mater.* **2015**, *2* (1), 015006.

(163) Li, Z.; Lv, Y.; Ren, L.; Li, J.; Kong, L.; Zeng, Y.; Tao, Q.; Wu, R.; Ma, H.; Zhao, B.; Wang, D.; Dang, W.; Chen, K.; Liao, L.; Duan, X.; Duan, X.; Liu, Y. Efficient Strain Modulation of 2D Materials via Polymer Encapsulation. *Nat. Commun.* **2020**, *11* (1), 1151.

(164) Shen, P. C.; Lin, Y.; Su, C.; McGahan, C.; Lu, A. Y.; Ji, X.; Wang, X.; Wang, H.; Mao, N.; Guo, Y.; Park, J. H.; Wang, Y.; Tisdale, W.; Li, J.; Ling, X.; Aidala, K. E.; Palacios, T.; Kong, J. Healing of Donor Defect States in Monolayer Molybdenum Disulfide Using Oxygen-Incorporated Chemical Vapour Deposition. *Nat. Electron.* **2022**, *5* (1), 28–36.

(165) Shard, A. G. Detection Limits in XPS for More than 6000 Binary Systems Using Al and Mg Kα X-rays. *Surf. Interface Anal.* **2014**, *46* (3), 175–185.

(166) Shree, S.; George, A.; Lehnert, T.; Neumann, C.; Benelajla, M.; Robert, C.; Marie, X.; Watanabe, K.; Taniguchi, T.; Kaiser, U.; Urbaszek, B.; Turchanin, A. High Optical Quality of MoS_2 Monolayers Grown by Chemical Vapor Deposition. *2D Mater.* **2019**, *7* (1), 015011.